Escaping Events at the NOvA Far Detector

A DISSERTATION
SUBMITTED TO THE FACULTY OF THE GRADUATE SCHOOL
OF THE UNIVERSITY OF MINNESOTA
BY

Vladimir Bychkov

IN PARTIAL FULFILLMENT OF THE REQUIREMENTS
FOR THE DEGREE OF
DOCTOR OF PHILOSOPHY

Dr. Gregory Pawloski

August, 2018

Acknowledgements

I would like to say a huge thank you to my mom, Galina, who was the first person to introduce me to the science world with small math questions and talks about stars and galaxies, to my dad, Sergey, who opened a gate to the world of physics competitions and provided the best resources to learn math and physics, and to my wife, Nina, who was always supporting and believing in me. I could not achieve all of my goals without you.

I want to say thank you to my adviser Gregory Pawloski for giving me this project, teaching and sharing his wisdom in experimental physics research. Thank you to my former officemates Susan, Dominick, Andrew and Jarrett with whom I shared the joy of working in NOvA and traveling to collaboration meetings, who helped me a lot when I struggled. Thank you to our post-docs Matthew and Aaron for sharing their expertise and ideas.

A big thank you to my friends Yevhen, Mike, Sean, Yahor, Mitya, Olesya, Sergey, Timur, Vera for sharing with me countless hours of working through coursework, papers, traveling around US and making my life easier and enjoyable. You are the best friends one can dream of.

And last but not least, I would like to thank you entire NOvA collaboration who make this work possible, especially Alex Himmel, Bruno Zamorano and Jeremy Wolcott. You taught me skills which were immensely important at the last stage of my work.

Dedication

To my parents, Sergey and Galina, and my loving wife Nina.

Abstract

The NuMI Off-axis ν_e Appearance (NOvA) experiment studies neutrino oscillations in the NuMI (Neutrinos at the Main Injector) beam. The goal of the experiment is to determine the mass hierarchy and measure δ_{CP}, however it is also sensitive to $\sin^2\theta_{23}$, and Δm_{32}^2. The present work tries to improve experimental sensitivity to the oscillation parameters by considering neutrino events which are discarded by the previous analysis — escaping events. The biggest issues with the escaping sample are significant cosmic background and correct energy estimation. Both issues were addressed and inclusion of escaping sample to the final fit led to an effective increase of statistics by 4% with best-fit measurements of $\sin^2\theta_{23} = 0.504$ and $\Delta m_{32}^2 = 2.45 \times 10^{-3}$ eV^2.

Contents

List of Tables

List of Figures

Chapter 1

Introduction

The goal of this work is to study and understand properties of one of the most mysterious elementary particles in the universe - neutrinos. Neutrinos are electrically neutral, and are lighter than all other fundamental particles by many orders of magnitude. It is known that neutrinos could interact only through weak and gravitational forces which leads to a several light years of mean free path in the matter for 1 MeV neutrinos. Despite their tiny mass and weak interactions with matter, they are very interesting to the elementary particle physics, cosmology, and astrophysics communities. Neutrinos carry away almost all energy of supernova explosion, and can reveal a lot about a dying star's internal structure and the last seconds of its life. Neutrino telescopes may open a new window for Universe observation and give a unique look into phenomena which could not be seen by conventional telescopes. Neutrinos also can direct physicists towards potential signs of new physics that can be investigated at collider experiments [3] and in the galaxy. The list of examples why neutrinos are important continues to grow, and it gives a sense that neutrino physics is a very rich and interesting subject to study.

A hallmark of the weak force is oscillations between flavors. Oscillations were first discovered in neutral mesons, and later in neutrinos [4, 5, 6, 7, 8, 9]. After travelling some distance, neutrinos produced in one flavor oscillate into a different flavor, and this repeats until a neutrino emits a charged weak boson and becomes a charged lepton. The NOvA - NuMI[1] Off-axis Neutrino Appearance - experiment was designed to

---
[1]Neutrino at the Main Injector

study properties of these oscillations. There are several parameters which fully describe neutrino oscillations. Analysis presented in this work is focused on measuring $\sin^2 \theta_{23}$ and $|\Delta m^2_{32}|$. The measurements come from studying a specific mode of the oscillations: $\nu_\mu \to \nu_\mu$.

Here is a brief outline of the work

- Chapter 2 briefly presents the history of neutrino discovery and observation of neutrino oscillations.

- Chapter 3 discusses corresponding theory behind the neutrino oscillation physics together with the current measurements of the parameters describing these oscillations.

- Chapter 4 describes the NOvA experiment design and its two most significant parts - Far and Near Detectors.

- Chapter 5 provides details on Monte Carlo simulations used in the analysis.

- Chapter 6 follows the reconstruction chain from raw data to high level objects such as slices, tracks, etc. Energy estimation algorithm is considered.

- Chapter 7 presents selection criteria for the contained sample as well as selection and background reduction processes for the escaping sample excluded in previous analyses.

- Chapter 8 discusses different approaches to escaping sample energy estimation algorithm.

- Chapter 9 gives predictions for the selected events in Far Detector

- In Chapter 10 all the systematics are discussed.

- Chapter 11 presents results of the analysis developed in the thesis.

- Chapter 12 summarizes the work presented in the thesis.

Chapter 2

Neutrino and its oscillation

2.1 History of neutrino discoveries

The energy spectrum of electrons in beta decay was first accurately measured by James Chadwick in 1914 [10]. Previous attempts by Lise Meitner and Otto Hahn in 1911 and Jean Danysz in 1913 showed hints that the electron energy spectrum was continuous. At the time this was an obvious contradiction with laws of energy and angular momentum conservation. A nucleus emitting an electron changes its state and energy of the electron should be equal to the energy difference of two nucleus' states. After several attempts to explain the mystery of beta decay Wolfgang Pauli postulated [11] that beta decay is actually a three particle decay. He called the third particle "neutron" - an electrically neutral and very light particle - and it was responsible for carrying away some portion of the energy which leads to continuous electron energy spectrum. Two years later in 1932 an actual neutron - the proton's partner inside a nucleus - was discovered by Chadwick [12]. To avoid confusion Enrico Fermi proposed a new name for Pauli's particle [13] - neutrino, which means "little neutral one".

It took more than 20 years for the first neutrino to be observed. In 1956 Reines and Cowan made a direct observation of a neutrino [14], whose flavor was later recognized as an electron anti-neutrino $\bar{\nu}_e$. An anti-neutrino was produced in a nuclear fission reactor via neutron decay

$$n \rightarrow p + e^- + \bar{\nu}_e. \tag{2.1}$$

An anti-neutrino interacted with a proton in a detector and produced positron and neutron

$$\bar{\nu}_e + p \rightarrow e^+ + n. \tag{2.2}$$

The signature of both processes, and thus evidence of the neutrino, was observed using a detector in the following way. An anti-neutrino interacted with a proton to produce a positron and neutron. The positron annihilated with an electron and produced two photons. Shortly after the neutron was captured by a nucleus and emitted several photons. Two photons followed by a third one gave an indication of a neutrino interaction inside the detector. The Nobel Prize was awarded to Reines in 1995 for the detection of the neutrino.

In 1962 the neutrino family was expanded by observation of the second type of neutrino - a muon neutrino ν_μ. Leon Lederman, Melvin Schwartz, and Jack Steinberger used the world's largest accelerator at that time at Brookhaven National Laboratory to direct protons onto a fixed target to produce charged pions. Those pions subsequently decayed to (anti)muons and muon [anti]neutrinos. At the end of pion decay pipe plates made of steel and lead were installed to absorb muons. Beyond the metal absorbers a spark chamber was placed to identify neutrino interactions similar to (2.2),

$$\nu_\mu + n \rightarrow \mu^- + p, \qquad \bar{\nu}_\mu + p \rightarrow \mu^+ + n. \tag{2.3}$$

After processing all experimental data, 34 neutrino interactions were found with a single muon track in the spark chamber [15]. Absence of observed electrons in the chamber proved that $\nu_\mu \neq \nu_e$ and lead the fact that in 1988 the group was awarded the Nobel Prize for their discovery of the muon neutrino.

The discovery of weak gauge bosons at CERN by UA1 and UA2 collaborations [16], [17] in 1983 provided new ways to study particles interacting via weak bosons. Careful measurements of the Z boson decay rates helped to establish the total number of neutrinos which interact through $W^\pm$ and Z bosons. ALEPH detector on the CERN Large Electron Positron collider determined [18] in 1989 that only three different neutrinos participate in weak interactions. Sterile neutrinos, which do not interact weakly, have not been found but are still being searched for.

The ALEPH experiment suggested that a third neutrino should be associated with

the tau lepton, which was discovered in 1975 [19]. The Direct Observation of Nu Tau (DONUT) experiment was setup at Fermilab in 2000 and looked for reactions

$$\nu_\tau + n \to \tau^- + p, \qquad \bar{\nu}_\tau + p \to \tau^+ + n. \tag{2.4}$$

The general idea of the DONUT experiment was similar to the experiment conducted at Brookhaven National Lab in the early 1960s. A proton beam was directed into a fixed target resulting in a shower of meson and baryons. In order to decrease the background of ν_μ neutrinos, deflecting magnets were installed along the decay pipe to remove muons which produce ν_μ neutrinos upon decaying. Tau neutrinos were produced through $D_S \to \tau + \nu_\tau$ process, and as many as 4 tau neutrino interactions were observed [20]. This number of interactions was sufficient to confirm the existence of the tau neutrino.

2.2 Neutrino oscillations

The idea of neutrino oscillations was suggested in the work of Bruno Pontecorvo in 1957 [21]. Although at the time only one neutrino flavor was known, Bruno described the mixing of electron neutrinos and antineutrinos. Later, when the muon neutrino was discovered, the physicists Maki, Nakagawa, and Sakata used Pontecorvo's framework [22] to describe neutrino flavor oscillations. After the discovery of the tau neutrino, a third neutrino was added to the oscillation picture.

Before Ray Davis and collaborators' observation of solar neutrino deficit in the 1960's [23], neutrino oscillations were considered possible but hardly realistic. Using the standard solar model the total number of electron neutrino coming from the sun was predicted by John Bahcall [24]. However, an obvious deficit of solar neutrinos was measured. Later, more precise measurements of solar neutrino flux were made in Japan - Super-Kamiokande [25], and in Sudbury Neutrino Observatory [26] in Canada. Both observations matched prior results, but contradicted predictions. This solar neutrino problem is elegantly explained in the framework of neutrino oscillations. In the following section a theoretical description of neutrino oscillations will be given.

Chapter 3

Physics of Neutrinos

3.1 Standard Model in a nutshell

Since ancient times people were trying to understand the world around them. From first world models of ancient Greeks to modern theories scientists tried to use limited number of entities to describe phenomena happened in nature - Democritus's indivisible atoms, Plato's elements (air, fire, water, earth) or elementary particles of the Standard Model. Here we focus on the latest and most accurate theory - the Standard Model.

Elementary particles of the Standard Model are the building blocks of matter, and the glue of everything we can see around us[1]. However, the most fascinating thing about the Model is that underlying principles that governs it are symmetries - gauge symmetry and Lorentz symmetry. The Standard Model group is

$$SU(3) \times SU_L(2) \times U(1), \tag{3.1}$$

where the $SU(3)$ group describes strong interactions, and the $SU_L(2) \times U(1)$ group describes electro-weak interactions[2]. The different mathematical properties of the groups

---

[1]As of today, Standard Model and Einstein's General Theory of Relativity could not fully explain motion of galaxies and exponential expansion of the Universe. Two more entities were introduced - dark matter for former phenomenon and dark energy for latter one.

[2]Gravitational interaction falls out of the picture since for the last one hundred years gravity is described by deformation of space-time continuum. Nevertheless, the attempts to rewrite gravity using the same language of groups and unified it with Standard Model never were given up. In fact, all latest unified theories were based on groups of high dimensions such as String Theory.

Standard Model of Elementary Particles

Figure 3.1: Elementary Particles in the Standard Model.

All particles could be divided into 2 groups: fermions and bosons. Fermions are further divided into quarks with fractional charges and leptons - charged ones (e, μ, τ) and neutral $(\nu_e, \nu_\mu, \nu_\tau)$. The fermions participate in strong (except leptons), weak and (only charged ones) electromagnetic interactions. These interactions are mediated by massless gluons (g), massive weak bosons $W^{\pm}$ and Z^0 and massless photon (γ). The Higgs boson is last discovered particle and is responsible for all fundamental particles' masses. However, the source of the neutrino mass is unknown and it is possible that Higgs mechanism is not working for neutrino mass generation.

naturally split the particles into two categories based on their spins: bosons and fermions. Fermions are particles with half-integer spin and bosons are particles with integer spin (in units of $\hbar$). The matter consists of fermions, while bosons serve for carrying interactions between matter particles.

Fermions in the Standard Model are quarks and leptons. Quarks make up protons and neutrons and have fractional electric charge - up, charm and top quarks have charge $+\frac{2}{3}e$, while down, strange and bottom have $-\frac{1}{3}e$. Quarks also have strong charge - color - which could be one of three options: green, red or blue. The interesting fact is that the quarks are not observable in the same sense as electrons could be observable and only three quark (baryon) or quark-antiquark (meson) combinations exist[3]. This phenomenon is called quark confinement with no complete explanation as of today.

The other sector of the Standard Model - the lepton sector - consists of negatively charged electron, muon and tau particles as well as neutral neutrinos. These particles participate only in weak and electromagnetic interactions. Moreover, the electron and electron neutrino carry an electron lepton number, similar quantities are carried by muon and tau leptons. Lepton numbers are known to be conserved in almost[4] every process, for example, muon decay produces not only electron but corresponding muon neutrino and electron antineutrino. Although attempts to observe lepton number violation, beside neutrino oscillation, are being made.

As shown in figure (3.1), fermions are split into three generations. The mass of each subsequent generation is bigger by at least two orders of magnitude, except for neutrinos, whose masses are extremely hard to measure directly or indirectly but they are believed to be in the below 1 eV region[5]. The matter we observe around us is made of particles from first generation. Why do other generations exist? Why are there only three generations? What mechanism generates neutrino masses? Physicists do not know the answer to this questions, nor why there is a gigantic (10^{11}) mass difference between the lightest and the heaviest particles.

The last but not the least sector of the Standard Model is boson sector. This sector is represented by particles which mediate electromagnetic, weak and strong interactions. The photon (γ) is spin-1 massless carrier of the electromagnetic force and is responsible

---

[3]Recently, five quark combinations have been discover

[4]The lepton number is not conserved in the case of neutrino oscillation which this thesis is about.

[5][27] summarizes recent attempts to measure neutrino mass directly

for almost all phenomena that a person experiences in their life - from the Sun's light, to the frictions and atomic bonds between chemical elements. Only charged particles interact through photon exchange.

The strong force carrier is spin-1 massless gluon (g). Gluon exchange binds quarks into stable states as baryons - protons, neutron etc.- or mesons - π, ρ etc. While the photon is electrically neutral and can not interact directly with other photons, gluon carries a color, or rather color-anticolor, and can interact with other gluons. As mentioned earlier, only specific combinations of quarks are observable - colorless combinations - three quarks of different colors, or quark-antiquark pairs with color-anticolor charge. In strong interaction quark changes its color by emitting gluon, for example, a blue quark emits blue-antired gluon and becomes a red quark.

The weak force carriers are spin-1 massive $W^{\pm}$ and Z^0 bosons. All the Standard Model fermions can interact via weak bosons exchange. The weak interaction plays a major role in radioactive decays and fusion processes, and are the only way to study neutrinos since these particles do not participate in strong or electromagnetic interactions.

Among Standard Model interactions only electromagnetic one has an infinite range while others are short range interactions due to massive (weak) and color charged (strong) force carriers. The relative strength of interactions are not very meaningful as it depends on energies one uses for measurements but still can provide useful information. Strong, electromagnetic and weak interactions relate to each other as $1 : 10^{-3} : 10^{-16}$.

The masses of particles and the interaction strengths are free parameters of the Standard Model, and can be chosen so that the theory's predictions match experimental observations. The fact that weak bosons are massive makes it difficult to incorporate them into the theory due to gauge symmetry. However, the Higgs mechanism accomplishes this in an elegant way by introducing the Higgs field and a corresponding carrier - the Higgs boson. The Higgs boson is the last fundamental particle of the Standard Model and is the only one with spin-0.

In addition, each particle has an antiparticle with the same mass and spin but opposite charge. Interaction between the particle and its antiparticle leads to annihilation with two photons being emitted [6]. It is known from measuring light element abundances

---

[6]also pairs of Z^0 or $W^{\pm}$ could be emitted for sufficiently high energies in the CM reference frame

in the early Universe that our Universe consists primarily of matter and not antimatter with baryon-to-photon ratio ($\eta_B = \frac{n_B - n_{\bar{B}}}{n_\gamma}$) between 4.7 and 6.5×10^{-10} [28]. Why the asymmetry materialized in the early Universe is still a mystery, however, CP-symmetry[7] violation is partially responsible for this and NOvA experiment can shed some light on the problem.

3.2 Oscillations in Vacuum

Neutrinos are massive elementary particles which only participate in weak interactions and are immune to electromagnetic and strong interactions. They also participate in gravitational interactions, but since gravity is many orders of magnitude smaller in comparison to other forces one can neglect gravity effects completely, at least on energy scale of modern experiments. There are three types of neutrinos - with definite flavor - electron (ν_e), muon (ν_μ) and tau (ν_τ) neutrinos. These flavor neutrinos are eigenstates of the weak Hamiltonian and they can be produced or destroyed only in weak interactions via exchange of the weak gauge bosons $W^\pm$ and Z. The neutrino mass eigenstates do not coincide with flavor eigenstates, and this leads to neutrino oscillations.

Weak interactions produce definite flavor neutrinos, but neutrinos propagate through space based on their mass eigenstates. The flavor eigenstates ($|\nu_e\rangle$, $|\nu_\mu\rangle$, $|\nu_\tau\rangle$) can be decomposed into linear combinations of mass eigenstates ($|\nu_1\rangle$, $|\nu_2\rangle$, $|\nu_3\rangle$).

$$|\nu_f\rangle = \sum_{i=1,2,3} U_{fi}|\nu_i\rangle. \tag{3.2}$$

The matrix U_{fi} is a 3×3 unitary matrix and is called the lepton mixing matrix or PMNS (Pontecorvo, Maki, Nakagawa, Sakata) matrix. U_{fi} encapsulates the neutrino mixing angles θ_{12}, θ_{13}, θ_{23} and phase δ that represents the degree of CP violation in the weak interactions. A convenient parametrization is as follows:

$$U_{fi} = \begin{pmatrix} c_{12}c_{13} & s_{12}c_{13} & s_{13}e^{-i\delta} \\ -s_{12}c_{23} - c_{12}s_{23}s_{13}e^{i\delta} & c_{12}c_{23} - s_{12}s_{23}s_{13}e^{i\delta} & s_{23}c_{13} \\ s_{12}s_{23} - c_{12}c_{23}s_{13}e^{i\delta} & -c_{12}s_{23} - s_{12}c_{23}s_{13}e^{i\delta} & c_{23}c_{13} \end{pmatrix}, \tag{3.3}$$

---

[7]Charge-Parity symmetry - $q \to -q, \quad \vec{r} \to -\vec{r}$.

where $c_{ij} = \cos(\theta_{ij})$ and $s_{ij} = \sin(\theta_{ij})$.

Quantum mechanics explains how the mass eigenstates propagate through space. Using the Schrodinger equation $-i\hbar \frac{\partial}{\partial t}|\psi\rangle = H|\psi\rangle$ one can derive a solution for neutrino wave function at the point (x, t) of space-time starting with the wave function at the point $(0, 0)$. Using the free Hamiltonian for neutrino mass eigenstates, one derives [8]

$$|\nu_i(x,t)\rangle = e^{-i(E_i t - p_i x)}|\nu_i(0,0)\rangle. \tag{3.4}$$

The neutrino masses m_i are much less in comparison neutrino energy in all experiments and an ultra-relativistic approximation could be used

$$p_i = \sqrt{E_i^2 - m_i^2} \approx E_i - \frac{m_i^2}{2E_i}, \tag{3.5}$$

moreover, in this limit neutrinos travel at nearly the speed of light, so final solution for neutrino wave function with the mass m_i is

$$|\nu_i(L)\rangle = e^{-i\frac{m_i^2}{2E}L}|\nu_i(0)\rangle, \tag{3.6}$$

where L is distance which the neutrino traveled.

Given a neutrino of flavor f at $t = 0$ and energy E, the probability that the neutrino oscillates into a flavor f' a distance L from its initial position is

$$P_{\nu_f \to \nu_{f'}}(L, E) = |\langle \nu_f(0)|\nu_{f'}(L)\rangle|^2$$

$$= \left|\left(\sum_i \langle \nu_i(0)|U_{fi}^*\right)\left(\sum_{i'} e^{-i\frac{m_{i'}^2}{2E}L}U_{f'i'}|\nu_{i'}(0)\rangle\right)\right|^2$$

$$= \left|\sum_i U_{fi}^* U_{f'i} e^{-i\frac{m_i^2}{2E}L}\right|^2$$

$$= \sum_{i=1}^{3}\sum_{j=1}^{3} U_{fi}^* U_{f'i} U_{f'j}^* U_{fj} e^{-i\frac{\Delta m_{ij}^2}{2E}L}, \tag{3.7}$$

---

[8]Natural units are used everywhere.

where standard notation $\Delta m_{ij}^2 = m_i^2 - m_j^2$ was used. The final expression simplifies to

$$P_{\nu_f \to \nu_{f'}}(L, E) = \delta_{ff'} - 4 \sum_{i > i'} \mathfrak{Re}(U_{fi} U_{fi'}^* U_{f'i'}^* U_{f'i}) \sin^2 \left(\frac{\Delta m_{ij}^2}{4E} L \right) +$$

$$+ 2 \sum_{i > i'} \mathfrak{Im}(U_{fi} U_{fi'}^* U_{f'i'}^* U_{f'i}) \sin \left(\frac{\Delta m_{ij}^2}{2E} L \right). \qquad (3.8)$$

It is worth noting that the oscillation probabilities depend on neutrino mass difference squared, therefore all neutrino oscillation experiments are sensitive only to Δm_{ij}^2. Also, in the case of a CP violation phase $\delta = 0, n\pi$ [9] the last term in (3.8) disappears and the oscillation probabilities are identical for neutrinos and antineutrinos. For the purpose of the experiment it is convenient to have the last equation when Δm_{ij}, E and L are expressed in eV^2, GeV and km respectively

$$\frac{\Delta m_{ij}^2}{2E} L \quad \to \quad 1.267 \frac{\Delta m_{ij}^2 [eV^2]}{E[GeV]} L[km] = \Delta_{ij}. \qquad (3.9)$$

The NOvA experiment is used to measure the probabilities of muon neutrino disappearance and electron neutrino appearance

$$P_{\nu_\mu \to \nu_\mu}(L, E) \approx 1 - \sin^2 2\theta_{23} \sin^2 \Delta_{32}, \qquad (3.10)$$

$$P_{\nu_\mu \to \nu_e}(L, E) \approx P_{atm} + P_{sol} + 2\sqrt{P_{atm} P_{sol}}(\cos \Delta_{32} \cos \delta \mp \sin \Delta_{32} \sin \delta), \qquad (3.11)$$

with

$$P_{atm} = \sin^2 \theta_{23} \sin^2 2\theta_{13} \sin^2 \Delta_{31}, \qquad P_{sol} \approx \cos^2 \theta_{23} \cos^2 \theta_{13} \sin^2 2\theta_{12} \Delta_{21}^2, \qquad (3.12)$$

where the "-" sign in 3.11 is for the neutrino and the "+" sign is for the anti-neutrino.

3.3   Oscillations in Matter

Each neutrino studied by the NOvA experiment travels more than 810 km through the Earth's crust. While propagating through the earth, neutrinos interact with matter,

---

[9] $n = 1, 2, 3, ...$
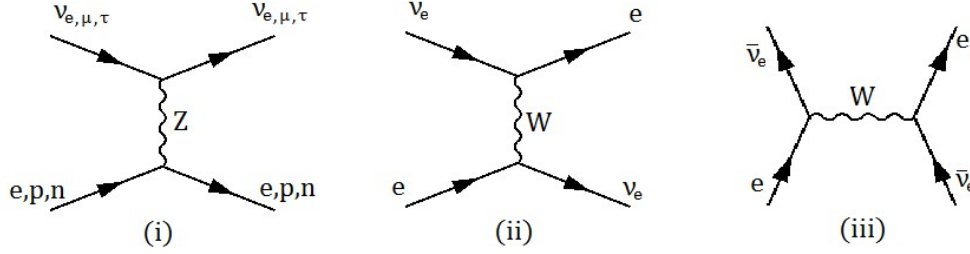
Figure 3.2: Neutrino interaction with matter. (i) All neutrinos participate in NC interactions which leads to additional effective mass for all eigenstates ν_1, ν_2 and ν_3, (ii) Additional CC interaction for electron neutrino ν_e, which modifies mass square difference, (iii) effect similar to (ii) only for electron anti-neutrino $\bar{\nu}_e$. The diagram (iii) contributes with opposite sign in comparison to (ii).

and these interactions distort the neutrino oscillations. Since interaction going through exchange of only weak gauge bosons there are two types of possible interaction: (i) neutrino emits Z boson - neutral current (NC) interaction and (ii) neutrino emits $W^{\pm}$ boson - charged current (CC) interaction. In matter, all three flavors of neutrinos interact through the exchange of Z boson with electrons, protons and neutrons. For electron neutrino there is another possibility - interaction through exchange W^{+} boson with electrons, as illustrated in figure 3.2. Interactions of ν_μ and ν_e through W^{+} change initial state, and thus could not be considered as matter effect.

Accounting for interactions between neutrinos and the Earth adds two additional terms to the Hamiltonian which describes neutrino propagation - an effective potential,

$$V_C = \sqrt{2}G_F N_e \quad \text{and} \quad V_N = -\frac{1}{\sqrt{2}}G_F N_n, \quad (3.13)$$

where G_F is Fermi constant, N_e and N_n electron and neutron number density respectively. The second term effectively shifts all $m_i^2 \rightarrow m_i^2 + 2|\mathbf{p}|V_N$ and does not have an effect on Δm_{ij}. The first term V_C enters the Hamiltonian in a such way that it only affects the electron neutrino ν_e and electron anti-neutrino $\bar{\nu}_e$. After further calculations one derives the following corrected expressions for Δm_{32} and $\sin 2\theta_{13}$ in the presence of matter

$$\Delta m_{32}^2\Big|_{mat} = \sqrt{(\Delta m_{32}^2 \sin 2\theta_{13})^2 + (\Delta m_{32}^2 \cos 2\theta_{13} \mp 2E_\nu V_C)^2}$$
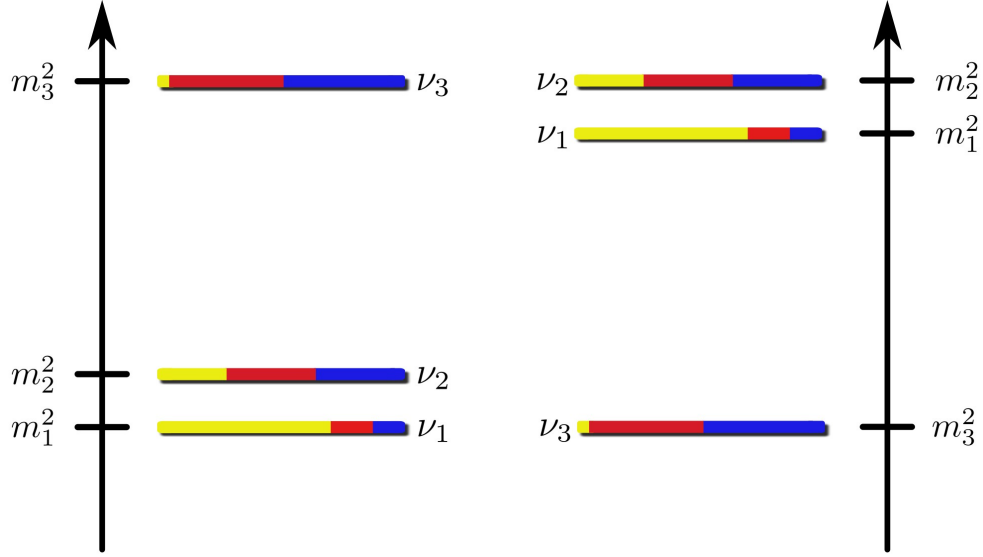
Figure 3.3: Two possible variants of neutrino mass hierarchies. The left side corresponds to the normal hierarchy (NH) and right side corresponds to the inverted hierarchy (IH). Colors represent how much and what kind of neutrino flavors contribute to every mass state. The electron flavor is yellow, muon flavor is red and the tau flavor is blue.

$$\sin 2\theta_{13}\Big|_{mat} = \frac{\Delta m_{32}^2 \sin 2\theta_{13}}{\sqrt{(\Delta m_{32}^2 \sin 2\theta_{13})^2 + (\Delta m_{32}^2 \cos 2\theta_{13} \mp 2E_\nu V_C)^2}} \tag{3.14}$$

The matter effect has a significant influence on the ν_e appearance probability, and in the first approximation

$$P_{\nu_\mu \to \nu_e}(E, L)\Big|_{mat} = \left(1 \pm \frac{2E_\nu V_C}{\Delta m_{32}^2}\right) P_{\nu_\mu \to \nu_e}(E, L), \tag{3.15}$$

where the "+" sign is for the neutrino and the "-" sign is for the antineutrino. This effect is known as the Mikheyev-Smirnov-Wolfenstein (MSW) effect, and for the NOvA experiment it plays an important role in measuring the CP violating phase δ_{CP}.

Similar one can get matter effect on the ν_μ disappearance probability in the first approximation

$$P_{\nu_\mu \to \nu_\mu}(E, L)\Big|_{mat} = P_{\nu_\mu \to \nu_\mu}(E, L) \pm LV_C \sin^2 2\theta_{23} \cos 2\theta_{13} \sin\left(\frac{\Delta m_{32}^2}{E}L\right), \tag{3.16}$$

and since most of NOvA sensitivity in measuring $\sin^2 \theta_{23}$ and Δm_{32}^2 comes from the

energy region of maximum ν_μ disappearance for neutrino energy $E = \frac{\Delta m_{32}^2}{\pi} L$ one can see that the matter effect does not play any role in the first approximation.

It is worth noting that assigning specific masses to specific mass eigenstates are completely arbitrary, but it is known from experimental data that two masses are much closer to each other in comparison with the third mass. These two masses are called m_1 and m_2, with $m_2 > m_1$ and $\Delta m_{12} << |\Delta m_{32}| \approx |\Delta m_{31}|$. However, the sign of Δm_{32} is still unknown. That leaves two possibilities, called the normal hierarchy (NH) and the inverted hierarchy (IH). Figure 3.3 illustrates the neutrino mass distributions. The NOvA experiment will be able to determine which hierarchy is realized in nature.

3.4   Mixing Parameters Values

Parameters which enter neutrino oscillation picture have to be determined experimentally. Table 3.1 shows the most recent, best fit measurements obtained in numerous experiments. Two mass differences are measured and the measurements are making Figure 3.3 to be not to scale. All three mixing angles are also measured; it turns out that the third mass state almost does not have a contribution of electron flavor (θ_{13} is relatively small) and has almost equal contribution from muon and tau flavors (θ_{23} is close to $\frac{\pi}{4}$). From a theoretical point of view, the latter fact is very intriguing because the exact equality of θ_{23} and $\frac{\pi}{4}$ could reveal some hidden symmetries in the lepton sector of the Standard Model. Measurements of δ_{CP} comes with a big uncertainty, however the uncertainty gets smaller as more data is gathered.

The primary goal of NOvA is to determine mass hierarchy and δ_{CP}, but it is also sensitive to θ_{23} and m_{32}^2. If nature prefers non-maximal mixing i.e., $\theta_{23} \neq \frac{\pi}{4}$, NOvA may be able to determine octant[10]. In the current analysis, θ_{23} and Δm_{32}^2 are measured.

---

[10]Upper octant if $\theta_{23} > \frac{\pi}{4}$ and lower octant if $0 < \theta_{23} < \frac{\pi}{4}$.

Parameter	Best Fit Value
$\Delta m^2_{21}, 10^{-5}eV^2$	7.53 ± 0.18
$|\Delta m^2_{32}|, 10^{-3}eV^2$	$2.45 \pm 0.05 \quad (2.52 \pm 0.05)$
$\sin^2(\theta_{12})$	$0.307^{+0.013}_{-0.012}$
$\sin^2(\theta_{23})$	$0.51 \pm 0.04 \quad (0.50 \pm 0.04)$
$\sin^2(\theta_{13})$	0.0210 ± 0.0011
δ_{CP}/π	$0.0 - 2.0 \quad (0.0 - 0.1, \ 0.5 - 2.0)$

Table 3.1: Best fit values for the mixing parameters from latest edition of the Particle Data Group [1]. Values in parenthesis are stated for the assumption of the inversed mass hierarchy, when no values in parenthesis are given that mean their are free of mass hierarchy assumption. The best fit values are given with 90% CL.

Chapter 4

The NOvA Experiment

The neutrinos studied by NOvA begin at Fermi National Accelerator Laboratory (Fermilab) in Illinois. An intense muon (anti-)neutrino beam is created at Fermilab by the Neutrino at the Main Injector (NuMI) source [29]. NOvA, which stands for NuMI Off-Axis ν_e Appearance, is a long baseline experiment which is designed to determine the neutrino mass hierarchy, the octant of θ_{23}, and to measure the CP violating phase δ_{CP}. It consists of the Near Detector (ND), which is located at Fermilab and measures the combined flux of the neutrino beam and interaction cross section, and the Far Detector (FD), which is located near Ash River, Minnesota and measures interaction yield of muon and electron neutrinos. The structures of the NuMI source and the Near and Far Detectors, and the detector positions relative to the beam axis will be explained in the following sections.

4.1 NuMI and Off-Axis Detectors Position

Neutrinos for the NOvA experiments comes from decay of pions and kaons. To get a beam of meson the Main Injector at Fermilab is used, which provides an intense beam of proton with energy 120 GeV. The structure of NuMI is illustrated on figure 4.1. It is designed to deliver 4.9×10^{13} proton on target (POT) with the repetition rate of 1.3s, which corresponds to 700 kW of beam power. The proton beam is directed into a graphite target. Collisions between the proton beam and graphite target produces many types of hadrons and mesons, with pions and kaons among them. Magnetic focusing
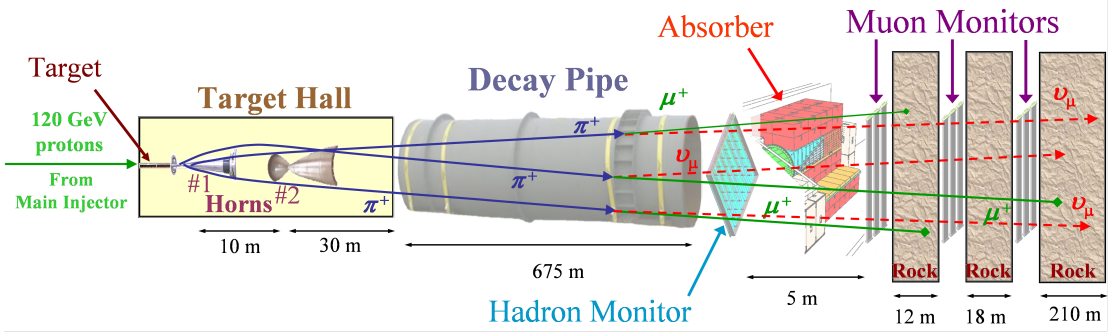
Figure 4.1: Schematics of neutrino production[2].

horns, which are supplied with current of 200kA, are used to focus and direct charged pions and kaons into a decay pipe. The decay pipe is long enough such that more than 99% of all pions and 63% of kaons decay into anti-muon/muon and muon/anti-muon neutrino, so the flux of particles at the end of the decay pipe consists of mostly muons and muon anti-neutrinos, or their antiparticles. By changing the electric current direction in the focusing horns one can switch between focusing positively or negatively charged pions and kaons into the decay pipe. This gives an opportunity to make two types of neutrino beams - ν_μ's and $\bar{\nu}_\mu$'s. Unfortunately, 5% of charged kaons and muons, those which decay in decay pipe, have electron neutrinos among their byproducts, and this is an irreducible background for an electron neutrino analysis. The rest of charged particles such as undecayed muons and electrons do not reach Near Detector as they get absorbed in rock. A hadron monitor, absorber and muon monitor are placed at the end of decay pipe to better understand beam properties, but they do not play any role in the NOvA experiment.

After the neutrinos leave the decay pipe they begin their journey to the near and far detectors. The NOνA detectors are placed 14.6 mrad off-axis of the NuMI beam for several reasons. As can be seen on the figure 4.2, the first minimum of the muon neutrino survival probability and first maximum of the electron neutrino appearance probability occur near 400 km/GeV. For this baseline of 810 km $P(\nu_\mu \to \nu_e)$ corresponds to 2 GeV of neutrino energy. Only a tiny fraction of neutrinos satisfies this condition if Far Detector stays on-axis of neutrino beam as shown in Figure 4.3 and there should be a way to fix that. The solution is simple: pions and kaons decay isotropically in their rest
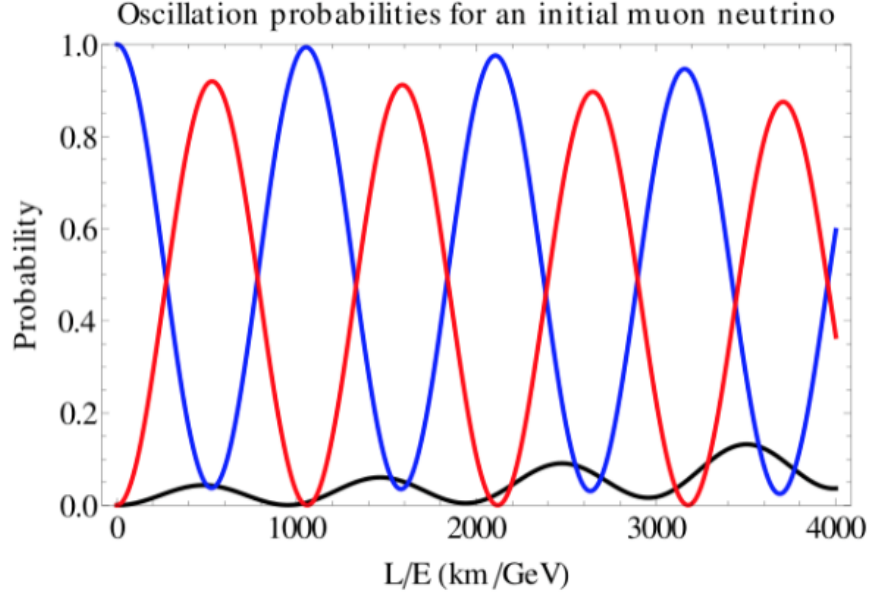
Figure 4.2: Neutrino oscillation probabilities.
Neutrino oscillation probabilities as a function of $\frac{L}{E}$, $P(\nu_\mu \to \nu_\mu)$ - blue line,
$P(\nu_\mu \to \nu_e)$ - black line and $P(\nu_\mu \to \nu_\tau)$ - red line.

frame, but, after a Lorentz boost to the laboratory frame, the neutrino flux and energy
at the Far Detector (for small off-axis angles θ) can be expressed in the following form

$$F = \left(\frac{2\gamma}{1 + \gamma^2\theta^2}\right)^2 \frac{A}{4\pi d} \tag{4.1}$$

$$E_\nu = \frac{0.43E_\pi}{1 + \gamma^2\theta^2}, \tag{4.2}$$

where $\gamma = \frac{E_\pi}{m_\pi}$, A is the size of the detector front area and d is the distance to the
detector. For kaons numerical factor 0.43 should be changed to 0.96. Knowing the
pion and kaon energy spectrum at the NuMI source, the neutrino energy spectrum at
the far detector for different off-axis angles θ can be predicted. As shown on the top
of figure 4.3, as θ increases the neutrino energy distribution gets narrower and shifts
toward lower energies. At 14.6 mrad the neutrino flux is still appreciable and peaks
near 2 GeV. Based on this configuration, the NOvA Far Detector is situated 810 km
from the source to measure the maximum of $P(\nu_\mu \to \nu_e)$. At this distance, the narrow

peak decreases the probability that neutral current (NC) events from more energetic neutrinos are misidentified as CC events in the energy region of interest[1]. In general, the off-axis detector placement significantly improves the sensitivity of the $P(\nu_\mu \rightarrow \nu_e)$ probability measurement.

4.2 NOvA Near and Far Detectors

The NOvA experiment uses two detectors for measuring muon neutrino disappearance probability $P(\nu_\mu \rightarrow \nu_\mu)$ and electron neutrino appearance probability $P(\nu_\mu \rightarrow \nu_e)$. In order to decrease systematic uncertainties, such as beam uncertainty and uncertainties due to variation in detector efficiency, two detectors are built with exactly the same material and similar technology. The Near Detector is placed 1 km from the NuMI source at Fermilab, while the Far Detector sits 810 km away on the surface and 14.6 mrad off beam axis in Ash River, Minnesota. The Near Detector weighs 330 metric ton and is 105 m underground, while the Far Detector mass is 14,000 ton and has shielding equivalent to 3 m of water which reduces cosmic ray background. The reason the Near Detector is underground is that on the ground NuMI source has to shoot the neutrino beam approximately 3.6 degrees below the ground level so it comes out of the Earth 810 km downrange.

4.2.1 Internal construction

Each detector is made of cells which are made from polyvinyl chloride (PVC) doped with titanium dioxide to increase light reflectivity. The cross section of cells has rectangular shape with sizes approximately equal to 4 cm and 6 cm. The length of the cells are varies between the detectors and is 4 m for the Near Detector and 15 m for the Far Detector. 32 cells are bound together along 6 cm side to make a module and a set of modules produces plane. The number of modules in a plane depends on a detector - 3 and 12 modules per plane for the Near and Far Detector respectively. Planes are glued together in a such way that adjacent planes alternating between horizontal and vertical alignment. The sketch of the detectors structure can be seen in 4.4b. Furthermore, 32

---

[1]For example, a 10 GeV neutrino after NC interaction can still have 8 GeV of energy and the rest of the energy is deposited in the detector as visible energy.
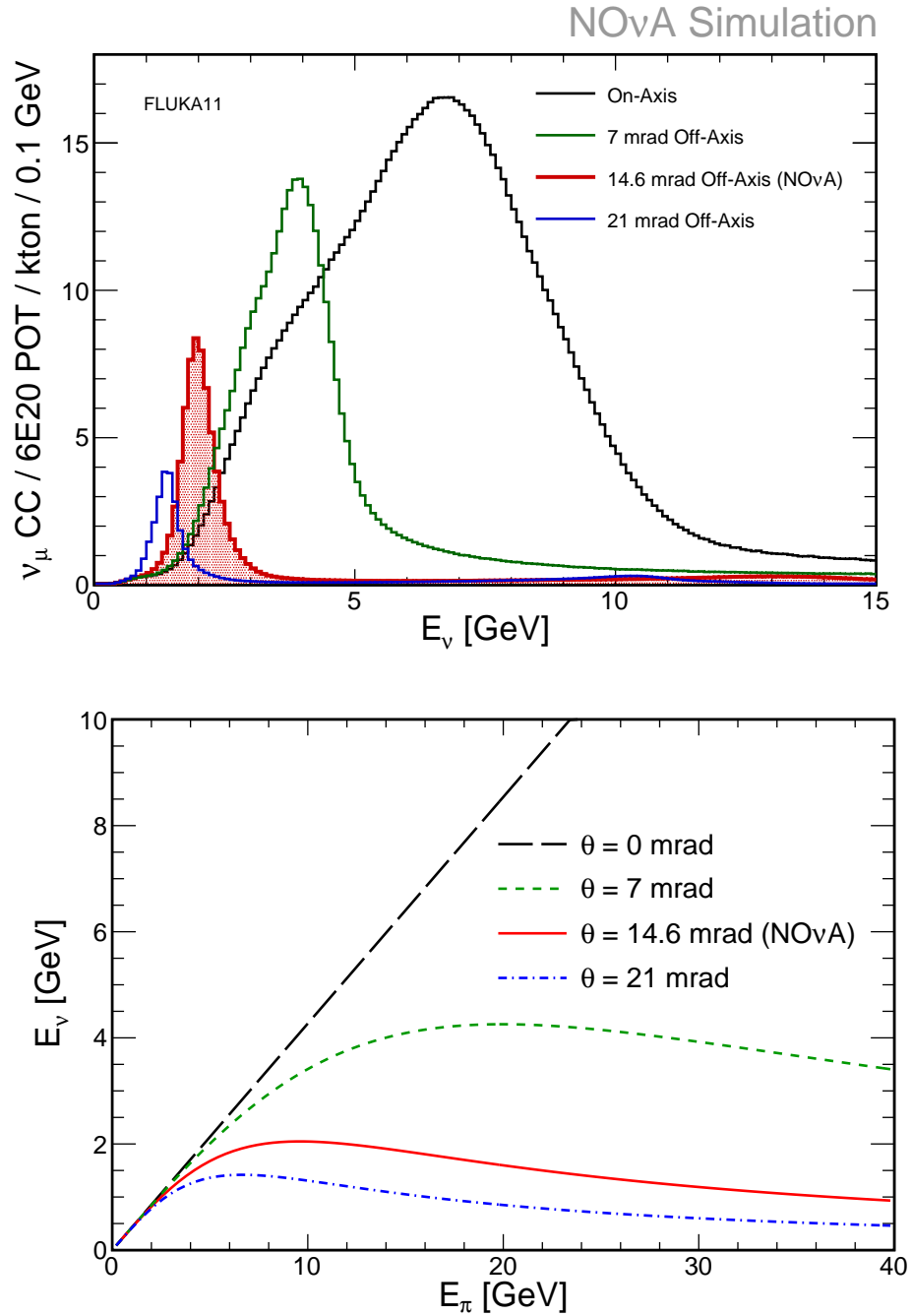
Figure 4.3: (Top) Expected unoscillated neutrino spectrum at the Far Detector as a function of angle relative to NuMI beam. (Bottom) Neutrino energy as function of pion energy (eq. 4.2) for different off-axis angles.

(a) A NOvA cell

(b) Scale and structure of the NOvA detectors
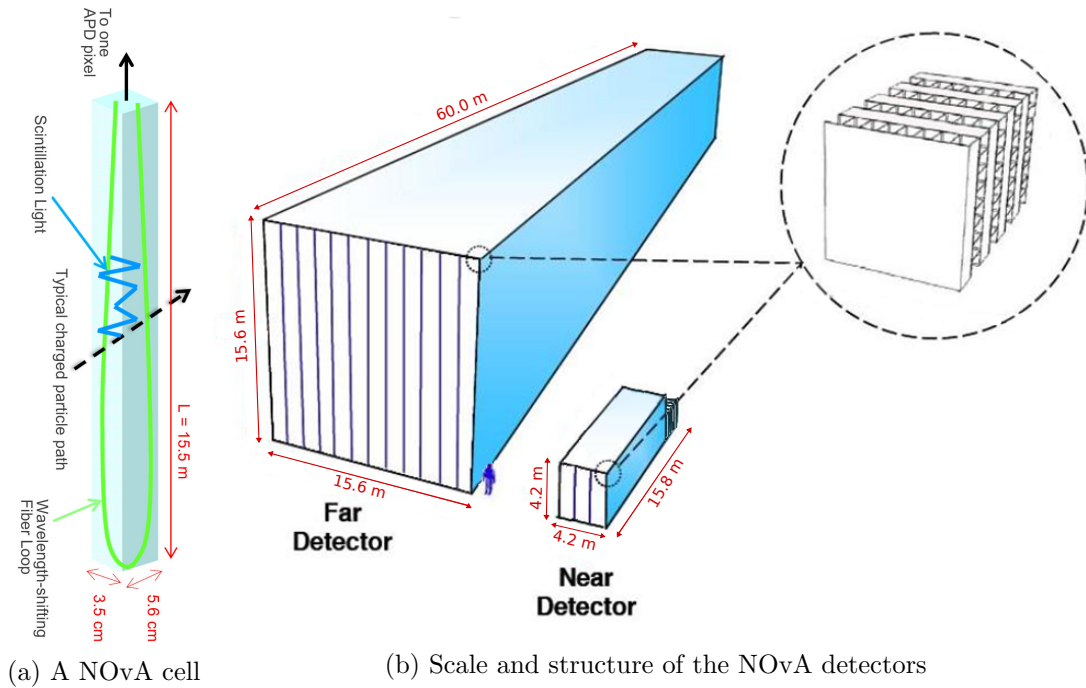
Figure 4.4: Structure of cell and the NOvA detectors

planes make up a block and 28 blocks complete the full Far Detector while for the Near Detector block consists of 24 planes and 3 blocks make the active part of the detector. In addition, so-called muon catcher block goes downstream of the Near Detector and serves for stopping muons which are produced in ν_μ CC interactions. The muon catcher, which helps to contain more muons as the relative size of the Near Detector is not big, consists of 22 active planes, with ten steel planes of 10 cm thickness interspersed between pairs of active planes. The size of the muon catcher in the XY plane is smaller than the active part of the Near Detector. The steel absorbs additional particle energy, and results in shorter muon tracks.

Using the planes configuration, three-dimensional particle tracks are reconstructed: vertical planes provide X measurements, horizontal planes provide Y measurements, and the Z measurements are extracted from the plane positions. The Z-axis is directed along the beam, the X-axis points to the west and the Y-axis points upward. This choice of axes results in a Cartesian right handed coordinate system.

4.2.2   Light production and digitization

In order to detect particles resulted in neutrino interactions in the detectors these particles should leave footprints. In NOvA experiment cells are filled with a liquid scintillator composed of mineral oil doped with pseudocumene [2]. In every cell, one wavelength shifting fiber runs from one end of the cell to the opposite end, then back to the other end where it connects to an avalanche photo diode (APD) as can be seen in 4.4a. Photons are created by charged particle moving through the scintillator. These reflected by the cell walls and have a high chance to be captured by the wavelength shifting fiber. Inside the fiber photons after absorption and reemission increase its wavelength resulting in propagation without escaping due to total inner reflection.

Photons that reach each APD are converted into a current of photoelectrons through the avalanche breakdown process. All 32 fiber of each module are connected to one APD. And the last step before signals might be processed with the help of conventional computers is to digitize the APD output signal. The digitization happens in front end board (FEB). Short APD signals are stretched in time in the Application Specific Integrated Circuit (ASIC) with the help of CR-RC circuit. After, the signal is passed to ADC - analog to digital converter - where continuous signal is converted to discrete, 12-bit signal that is read out every 500 (125) ns at the Far (Near) Detector, respectively. Only the 4 first ADCs - value of the digitization sample - are stored as a hit and the hit is written when the difference

$$ADC_i - ADC_{i-3} \tag{4.3}$$

is greater than a threshold. These 4 values are then passed to the Data Concentration Module (DCM). Later, those 4 values are used to fit the signal shape and to determine signal amplitude, which is proportional to amount of energy charged particle deposited in a particular cell.

4.2.3   Data acquisition

Every DCM is a custom built computer and collecting data from 64 FEBs. Data from the FEBs is sorted in time and arranged into 5 ms data blocks, then the data is sent

---

[2]1,2,4-Trimethylbenzene

to a buffer node where it is stored until a trigger decision is made to save the data permanently to the disks. 200 buffer nodes are arranged in a circular ring buffer and every node has up to a minute to run a trigger software until a new piece of data comes from a DCM. NOvA trigger software which issues trigger decisions relies on external triggers as well as data-driven triggers based on received data. Neutrino oscillation analyses use data which are recorded due to a timing trigger, this so-called NuMI trigger is issued by the acceleration complex at Fermilab. The trigger records 550 μs window of data centered around the 10 μs NuMI beam spill. There are several more triggers such as a cosmic trigger, which triggers at the rate of 10 Hz to store FD cosmic data for calibration and background estimation, and a supernova trigger, which should record up to 1 minute of data in the event of supernova burst.

The data selected by the triggers is stored temporarily at the FD and ND sites, and eventually transferred to Fermilab where it is processed for further analysis.

4.2.4   Neutrino Interactions in NOvA

The majority of neutrinos impinging on the NOvA detectors carry a few GeV energy, and all the charged products of a neutrino-nucleon interaction are clearly visible and can be individually tracked as long as their trajectories are sufficiently separated. As illustrated in figure 4.5 muons, electrons, and neutral pions produce a distinct signatures in NOvA. Particles primary lose their energy through an ionization process by disrupting electrons of atoms which happen to be close to particles trajectories. Being much heavier than an electron and immune to a strong interaction a muon can travel a long distance [3] inside the detectors which make it a relatively easy task to determine a high energy muon. Electrons interact with detector material electromagnetically, and quickly shower energy in a small conical region as opposed to a long muon track. Hadrons such as protons and charged pions lose energy through ionization and strong interactions with nucleons along their trajectories, and tend to travel much shorter distances than muons.

Despite these differences it is a complicated problem to distinguish a charged current (CC) interaction with a muon or electron being produced from a neutral current (NC) interaction where no visible lepton is produced. NC processes can produce charged or neutral pions with other hadrons. Charged pions leave tracks which could be confused

---

[3]Approximately 4.5 meters per 1 GeV of muon energy
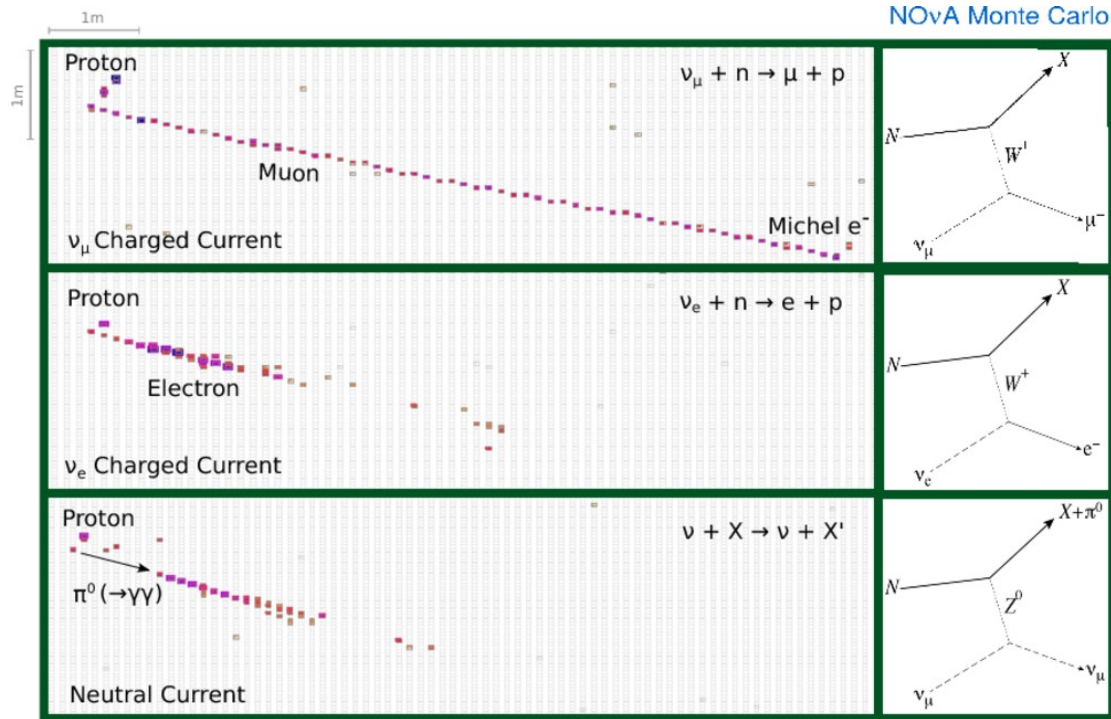
Figure 4.5: Neutrino interactions in NOvA detectors.

Three types of neutrino interactions are shown. The top part shows ν_μ CC interaction with some proton activity and long muon track left by high energy muon. The middle part shows ν_e CC interaction, electron develops a long electromagnetic shower with radiation length being much bigger than Moliere radius. The bottom part shows neutrino NC interaction with π^0 among the resulting particles which later produces an electromagnetic shower by decaying into two photons. NC type events form a primarily background in ν_e disappearance analysis.
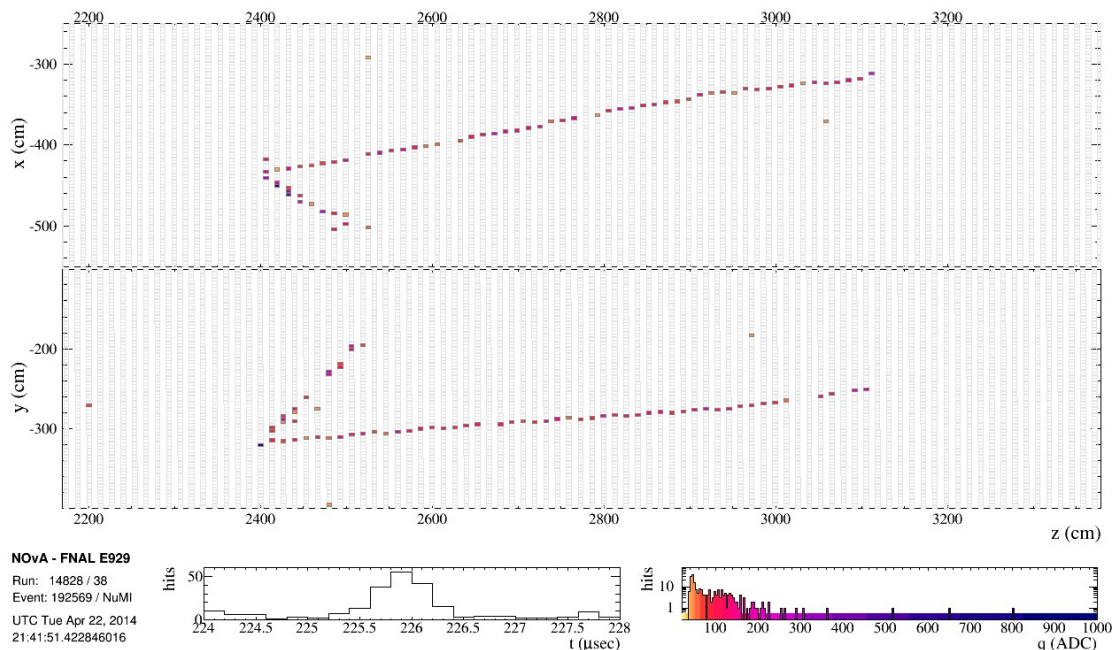
Figure 4.6: NOvA Event Display.
The candidate ν_μ CC event at the Far Detector zoomed in space and time. Top and bottom windows show X-Z and Y-Z projections.

with low energy muons, although occasional hard scatters with nuclei help with identification. Neutral pions decay into two photons and produce electromagnetic showers, and these showers can be mistaken with showers from electrons in CC interactions. Thus, sophisticated algorithms were developed to determine the exact neutrino flavor.

In addition, since the NOvA Far Detector sits on the ground it is constantly being bombarded by muons and other particles created by interactions of cosmic rays with air molecules in upper atmosphere. These muons contribute to a background for the main analysis but they are relatively easy to get rid off because of their activity at the top and/or at the sides of the detector and main analysis consider activity which is fully contained in the detector volume. However, cosmic muons are a primarily background in a escaping sample which this thesis is partially about.

4.2.5 NOvA Event Display

The NOvA event display helps to visualize data gathered by the detectors or a simulated one. The result of ν_μ CC interaction measured on April 22, 2014 is shown in 4.6. As NOvA detectors consist of alternating horizontal and vertical planes, event display shows hits from two types of planes in a separate windows. The top window displays X-Z hits position (detector activity as seen from the top), while the lower one displays Y-Z hits position (detector activity as seen from the side). The software allows to change a spatial zoom as well as a time zoom to see closely activity he/she might be interested in. Hits time distribution and deposited photoelectron charge distribution in ADC units together with event time stamp and trigger information are shown below the main windows. Hits also could be colored by their time, to see if they are close to readout window or not, or by their deposited charge, to see where the most of the energy was deposed. In the shown example, hits are colored by their charge.

Chapter 5

Simulation

In order to predict spectra at the near and the far detectors to compare predictions with actual data one needs to simulate neutrino interactions in the detectors relying on known physics models and theories of how particles are produced, how they travel and interact with detector material. The simulation process in NOvA starts with protons hitting the NuMI target and finishes with APD readouts and analog to digital converters. Side simulation packages or custom NOvA software are used in every step, output information on every step is used as input data for the following step

- Beam simulations: The FLUGG simulation package combines FLUKA [30] with GEANT4 [31]. Geometries of the target hall and detectors are encoded in GEANT4, and the proton interactions and downstream particle decays are simulated with FLUKA.

- Neutrino interactions: The neutrino flux generated in the previous step is input into the GENIE [32] package, which simulates neutrino-nucleus interactions inside the detectors. In each event GENIE produces a list of particles leaving the nucleus.

- Particle propagation: Particles produced by GENIE are propagated through the detector, and their interactions with the detector materials and decays are simulated by GEANT4. Amount of energy deposited in every cell is passed to the last step.

- Electronic signal: Deposited energy in the cell is converted to a light by the

scintillator; then light travels through the fiber to an APD and analog to digital converter. This step is simulated by NOvA custom software [33].

All of these parts are briefly discussed here.

5.1   Beam Simulation

The beam simulation estimates the neutrino flux into both detectors, and is accomplished using FLUKA and GEANT4 via the FLUGG interface. A detailed geometry of the target hall and target, the collimator, two focusing horns and the decay pipe is implemented in GEANT4, and the particle simulation is handled by FLUKA. The FLUKA package simulates 120 GeV protons which hit the graphite target, which yield hadronic showers of secondary particles that are directed by the horns into the decay pipe where they decay to neutrinos. All the proton interaction information whose daughter particles produce a neutrino is saved providing a way to study beam uncertainties related to particle production models.

The simulation outputs files which describe neutrino flux in terms of neutrino parent particles, flavour, energy and direction of motion.

5.2   Simulation of Neutrino Interactions

The neutrino interactions between ND and FD materials is simulated using GENIE. GENIE is developed by the experimental physics community, and is widely used as a neutrino Monte Carlo simulator for experiments due to its flexibility to simulate different target materials, and the accuracy of its results over a large range of neutrino energies which spans from MeV to PeV. As mentioned above GENIE gets a result of neutrino flux simulation from a previous step and convolutes it with neutrino interaction cross sections.

The neutrino energy spectrum expected in NOvA measurements overlaps with the energy regions of several neutrino interaction models, all of which are implemented in GENIE. These models include Quasi-Elastic scattering (QE), deep-inelastic scattering (DIS), baryon resonance production (RES) as well as meson exchange current (MEC) which dominates in 2 particle - 2 hole (2p-2h) effect. The physics behind the models is
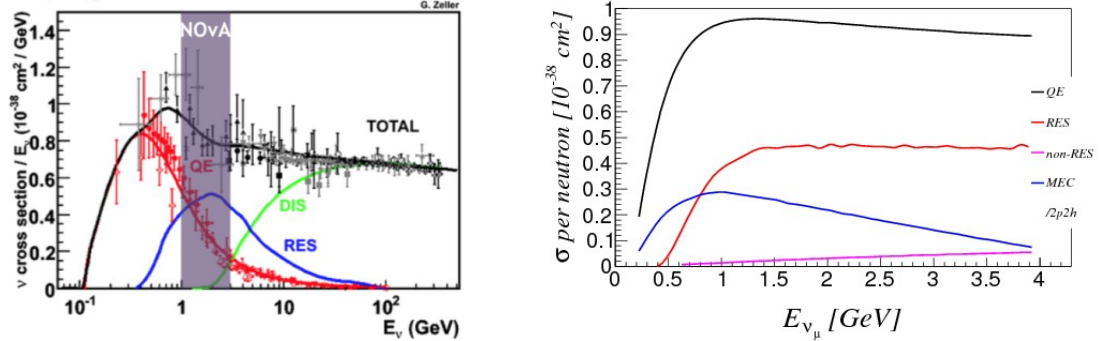
(a) Neutrino cross section energy dependence for QE, RES and DIS interactions overlapped with NOvA energy region used for the oscillation analysis.

(b) Neutrino cross section energy dependence used in GENIE neutrino generator.

Figure 5.1: Neutrino cross sections.

complicated, however on the qualitative level the QE interaction represents scattering off a single nucleon, the MEC interaction means scattering off a pair of nucleons, the RES process produces an excited nucleus, and the DIS interaction between a neutrino and a nucleus can disintegrate the nucleus[1].

Based on the left hand side of 5.1a, the typical energy regions of QE, RES and DIS neutrino interactions overlap with the NOvA energy domain. These three types of neutrino scattering are implemented in GENIE based on the Llewellyn-Smith model [34], Rein-Sehgal model [35] and effective leading order model with Bodek and Yang modifications [36] for QE, RES and DIS respectively. MEC process, which is included in GENIE as semi-empirical model, is described in [37].

5.3   Particles Propagation and Cerenkov Light

After GENIE is done with its part of simulation, or in other words, the list of particles which leave the nucleus with their energies, momenta and initial positions is ready, now one needs to propagate them through the detector material and simulate the energy deposition, interaction and decay. NOvA experiment uses GEANT4 [31] simulation

---

[1]This happens only when the energy transferred to a nucleus is sufficiently large

package for this step. Besides the list of particles, GEANT4 takes another input, namely geometry of the detector and its surrounding. Detailed information about blocks positions, cell structure and materials they made of, scintillator composition, concrete and steel support structure around the detectors is encoded in special geometry files.

The way GEANT4 propagates particles is done in the following manner. For each particle at each step of the trajectory it is decided with appropriate probability what particle should do next - move forward and deposit some energy, interact and scatter of particles that represent detector components, or decay. As a particle propagates further it loses its kinetic energy and as soon as particle's kinetic energy is less than 100 eV propagation stops. GEANT4 saves these trajectory steps as a list of particle positions, energy and momenta for the next step of simulation chain.

Before the final detector response could be simulated it is necessary to determine how much light was produced in the scintillator and what fraction of it was collected by the wave-shifting fiber and transported to the readout electronics. As a matter of fact, amount of light produced by the scintillator is not linearly proportional to amount of deposited energy due to a finite number of scintillator centres along the particle trajectory in the cell. The effect is know as Birks suppression [38]. If $\frac{dL}{dx}$ is light output per unit length and $\frac{dE}{dx}$ is amount of deposited energy then Birks law reads

$$\frac{dL}{dx} = L_0 \frac{\frac{dE}{dx}}{1 + k_B \frac{dE}{dx}}, \tag{5.1}$$

where L_0 and k_B are constants which depend on scintillator. Parameter k_B is tuned using muon and protons tracks in the Near Detector.

Another phenomena which plays a significant role in light production is Cerenkov effect [39]. This effect was observed in a bottle of water subjected to radioactive bombardment. Charged particle while moving through the liquid with velocity greater than the phase velocity of light emits light and this emission is simulated in NOvA experiment. The following formula is used to predict the number of Cerenkov photons produced per distance traveled at a given wavelength

$$\frac{dN_\gamma}{dx d\lambda} = \frac{2\pi\alpha z^2}{\lambda^2} \left(1 - \frac{1}{\beta^2 n^2(\lambda)}\right), \tag{5.2}$$

where α is fine-structure constant, z is charge of moving particle in units of e, $n(\lambda)$ is refraction index and β is particle's velocity in units of c.

5.4 Light propagation and signal to store

The last simulation step is done using custom NOvA software that is split into two parts - light propagation to the readout electronics, and the signal measurement made by the electronics. Although in practice cells could be different from each other (horizontal cells are not exactly horizontal because of their length - cells could be slightly bent, especially in the far detector. Not exact horizontality also leads to small bubbles of air are being trapped inside the cells) in simulations it is assumed that all cells are identical.

5.4.1 Light propagation

Assuming all cells are equivalent, a ray-tracing model is used to estimate how many photons were trapped by each WLS fiber. The following characteristics of detector components were measured in bench experiments, and used in light propagation simulations:

- characteristic scintillator emission time - 9 ns

- scintillator index of refraction - 1.46

- reflectivity of the cell walls - 87.7%

- photon capture length[2] - 30.66 cm

The resulting template is shown on 5.2. This template is used to determine the number of photons trapped in WLS fiber. To simulate what fraction of photons reaches the APD half of photons are sent in opposite directions around the fiber. There are some fraction on photons which is absorbed or get out of fiber, and the effect is accounted for in simulation by using attenuation curve which was measured in bench tests. Before the last simulation step starts, the number of photoelectrons created in each APD is determined by taking into account APD's quantum efficiency and additional Poisson smearing.

---

[2]Probability to capture a photon $P \sim e^{x/L}$, where x is distance between the point where the photon
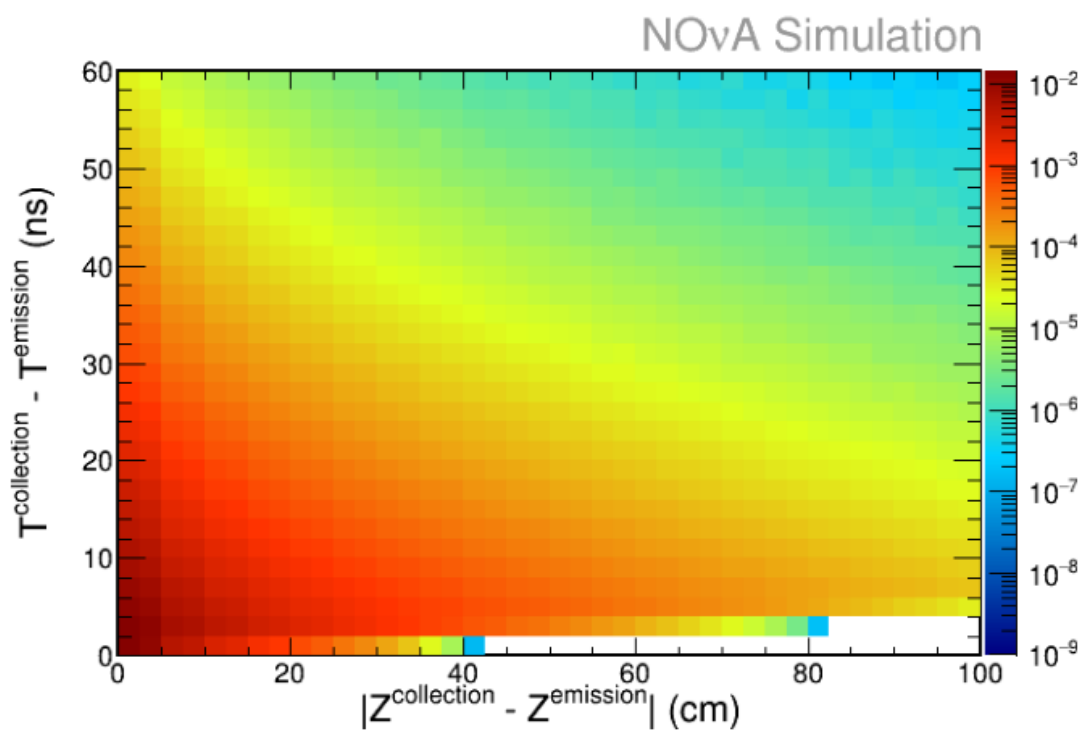
Figure 5.2: The collection rate of scintillator photons by a wavelength shifting fiber loop relative to the position and time where and when the energy was deposited.

5.4.2 Electronics

Photo-electron signal in the APD created in the previous step have to be digitized to finalize the simulation of the cell hit. As an APD impulse is too short, first it is stretched in the Application Specific Integrated Circuit (ASIC) by the CR-RC circuit. The response of the ASIC to a charged impulse has the following form

$$f(t) \sim e^{-\frac{t-t_0}{F}} - e^{-\frac{t-t_0}{R}}, \qquad (5.3)$$

Figure 5.4: Schematics of digitization

where t_0 is the time when pulse was created by APD, F and R are the fall time and rise time of the CR-RC circuit. And as was mention in chapter 4 the signal value is split into 4096 possible values and only 4 last ADCs - value of the digitization sample - is stored when the difference $ADC_i - ADC_{i-3}$ is greater then a threshold. At this point the simulation files have the same structure[3] as the data files. The next step in NOvA analysis is to reconstruct high level information about recorded or simulated events with the help of reconstruction algorithms which are the same for the real data and simulation.

---

was produced and the fiber, L is capture length.

[3]Of course plus additional information about type of neutrino information, resulting particles' momenta and energies etc.
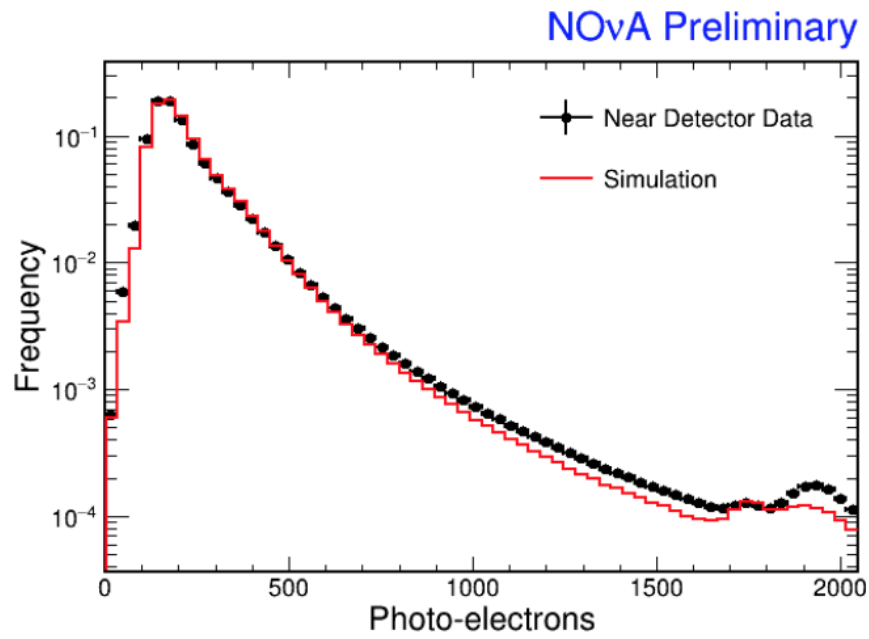
(a) Near Detector
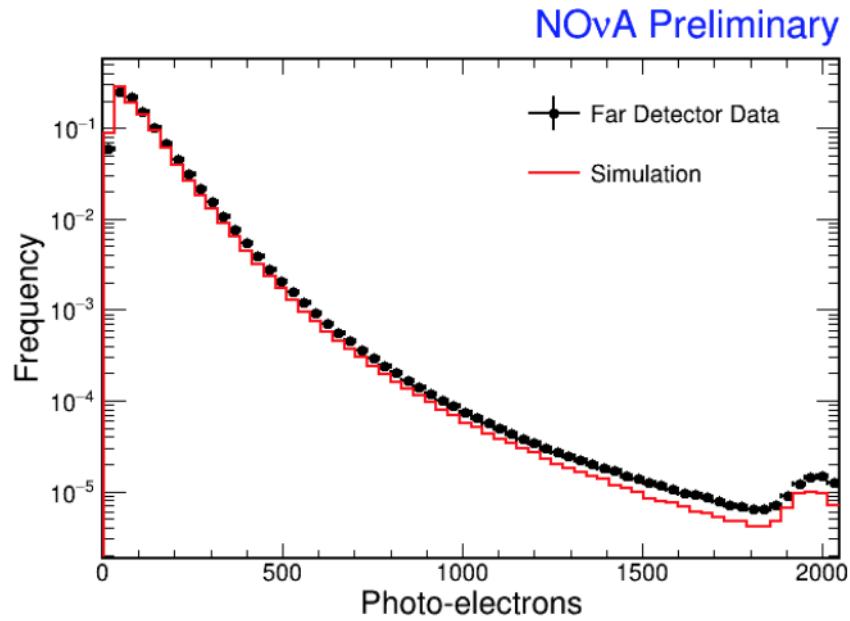
(b) Far Detector

Figure 5.3: Attenuation curves for the near and the far detectors. Data points are detectors response to cosmic ray muons while simulation curves are results of bench experiments.

Chapter 6

Event Reconstruction

To measure θ_{23} and Δm^2_{32}, neutrino-nucleon interaction events must be identified, and the resulting lepton and hadron energies and trajectories must be measured. To do this, data from the detectors is reconstructed into particles, and ν_μ CC interactions are identified. The reconstruction process chain is summarized as follows:

- Slicing. The full $550\mu s$ readout window contains hits which are associated with neutrino interaction, cosmic rays activity and noise. The hits need to be separated into different groups which ideally correspond to different physical processes.

- Tracking. Each slice is processed by a tracking algorithm to determine the 3-dimensional particle trajectories.

- Calibration. Each channel in every slice is calibrated to convert the magnitude of each measured signal into a channel energy.

- Muon identification and background rejection. Slices that contain a muon track are identified as pertinent to the ν_μ CC interaction.

- Energy estimation. Templates are used to map muon track length to true muon energy and visible hadronic energy[1] to true hadronic energy in order to determine neutrino total energy.

---

[1] Total energy of all hits in the slice which do not belong muon track

The analysis done here is based on two different data samples - contained and uncontained muons - that were selected and processed by different reconstruction algorithms. Muon identification and energy estimation algorithms used in the contained sample are explained here, and algorithms used in the uncontained sample are explained later.

6.1   Slicing

As can be seen on the figure 6.1 data recorded for one NuMI spill contains multiple uncorrelated activities. Even though the length of NuMI spill is $12\mu s$ in the middle of $550\mu s$ readout window, the slicer algorithm is applied to all the hits in the window to protect against small possible drift of NuMI spills as well as to make slices for cosmic rays for background estimation.

The task of the slicer is to group hits, which casually related to each other, in slices. The slicer is based on the DBSCAN algorithm [40], one of the most common clustering algorithms, and checks every pair of hits to determine how far are they from each other in space and time. The distance function is not exactly a space-time interval but rather modified

$$d = \Big(\frac{\Delta t - \frac{\Delta r}{c}}{T_{res}}\Big)^2 + \Big(\frac{\Delta z}{D_z}\Big) + \Big(\frac{\Delta v}{D_v}\Big), \tag{6.1}$$

where c is the speed of light, Δt and Δr are time and space difference between two hits respectively, T_{res} is the timing resolution, Δz is the distance between the hits along the z direction, Δv is the distance between hits in x or y direction. As soon as the function returns a value which is lower than a predefined threshold, two hits are put together in one slice. The first term prefers hits which lie close to a light cone, in other words it is assumed that all the particles move with the speed of light[2]. The second and the third terms penalize hits which are far from each other in space. These terms help to remove noise hits as they are randomly distributed in space and time, and therefore, they could be far from the main activity. After all correlated activities have been accounting for, and slices are created, the remaining hits are put into one additional noise slice.

The NOvA slicing algorithm efficiently separates different neutrino activities in the

---

[2]Or energy of the particles is much large than their masses.
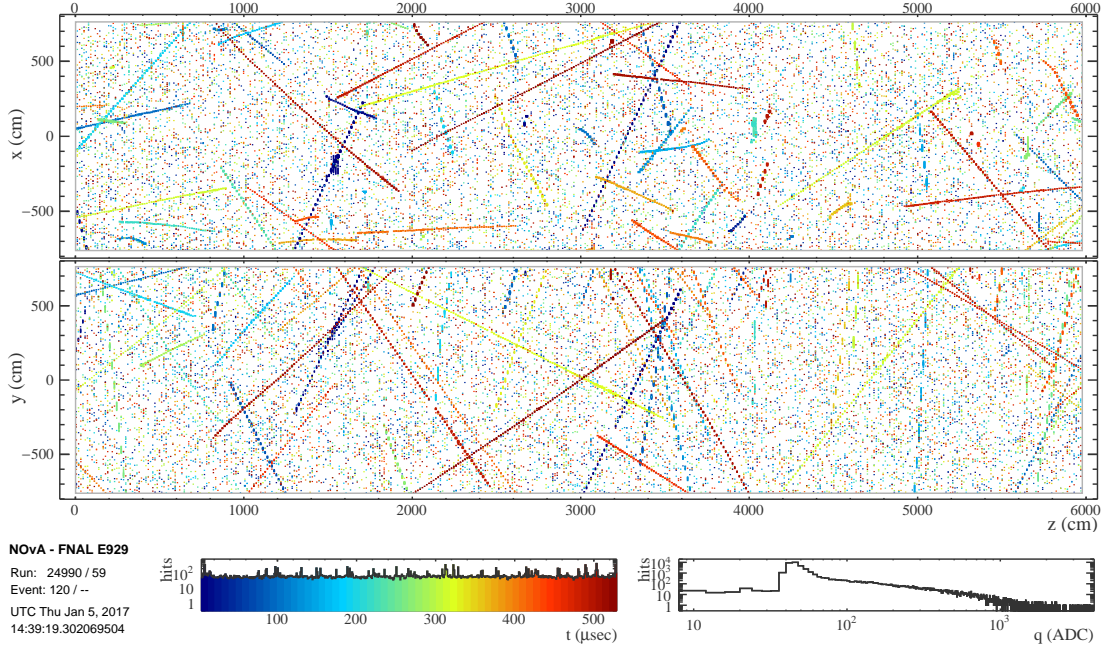
Figure 6.1: Trigger window in the far detector data. Hits are colored by the time they were recorded.

near detector and distinguishes cosmic rays from neutrino interactions in the far detector. However, hits which were produced by Michel electrons[3] or photons follow neutrons capture are usually not included in the corresponding slice.

6.2 Tracking

As all the activities are separated into corresponding slices the next step in the reconstruction chain is to find the sets of hits which are attributed to the different particles produced in the neutrino interaction or cosmic activity. Cosmic ray activity is usually consistent with only one particle, while neutrino interaction measurements are usually consistent with multiple particles.

The NOvA tracking algorithm is based on Kalman filtering [41] and its implementation could be found in [42]. In short, the algorithm is run on two views (X and Y)

---

[3]Electron produced in muon decay often called after Louis Michele who contributed significantly to the physics of charged leptons decay.

separately and merges 2D tracks into 3D ones. To construct a 2D track two hits with separation smaller than three planes are chosen as track seeds at the most downstream location[4]. The algorithm combines hits as it works upstream and the added hits are fit with piecewise linear segments. Adding a hit or not is decided on the basis of how much the χ^2 is changed by the hit; if it less than eight units then the hit is added. Fitting the track with linear segments naturally helps to follow particles trajectory with multiple scatterings. A track is considered to be reconstructed if the algorithm travels more than 3 planes and no hits are added, and the algorithm is run repetitively until no more tracks are reconstructed. The majority of the particles produced by neutrino interactions travel downstream, and thus the longest track, often the muon, is reconstructed first.

After all 2D tracks are found in both views they need to be merged into 3D tracks. Tracks are merged based on a geometric algorithm that considers the degree of overlap of disparate tracks, and the distances between their start and end points. For each track in X view with Z coordinates (z_{x1}, z_{x2}) and each track in Y view with Z coordinates (z_{y1}, z_{y2}) a score is calculated

$$\text{score} = \frac{|z_{x1} - z_{y1}| + |z_{x2} - z_{y2}|}{\min(z_{x2}, z_{y2}) - \max(z_{x1}, z_{y1})}. \tag{6.2}$$

The pair of 2D tracks with the lowest score are merged into one 3D track, and identified as one particle. The merging process continues until there are no 2D tracks to merge, unmatched 2D tracks are also recorded for possible analysis later.

6.3   Calibration

To convert cell hit arbitrary electronic units (ADC) into meaningful energy units (GeV) a calibration process should be carried out. Calibration consists of two parts - attenuation and absolute energy calibration. Both parts would be briefly explained in this section.

---

[4]Downstream in the sense of the incoming neutrino from Fermilab

6.3.1 Attenuation correction

After an ADC signal is produced it has to be decided by what factor the signal should be multiplied since a hit at the far end of the cell will result in a smaller signal as compared to a signal from a hit in the middle. For obvious reasons, hits produced by a beam neutrino are not appropriate as a source for the calibration. However, the abundance of cosmic rays with well understood properties helps with the procedure. Among all reconstructed cosmic tracks those are chosen which start and end on detector edges, this criterion is needed to make sure that tracks are not stopped inside the detector. An additional requirement is the that tracks should cross more than ten planes, thus allowing an accurate estimation of muon path in every cell it crosses. Finally, only those hits on tracks are used for calibration which satisfy a tri-cell criterion - a hit for calibration should have both adjacent cells to be hit, see figure 6.2. This conditions lead to a good estimation of muon trajectory and hence path length within each cell.

The ADC signal is scaled to a photoelectric (PE) value - estimation for minimal value of electronic signal based on 4 recorded ADCs, see chapter 5 for more details. After that for each reference hit, the path length and position within the cell (W) is estimated and a 2D histogram - ratio of PE and path length versus position within the cell - is made. A mean ratio of PE and path length as function of W is fit by the sum of two exponents which represent signal trip in two direction along the wave length shifting fiber.

$$y(W) = C + A\left(e^{\frac{W}{X}} + e^{-\frac{L+W}{X}}\right),\tag{6.3}$$

where A and C are fit parameters, X is the fiber attenuation length and L is length of the fiber. For information about additional effects close to cell ends see [43]. Figure 6.3 shows examples of the fit for far and near detectors.

For analysis, the W of every hit is estimated and a PE value of the hit is divided by fit at this position to get a corrected PE value of the hit. Since the attenuation curve is determined from the cell response to cosmic ray muons, the corrected PE value of the hit shows the relative signal to the cosmic muons. At this point, the attenuation is taken into account but the units of corrected PE signal are still arbitrary and the absolute energy calibration is still needed.
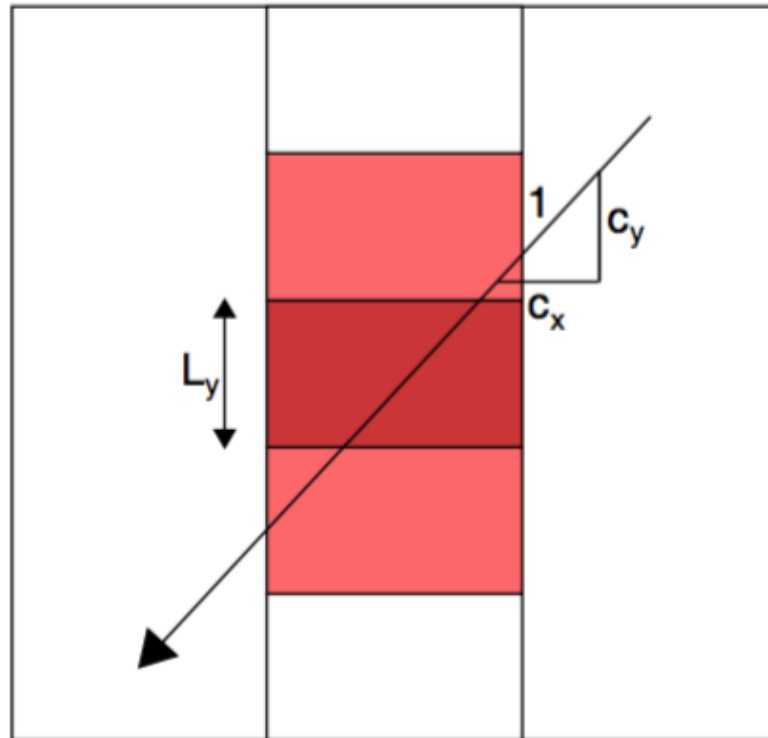
Figure 6.2: Tri-cell criterion.
The cell hit is used in calibration only if adjacent cells in the same view are also hit.

6.3.2 Absolute energy calibration

As in the previous step cosmic muons are used at this step too, but now hits a fixed distance from the end of the cosmic muon tracks are used. Thus, tracks which are used for calibration should stop inside the detector. The reason for using tracks end is that according to Bethe-Bloch formula [1] muon energy deposition per unit length ($\frac{dE}{dx}$) has a well understood minimum near the track end. The minimum deposition is typically span several meters from the end of the track for different materials and the region from 1 meter to 2 meters from the end of the track is used in NOvA absolute energy calibration procedure. Figure 6.4 illustrates the calibrated muon $\frac{dE}{dx}$ as a function of
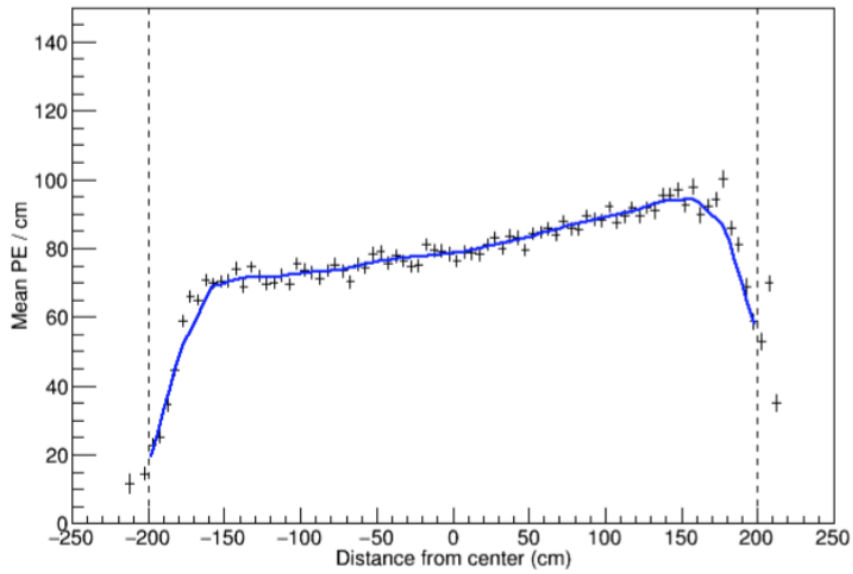
(a) Near Detector
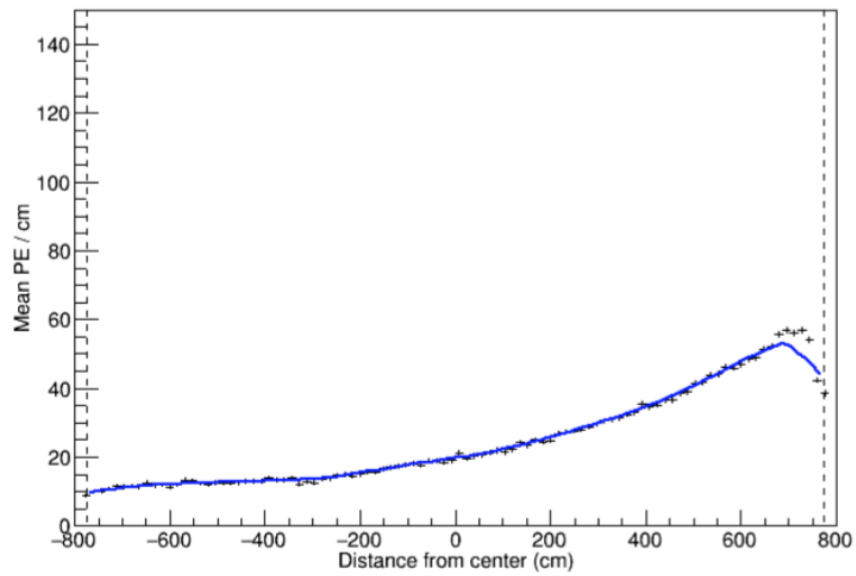
(b) Far Detector

Figure 6.3: Attenuation fits
Examples of attenuation fits in Near (top) and Far (bottom) detectors.
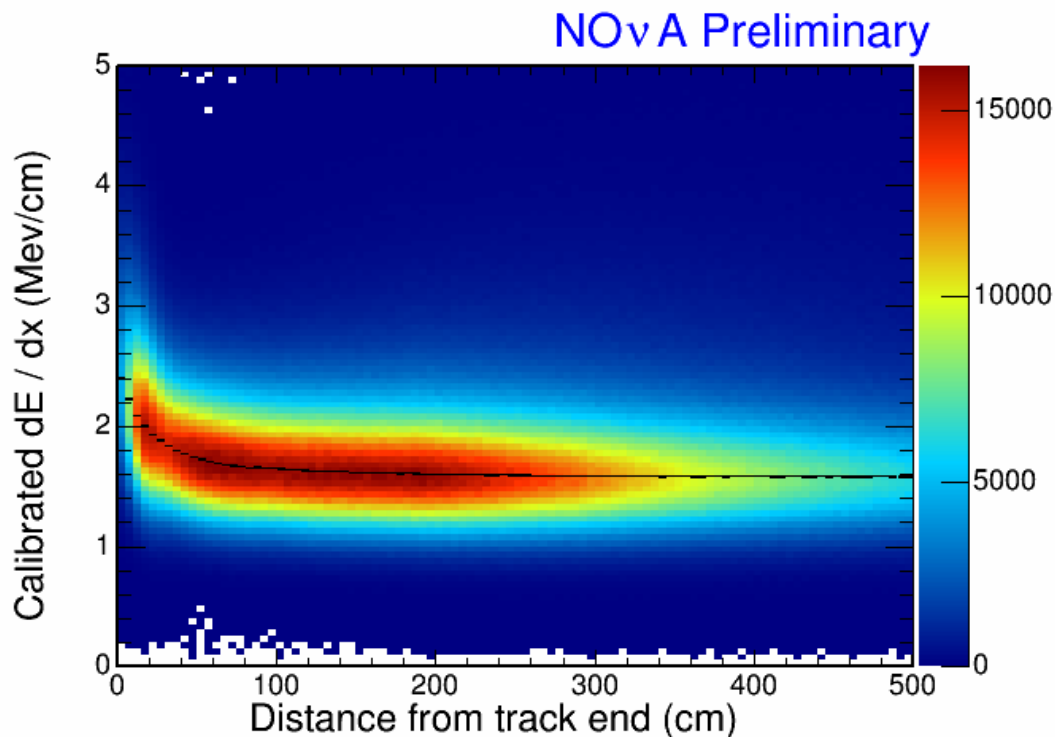
Figure 6.4: Muon $\frac{dE}{dx}$ per unit length in NOvA.
Already calibrated $\frac{dE}{dx}$ is shown as a function of distance to the end of the track.

distance from track end measured in NOvA.

6.4   Muon Identification

The neutrino disappearance analysis relies heavily on correct identification of the muon among the byproducts of the neutrino interaction with detector material. Existence of the muon in the event suggests that ν_μ CC interaction happened and the event is passed downstream for further analysis. Currently, NOvA uses two different algorithms to identify muons: the k-Nearest Neighbor (kNN) clustering algorithm, and a convolutional neural network. Extensive analysis has shown that using both algorithms gives better results than either of them individually.

6.4.1 ReMID

The Reconstructed Muon Identification (ReMID) algorithm uses four characteristics of a each reconstructed track to identify muons. kNN stores training examples in the 4-dimensional (number of dimensions is equal to number of features extracted from the track) space with additional label specifying the class examples belong to a muon or non-muon. These training examples were taken from NOvA simulation. Four features from the test track are represent a point in this 4-dimensional space and in order to determine the probability the point corresponds to a muon track kNN finds its k nearest neighbors[5] and calculates the fraction of muon neighbors. This fraction is output of kNN algorithm. Number k is adjustable hyper parameter and was chosen to be equal 80 in NOvA.

Four features which extracted from the track are track length, $\frac{dE}{dx}$ and scattering log-likelihood for muon hypothesis and non-hadronic plane fraction. $\frac{dE}{dx}$ and scattering log-likelihood are determined with the help of probability distributions that shows particle probability to deposit some energy and scatter by some angle at some distance from the end of the track, and these distributions are derived from simulation, for more information see chapter 6 of [42]. The last feature is a ratio of number of planes in the track which are free of hadronic shower contamination and total number of planes in the track.

6.4.2 CVN

Convolutional Visual Networks (CVNs) are neutral networks that excel in image classification, and are used in NOvA to identify muons. The full implementation of the CVN is described in [44], and the key points are described here.

In its core, CVN is a regular neural network but with tens of hidden layers and tens of millions of weights. On the higher level though, CVN learns features itself and a human is no longer required for this work. An input to CVN is two pictures 100 by 80 pixels around neutrino activity in X and Y views. Similar to ReMID, labels for the training pictures are taken from the simulation. However, the biggest difference is that while ReMID checks one track at a time and does the muon/non-muon classification for

---

[5]Regular L^2 metric in R^4 is used; $||\vec{r_1} - \vec{r_2}||^2 = (x_1 - x_2)^2 + (y_1 - y_2)^2 + (z_1 - z_2)^2 + (w_1 - w_2)^2$

track, CVN analyzes the whole activity in the slice and does the classification in multiple classes - muon/electron/tau neutrino, QE/RES/DIS/MEC interaction, NC interaction and cosmic rays.

A deep convolutional neural network requires tremendous amount of training samples to prevent an overfitting together with regularization techniques such as dropout layers [45] and weight decay. In order to increase available training dataset some pictures are randomly changed. First, Gaussian noise is added to all pixels with a standard deviation of 1%, this also reduces reliance on the simulated intensity in each pixel. Then, some pictures are reflected in the direction perpendicular to neutrino beam. An example of pictures that are fed into CVN are shown in Figure 6.5.

As stated above, CVN classifies events in multiple classes i.e. CVN output is n-dimensional vector with sum all its components equal to one. These components could be interpreted as probabilities that the current event belongs to a particular class. Only muon neutrinos are used in the current analysis, thus to select an event sum of outputs in muon/QE, muon/RES, muon/DIS and muon/MEC classes should be bigger than some threshold.

6.5 Energy Estimation

The final step in the reconstruction chain is estimating the total neutrino energy. The probability that one flavor of neutrino with a given energy will oscillate to other flavors depends on its energy, thus more precise measurements of energy would yield better measurements of θ_{23} and Δm^2_{32}. A simple approach like summing all of the calibrated energy and additional accounting for dead material[6] is not as good as the following one. In NOvA, energy estimation process is divided into two similar parts; energy estimation of the most muon like track and the rest of the activity, since muon part of the event is well understood while the hadronic part is not so well.

$$E_\nu = E_\mu + E_{had}. \tag{6.4}$$

---

[6]Dead material consists of any detector parts which are not producing light i.e., plastic, air bubble, glue and possible gaps between planes.

The muon energy, E_μ, is estimated using a 2D histogram that shows the true muon energy versus track length. This histogram was populated using muons produced in simulated neutrino interactions that were reconstructed with a ReMID output above zero, and a CVN output above 0.6 [46]. The fit is a piecewise linear spline with multiple segments; an example of this function is shown in Figure 6.6.

The second term in eq 6.4 is the hadronic energy, and is estimated differently. Calibrated energy of all hits which are not on muon track is summed together with additional hadronic energy which overlaps with muon track. The algorithm that determines how much energy overlaps with muon track is described in [47]. The hadronic energy is challenging to model correctly, so instead of true hadronic energy the fit uses true neutrino energy minus reconstructed muon energy. This approach accounts for dead material automatically. Similar to muon case, the fit is piecewise linear spline with up to four segments, as shown in figure 6.7. The optimization is done to minimize the total neutrino energy resolution rather then resolution of muon and hadronic energies separately.

The detectors operating conditions change with time, so to improve the analysis different energy estimators were used during different data taking periods.
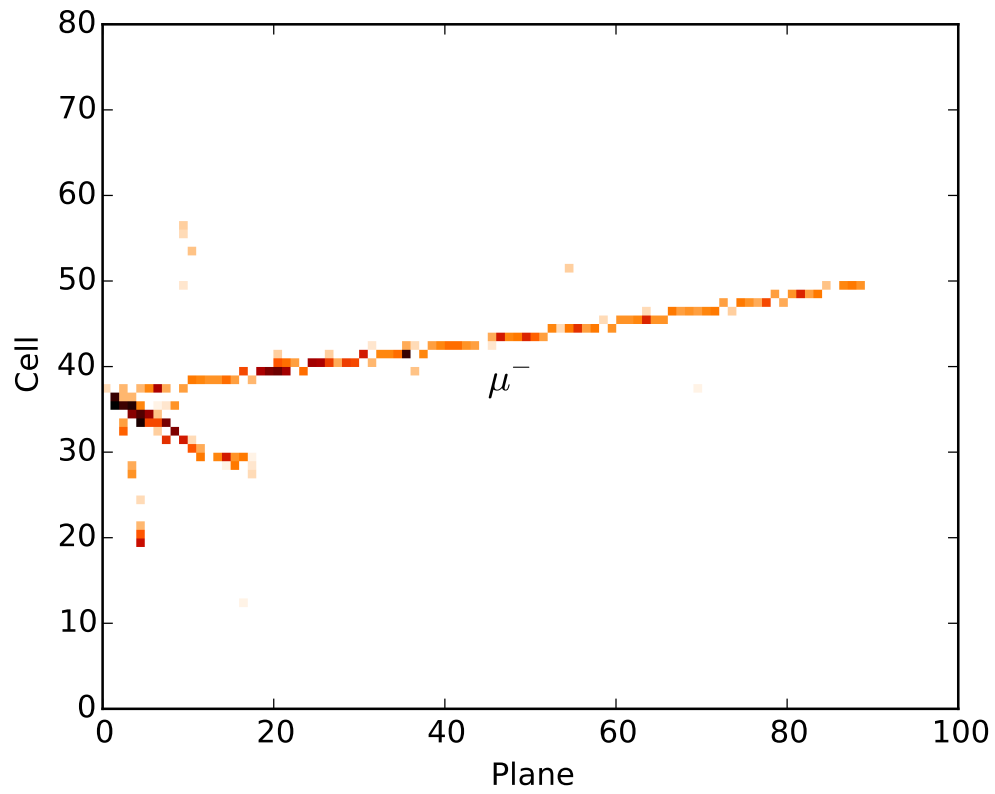
Figure 6.5: CVN Pixel Map.
Example of the figure which is fed into convolutional neural net for training. The window of 100×80 pixels is chosen around the true ν_μ CC interaction activity in a such way that reconstructed vertex is approximately put in the left middle part of the picture.
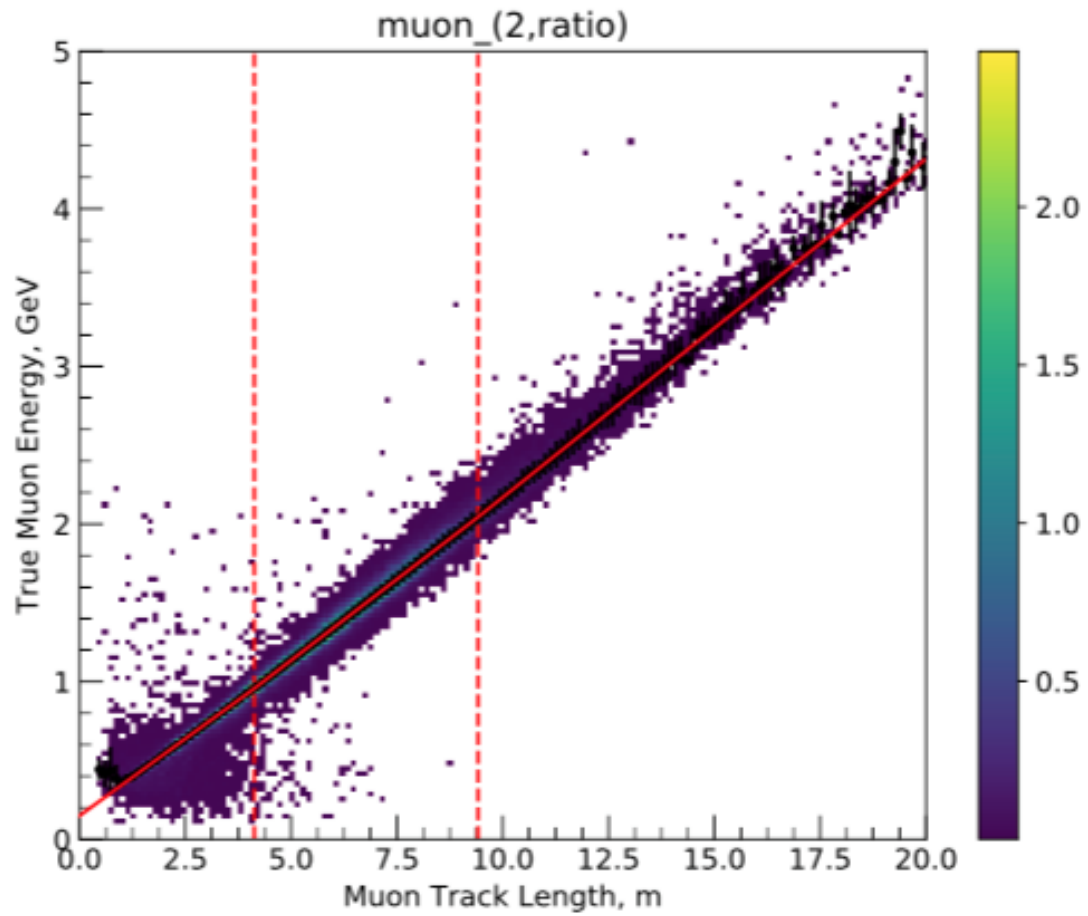
Figure 6.6: Muon Energy Estimator.
Muon track energy is measured based on muon track length. The fit is a piecewise linear spline, vertical dashed lines represent joint points and red line is a fit. Stitches, offsets and slopes are free parameters of the fit.
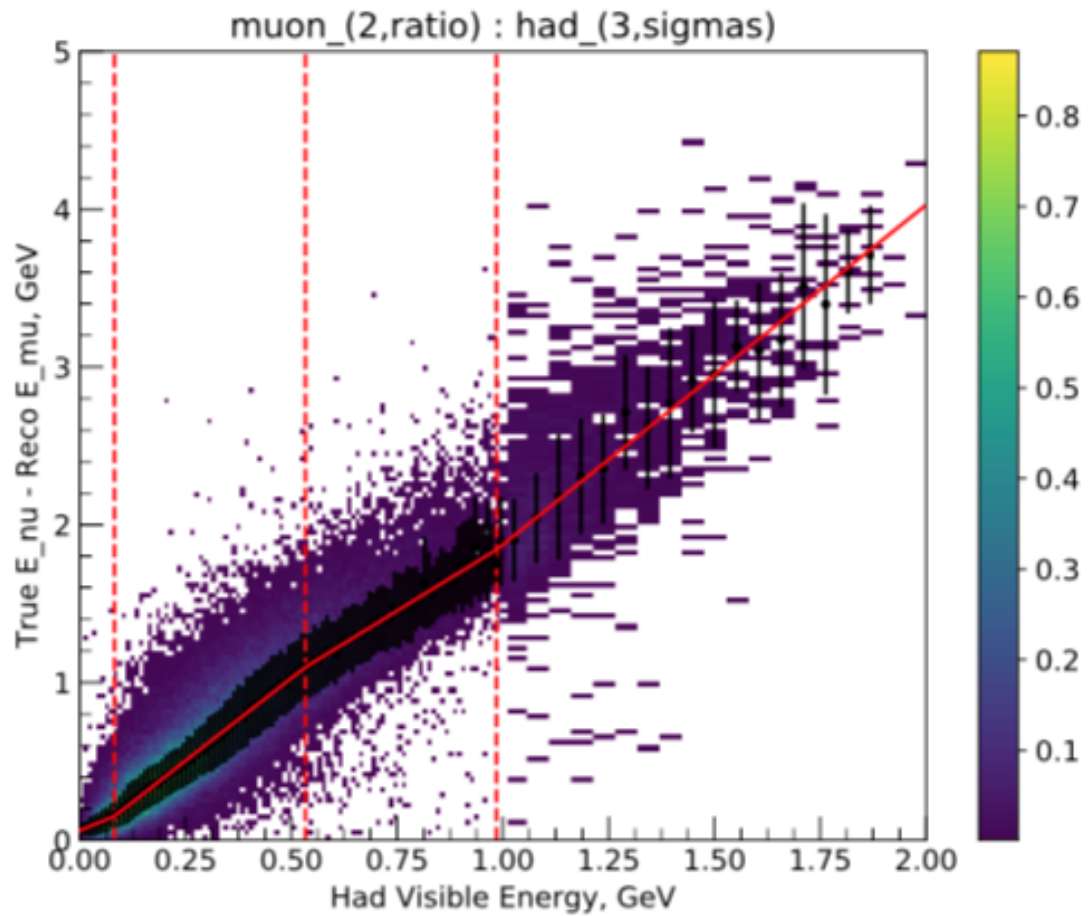
Figure 6.7: Hadronic Energy Estimator.
Hadronic energy measured based on visible calibrated energy. The fit is a piecewise linear spline, vertical dashed lines represent joint points and red line is a fit. Stitches, offsets and slopes are free parameters of the fit.

Chapter 7

Contained and Escaped ν_μ CC Event Selection

In this chapter, algorithms for the event selection are described. The chapter begins by describing the contained sample and the event selection criteria. These criteria were developed by other members of the NOvA collaboration, and are summarized in section 7.1. This is followed by a description of the new selection criteria used to select the "escaping sample" - events that failed the contained event selection criteria, but had evidence of a muon neutrino interaction. The final selection criteria for escaping events maximizes sensitivity to θ_{23} and Δm_{32}^2. By combining the contained and escaping samples of events, better measurements of θ_{23} and Δm_{32}^2 are made.

7.1 Contained Sample

The selection criteria used to select contained sample events ensure that selected events contain a ν_μ CC interaction, the muon energy is measured with good resolution, and cosmic contamination is low. These selection criteria are described in the subsequent sections.

7.1.1 Data Quality

A data quality is the first cut in contained sample selection flow and serves to remove events of poor quality. Events which pass data quality cut have

- more than 20 reconstructed hits. There is no useful information for events with fewer number of hits.

- at least one track reconstructed by cosmic tracker. This criterion confirms that there is cluster of hits which could be associated with track.

- PID value of ReMId selector should be greater than zero. This ensures that at least one 3D Kalman track was reconstructed.

- slice which spans more than 4 consecutive planes. This cut removes events with geometric gaps and highly vertical tracks, thus the cut is a good preselector for a good fraction of cosmic rays.

7.1.2 Containment

The containment requirement selects events where the majority of the activity is measured in the central region of the detector. This further reduces contamination from cosmic ray events, as most cosmic rays enter from the tops or sides. Contained events have the best energy resolution and satisfy criteria below, which are explained in the next paragraph,

- Kalman Forward Cell > 6,

- Kalman Backward Cell > 6,

- Cosmic Forward Cell > 0,

- Cosmic Backward Cell > 7,

- Planes to Front > 1,

- Planes to Back > 1,

- Minimal Prong Distance to FD Top > 60,

- Minimal Prong Distance to FD Bottom > 12,

- Minimal Prong Distance to FD East > 16,

- Minimal Prong Distance to FD West > 12,

- Minimal Prong Distance to FD Front > 18,

- Minimal Prong Distance to FD Back > 18.

The first four criteria use tracks reconstructed by the Kalman Tracker and Cosmic Tracker. For every track, the number of projected cells[1] from start/end of the track to the edge of the detector is estimated and these numbers should be bigger than above stated thresholds. The next two criteria checks that reconstructed slice does not have hits in the first and the last planes of detector active region[2]. Finally, the last six criteria use objects reconstructed by Fuzzy clustering algorithm, the objects consist of hits that could belong to different clusters (in other words, two particle which move in close trajectories could contribute to one hit). The thresholds in the last six criteria are result of optimization carried out in [48].

7.1.3 ν_μ CC selection

This cut aims to select ν_μ CC like events and to reject ν_e CC and ν NC like events. The optimization of the selection thresholds is discussed in detail in [49], and the thresholds are

- ReMId > 0.5 - event has long muon track with a good ReMId score,

- CVN > 0.5 - event has a good score for ν_μ CC classifier based on convolutional neural net.

7.1.4 Cosmic Rejection

The final selection criterion in the contained selection further reduces cosmic ray contamination. Several event variables are analyzed using a Boosted Decision Tree (BDT) algorithm[3][50], and the BDT output is used to discriminate between cosmic and ν_μ CC

---

[1]along the track

[2]Data were taken during detector construction period, thus active region was changing with time.

[3]Discussed further in the next chapter.

events. These event variables used in the BDT are

- cosine of angle between muon track and incoming beam direction,

- reconstructed y-direction of the muon track,

- reconstructed length of the muon track,

- largest y-position of either the start or the end of muon the track,

- CVN cosmic score,

- min(CosmicForwardCell + CosmicBackwardCell, KalmanForwardCell + Kalman-BackwardCell), this variable helps to discriminate through going cosmic muons which passed all previous cuts,

- ratio of hit number in kalman track to hit number in slice, this ratio is a measure of hadronic energy fraction. Cosmic events have very little hadronic energy as compared to beam neutrino events.

The BDT outputs a PID value, and events are selected if their PID value is > 0.5 [49].

7.1.5 Resolution Bins

Previous analyses carried out in [47], [51], [52] used one selected sample for fitting to actual data. Analysis carried out in [42] used several samples for fitting to data such as a contained QE sample, a contained non-QE sample and an escaping sample[4]. This approach separates events into different energy resolution bins and thereby improves the final sensitivity of the experiment. Finally, the recent analysis [53] goes further and separates contained sample into four independent samples with different fraction of hadronic energy in selected events.

Hadronic energy fraction ($\frac{E_{had}}{E_\nu}$) distribution is made for every reconstructed neutrino energy bin and is split into four parts - lowest, second to lowest, second to highest and highest quantiles - so every quantile has equal number of events. A Plot of $\frac{E_{had}}{E_\nu}$ vs E_ν and quantile boundaries are shown in figure 7.1. Since the detector configuration was

---

[4]Most of the events selected in the escaping sample in [42] have energy far from the first oscillation dip, thus it is not contributing much to the disappearance analysis. Current analysis aims to address this issue.

different for different run periods, the analysis uses different quantiles boundaries to account for that.
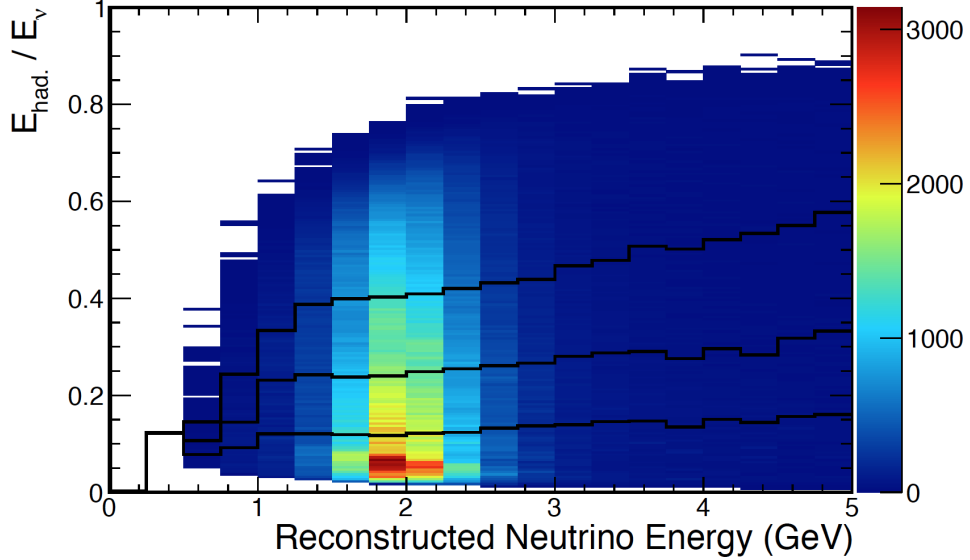
Figure 7.1: Hadronic energy fraction quantiles.
Hadronic energy fraction vs reconstructed neutrino energy plot allows to determine for every bin of reconstructed energy hadronic energy fraction quantile. Events from every bin are split into 4 parts and separated by black horizontal lines. This plot is made for run period 2, plots for other run periods are similar.

7.2 Escaping Sample

The remainder of the chapter describes the new work done to select ν_μ CC events where part of a muon track was measured. The main goal is to select the sample with minimal cosmic background and maximal beam neutrino signal.

7.2.1 Definition and Basic Selection

Escaping sample does not have the nice qualities of the contained sample such as low cosmic background and high energy resolution; nevertheless, it might provide additional information on neutrino oscillation effectively increasing gathered statistics.

Events which define the escaping sample do not need to be only particles which leave the detector but rather ones which fail to pass some cuts of contained sample. The obvious cut escaping events should fail is containment cut 7.1.2. Escaping events also should pass some cuts from contained sample because it is still needed that they contain useful information for the analysis. Those cuts are

- data quality cut - events have reasonable number of reconstructed hits and tracks,

- CVN > 0.5 - events are highly ν_μ CC events,

- loose cosmic rejection, cosmic rejection PID value is > 0.48 - events should not be an obvious cosmic rays.

These are the basic criteria for the escaping sample. In Figure 7.2, the expected number of cosmic and signal events which pass basic criteria for primary track length distribution is shown.
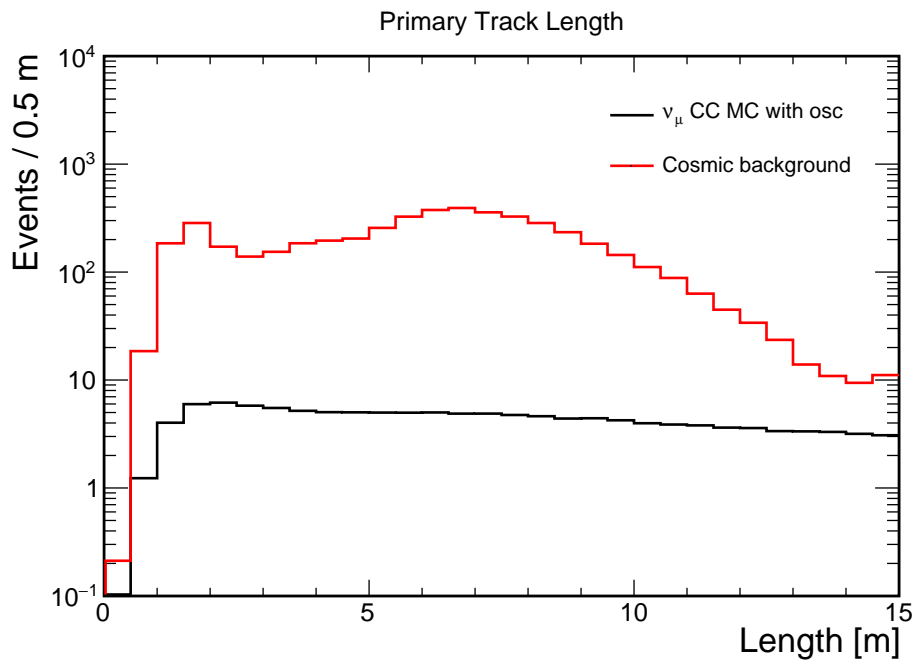
Figure 7.2: Length of Primary Track After Base Cuts.
The plot illustrates almost two order of magnitude difference between expected number of signal events (black) and cosmic events (red).

7.2.2 Preselection

The next step is to understand what variables could help to discriminate cosmic rays and beam neutrino signal. The first approach here is to try to determine direction of the primary track - is track going out of or in the detector? Unfortunately, the time resolution of individual hits is not enough to determine confidently the direction of the track and other approaches are needed.
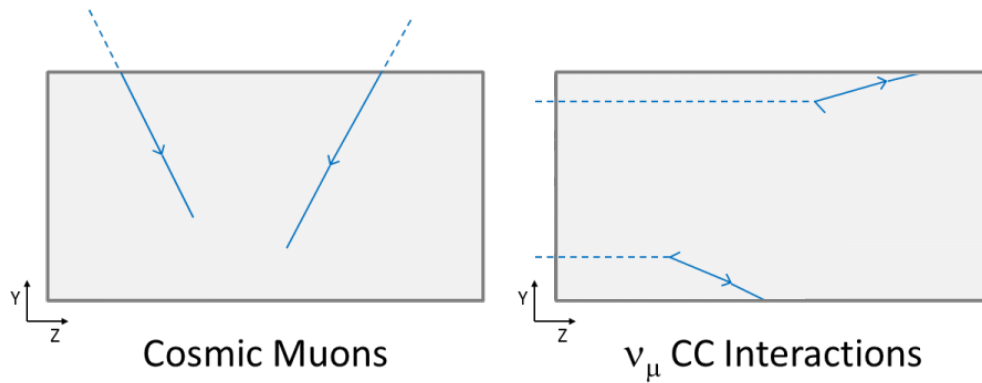
(a) Topologies.
Dash lines illustrates parts which are not visible in the detector.
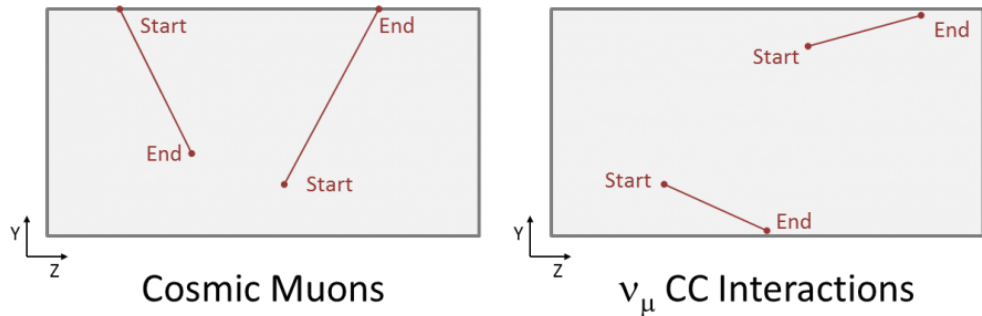
(b) Reconstructed Kalman tracks.

Figure 7.3: Cosmic rays and beam neutrinos in the far detector.

Figure 7.3a shows topologies of cosmic
rays and beam neutrinos with escaping
muons, and Figure 7.3b illustrates cor-
responding reconstructed Kalman tracks.
The feature of the Kalman tracker is that
it all reconstructed tracks are assumed to
point along the positive Z-axis, and this
substantially reduces cosmic ray contam-
ination at the cost of a small reduction in

Figure 7.4: Backwards projected distance
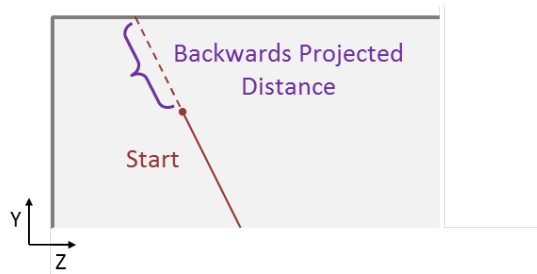
the signal. All cosmic rays effectively are divided into two populations, the one where
track direction assumed correctly and the one where it is not. These populations are
clearly seen on the figure 7.5 where the distribution of reconstructed Kalman track Y-
direction at its end (StopDirY) is shown for the cosmic rays and the primary track of
the signal events. The usage of this variable will be explained later. Now, one can see
that it is easy to remove one population by requiring backwards projected distance 7.4
(KalBakCell) to be greater than some threshold. The actual cut is perform for 'number
of backwards projected cells' variable, see figure 7.6.

The next selection criterion is not designed to further decrease amount of cosmic rays
but rather make selected sample to be more clean for energy estimation. Next chapter
is completely devoted to this topic. Each hadronic cluster (all hits in slice except the
ones which belong to primary track) cannot have a hit which is within 2 cells of the
edge of the detector. Figure 7.7 shows the distribution of StopDirY after this cut and
the previous one (KalBakCell > 7).

There is another variable which removes big a fraction of cosmic rays similar to
KalBakCell. And this variable is StopDirY. As can be seen from figure 7.3b, all cosmic
rays, which have incorrectly reconstructed direction, have their StopDirY grater than
zero. By asking that variable to be less than zero for escaping sample the second
population of cosmic rays could be eliminated. Physically, that means that only those
events are selected whose primary track stops or leaves the detector pointing downward.
This cut has a big impact on the signal as incoming beam neutrinos pointing upward
at a few degrees level, thus muons resulting in ν_μ CC interaction also prefer upward
direction. Track direction at its end is more useful variable as compared to track's start
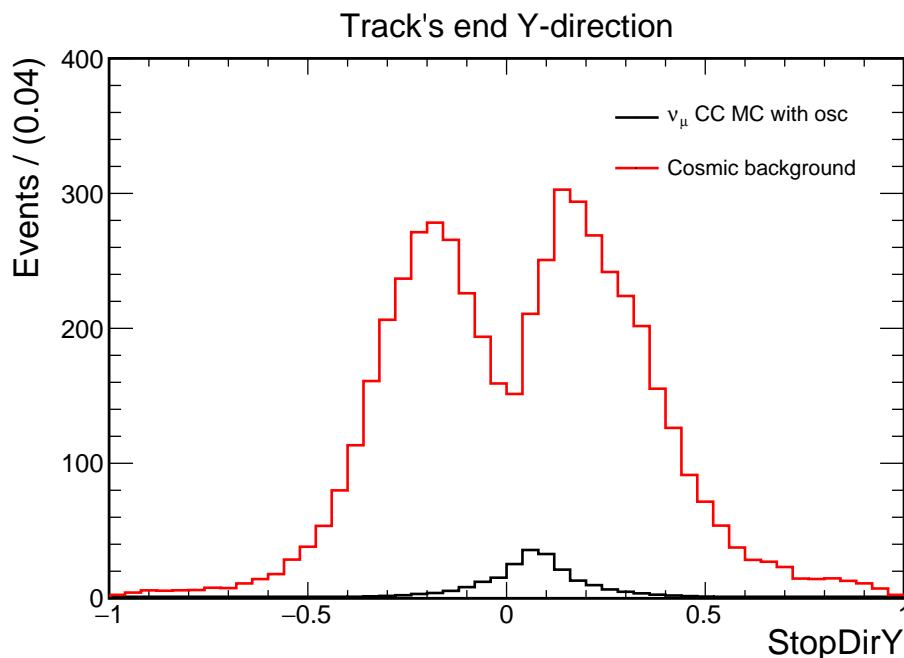
Figure 7.5: Primary Track's End Y-Direction.
Two population structure is clearly visible for cosmic rays background, this is an artifact of Kalman tracker. Figure 7.3b shows members of these populations. The tracker reconstructs a track with an assumption that its starting point is always to the right of its end point.

since it has information about cosmic ray direction as ray enters the detector.

Figure 7.8 shows that escaping sample still has noticeable cosmic ray background and the next section develops a few more optimized cuts to decrease further the rest of background.

7.2.3 Selection

Following the section 7.1.3 for contained sample, ν_μ CC selection for escaping sample is exactly the same, namely ReMid and CVN score have to be grater than 0.5. Figure 7.9 shows ReMId value for events which pass Base 7.2.1 and Preselection 7.2.2 cuts.

The last two criteria are based on the facts that cosmic rays tend to be vertical and the majority of them are muons with small amount of deposited energy outside the reconstructed track. Figures 7.10 and 7.11 illustrate previous statement - the first figure
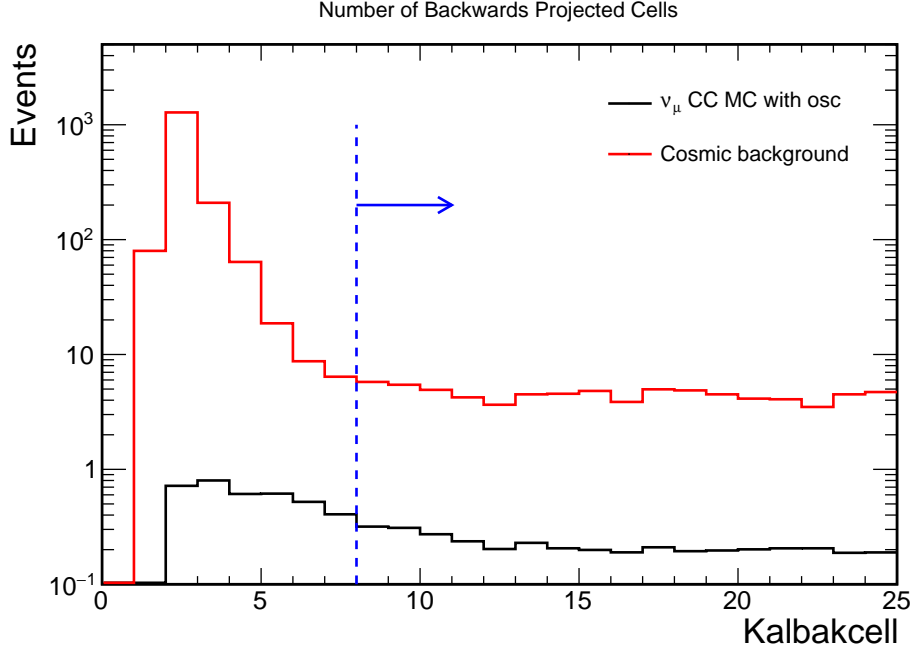
Figure 7.6: Number of Backwards Projected Cells.
Three order of magnitude more cosmic events for lower end of number of backwards projected cells comes from cosmic rays which move along the positive Z-axis. See left example of cosmic ray in figure 7.3b.

shows reconstructed transverse momentum over total momentum $\left(\frac{p_t}{p}\right)$ and the second one shows reconstructed hadronic energy of the events after Base and Preselection cuts. However, a simple cut on event hadronic energy leads to a significant loss in signal and as result to a worse experiment sensitivity for θ_{23} and Δm^2_{32} parameters. To bypass this unpleasantness one can use a strength of CVN classifier - it predicts not only type of neutrino but also a type of interaction the neutrino participated in. Figure 7.12 shows distribution of reconstructed hadronic energy for different type of neutrino interaction determined by CVN classifier. The final cut optimization is done for $\frac{p_t}{p}$ variable and reconstructed hadronic energy of CVN QE-like events.

The ultimate goal of this work is to measure θ_{23} and Δm^2_{32} parameters which govern muon neutrino oscillations and the tuning of selection criteria is done to maximize the experiment sensitivity. However, to measure a sensitivity one needs to estimate energy for the selected events and to make an energy estimator one needs the final selection

Track's end Y-direction
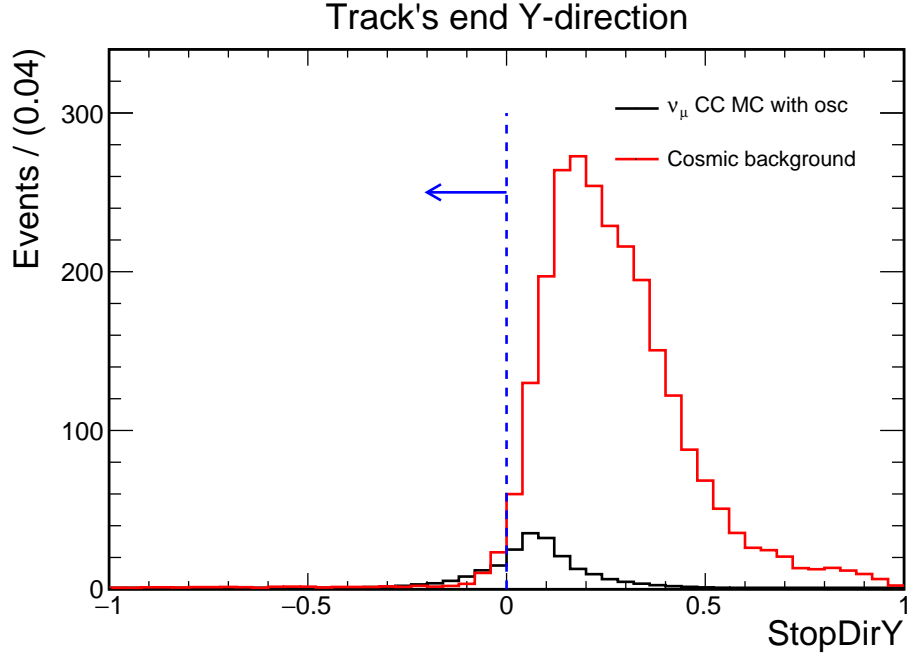
Figure 7.7: Primary Track's End Y-Direction after two preselection cuts.
Cut on the number of cells from the edge of the detector to hadronic cluster has a small impact on all distributions, it is needed only for a clean sample to train energy estimator on. On the opposite, Kalbakcell cut removes half of the cosmic background.

criteria. To break this cycle, an energy estimator (see chapter 8) is trained on the events that do not pass the final cuts but rather close to final selection criteria. And then, the final selection are chosen by using that energy estimator.

The final selections after optimization are

- $\frac{p_t}{p} < 0.6$,

- hadronic energy for CVN QE-lie events is less than 0.1 GeV.

Figures 7.14, 7.15, 7.16 show X, Y, and Z-position of primary track start (position of interaction point), figures 7.17, 7.18, 7.19 show distributions of primary track start in planes X-Z, Y-Z, X-Y, figure 7.20 shows length of the primary track for signal and cosmic events. All these figures show events which pass full escaping sample selection criteria.
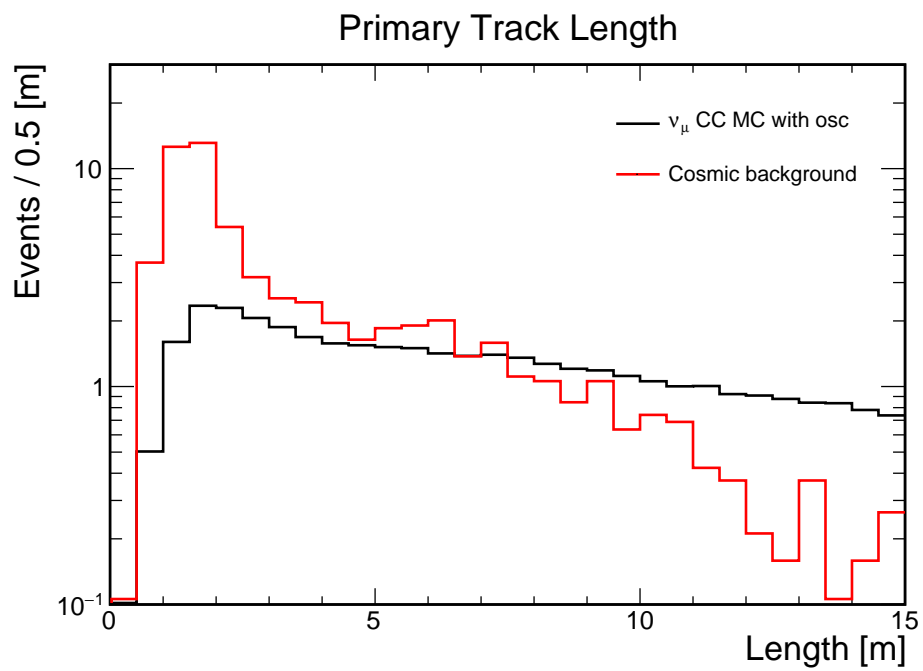
Figure 7.8: Length of Primary Track After Base and Preselection Cuts. The plot illustrates abundance of cosmic ray background after base and preselection cuts.
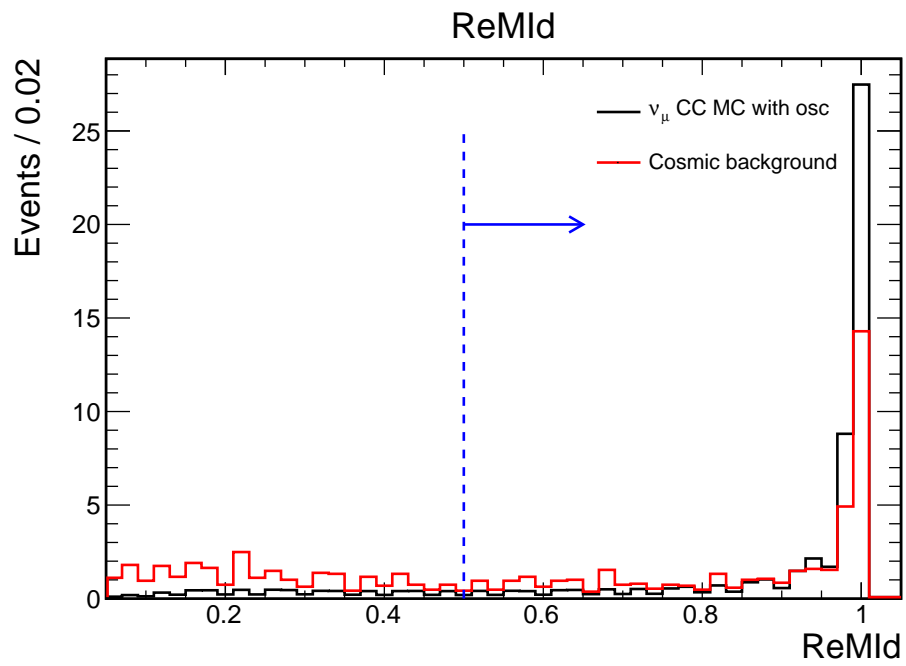
Figure 7.9: ReMId value for the events which pass Base and Preselection cuts. Cut on ReMId value is chosen similar to contained sample. Low value means a poorly reconstructed muon track or track produced by a pion.
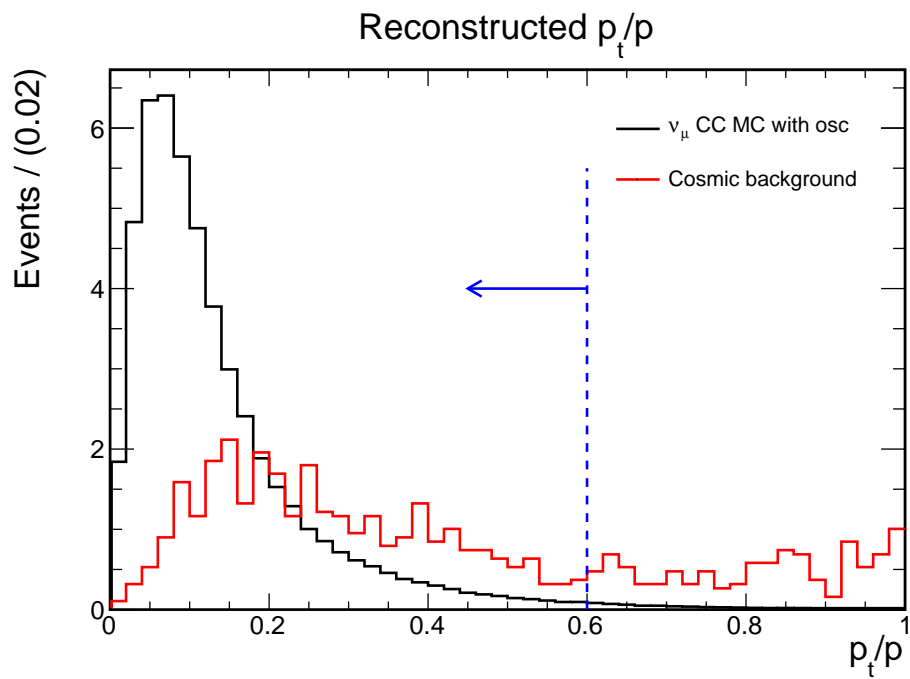
Figure 7.10: Reconstructed $\frac{p_t}{p}$.
Distribution of reconstructed transverse momentum over total momentum for events
which pass Base, Preselection and ReMId grater than 0.5 cuts.
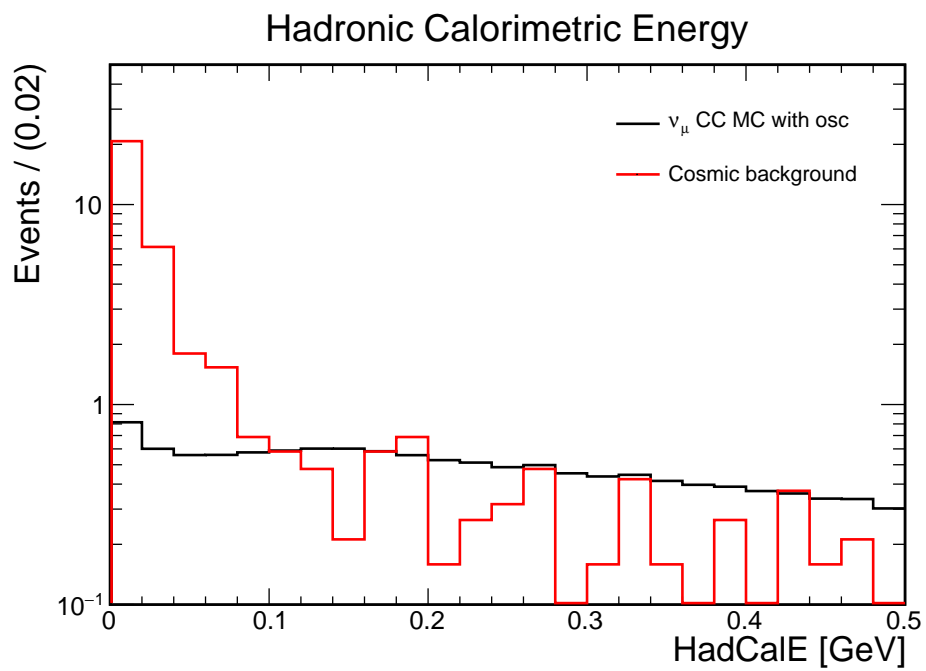
Figure 7.11: Hadronic Calorimetric Energy.
Distribution of hadronic calorimetric energy for events which pass Base, Preselection
and ReMId grater than 0,5 cuts. Simple cut on this variable significantly hurts
sensitivity, thus different approach is taken.

(a) Signal.

(b) Cosmic Background.
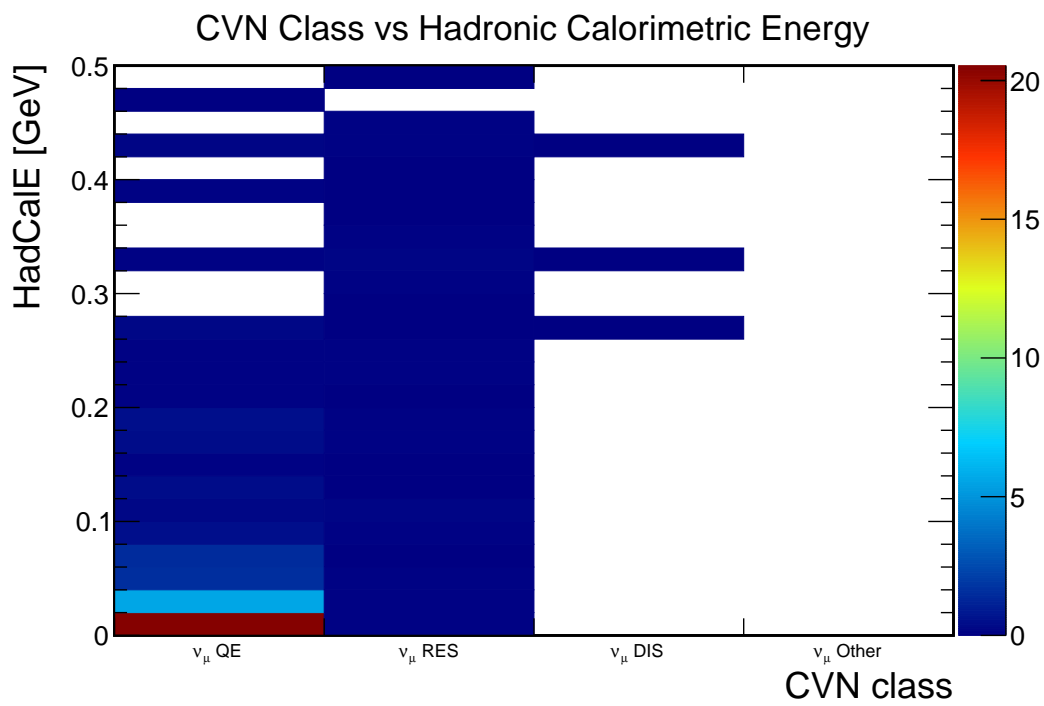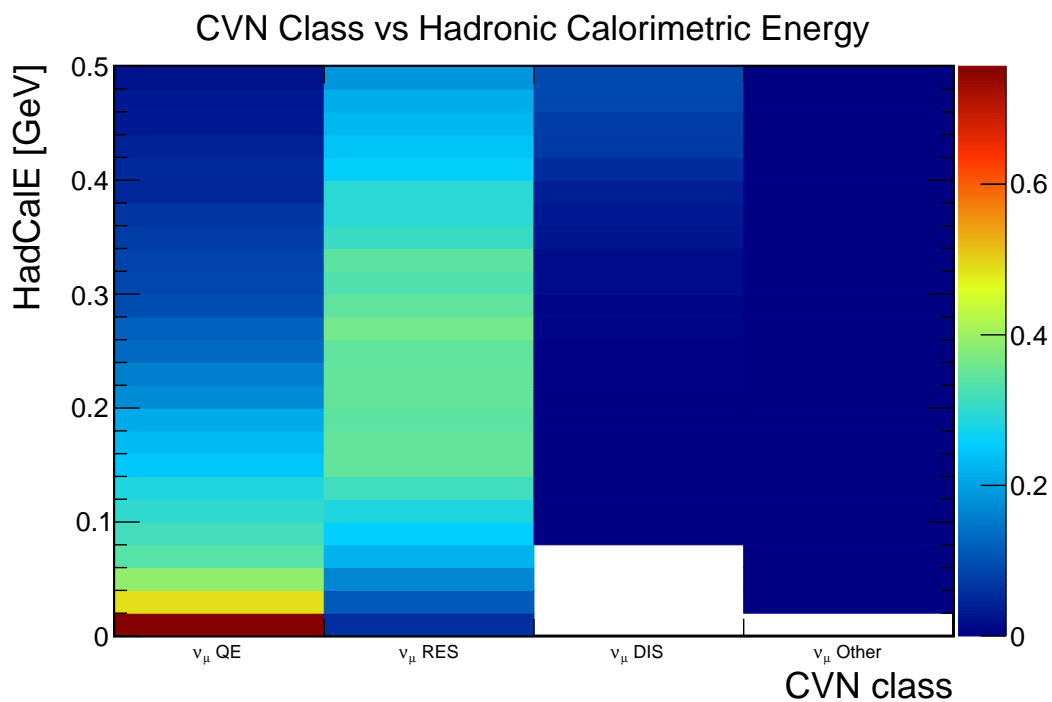
Figure 7.12: Hadronic Calorimetric Energy for Different CVN Classes.
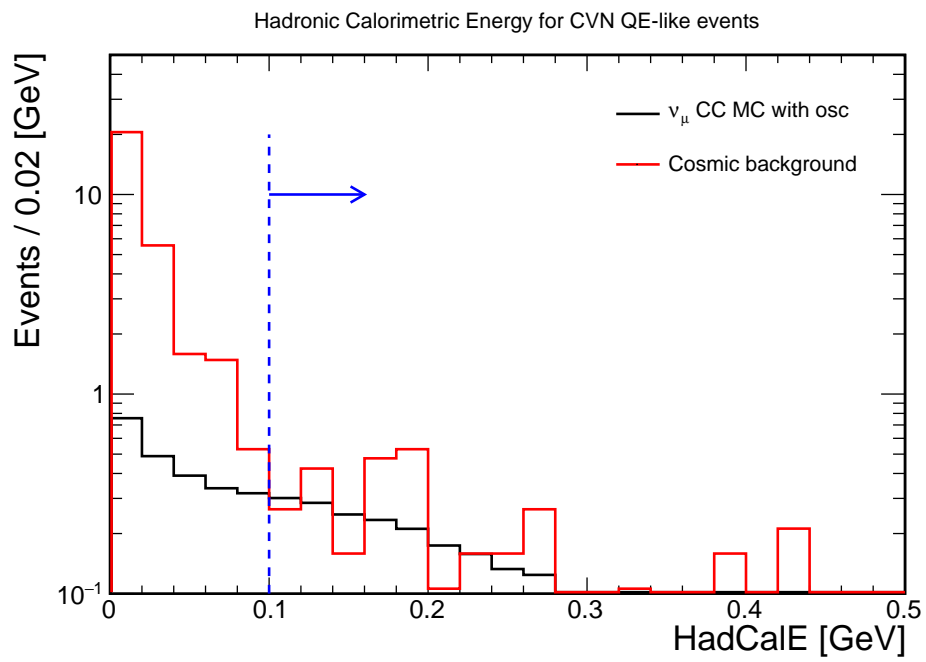
Figure 7.13: Hadronic Calorimetric Energy for CVN QE-like events. Distribution of hadronic calorimetric energy for events which pass Base, Preselection, ReMId grater than 0,5 cuts and classified by CVN as QE events. Optimized cut was chosen at 0.1 GeV.
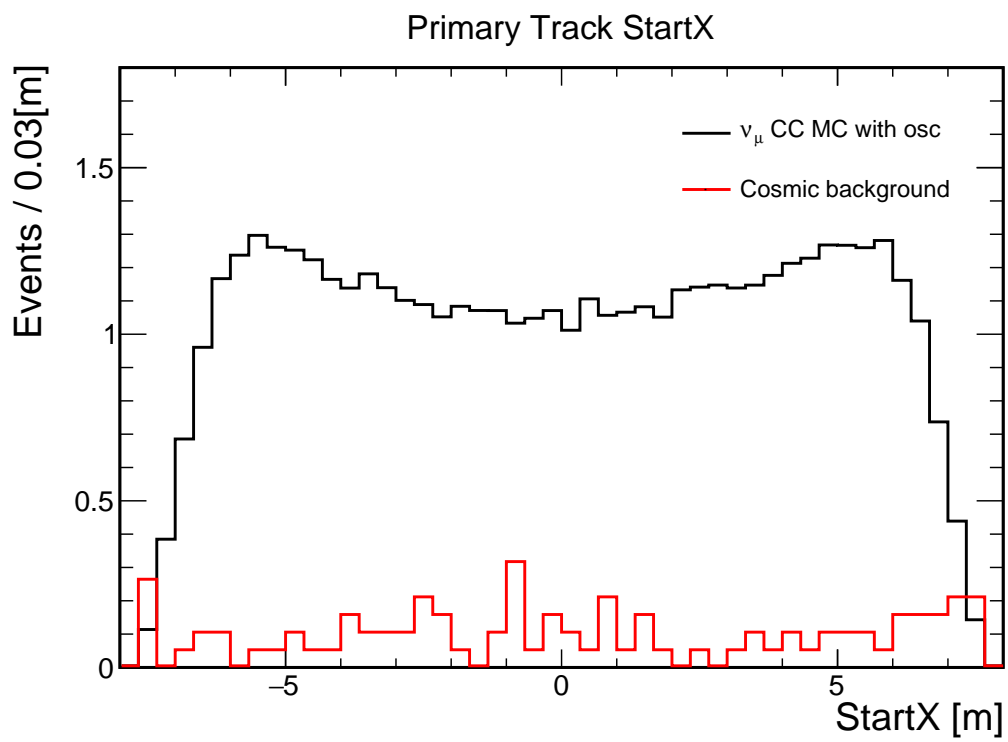
Figure 7.14: StartX Position of Primary Track.
Distribution of primary track Start X-position for events which pass all selection criteria.
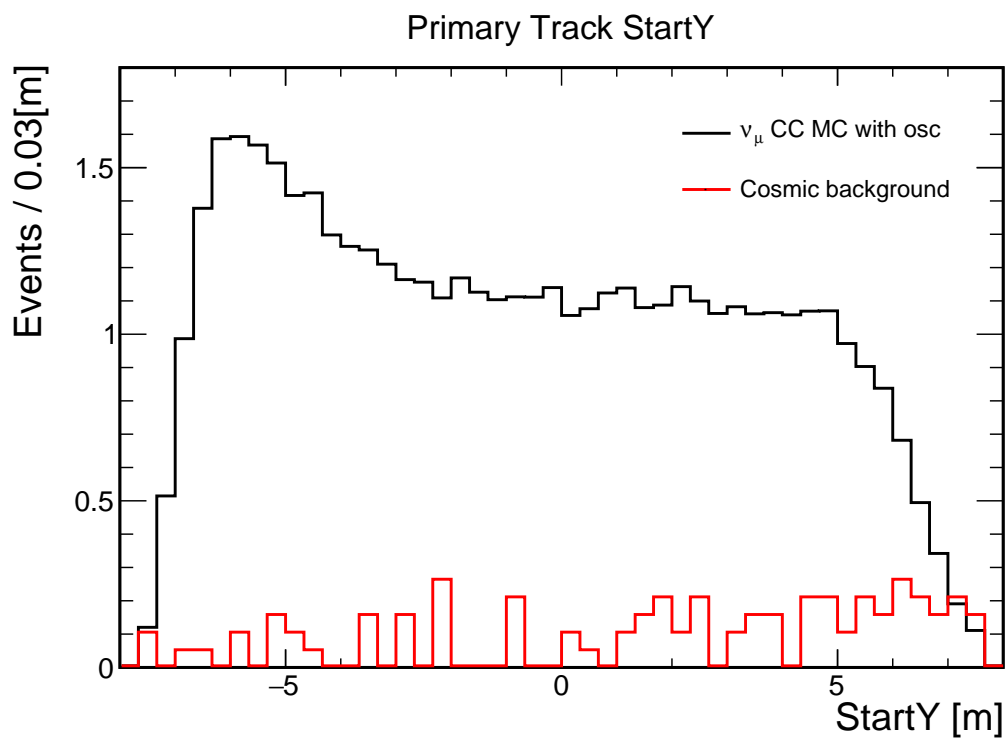
Figure 7.15: StartY Position of Primary Track.
Distribution of primary track Start Y-position for events which pass all selection criteria.
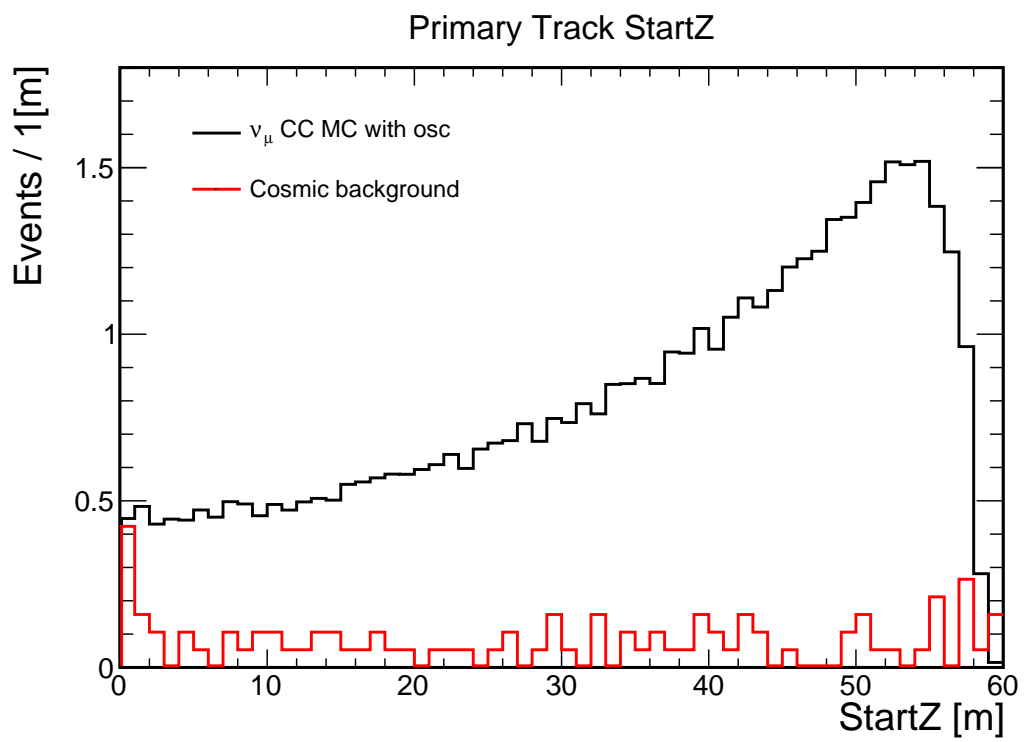
Figure 7.16: StartZ Position of Primary Track.
Distribution of primary track Start Z-position for events which pass all selection criteria.

(a) Signal.

(b) Cosmic Background.
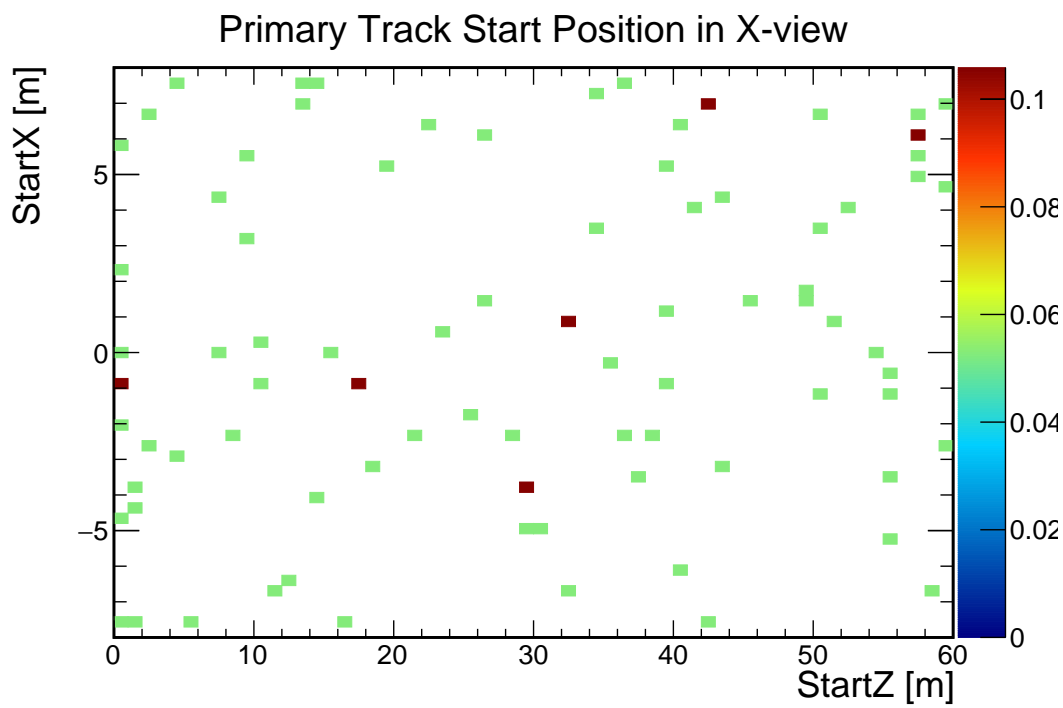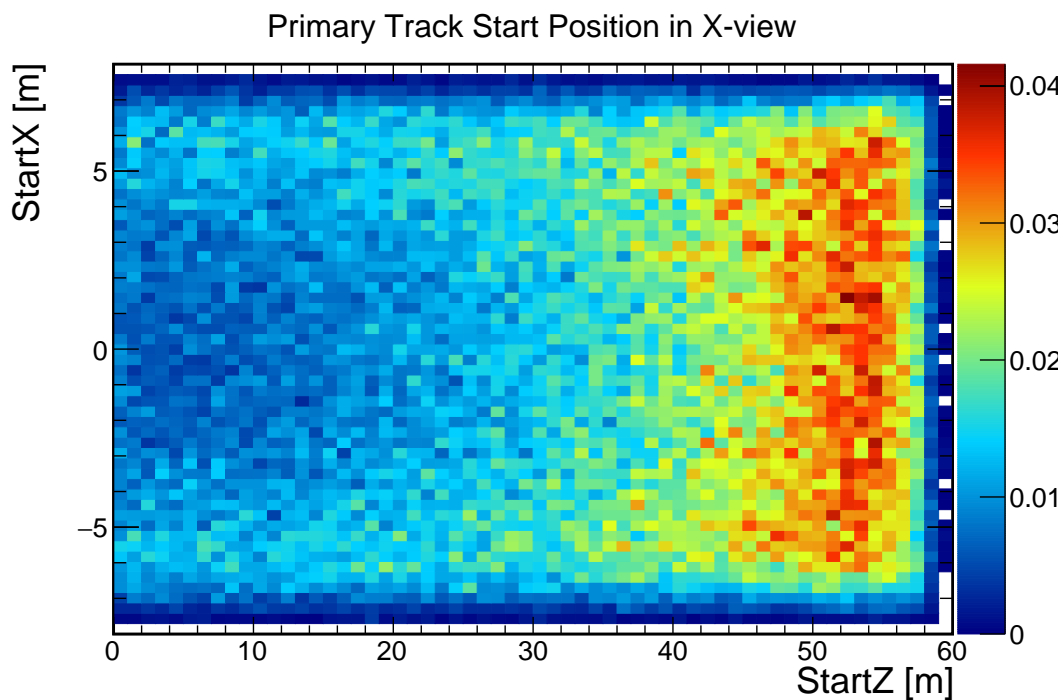
Figure 7.17: Distribution of Primary Track Start in X-view.
Events pass all the escaping sample selection criteria. X-view can be interpreted as
look from the top of the detector.

(a) Signal.

(b) Cosmic Background.
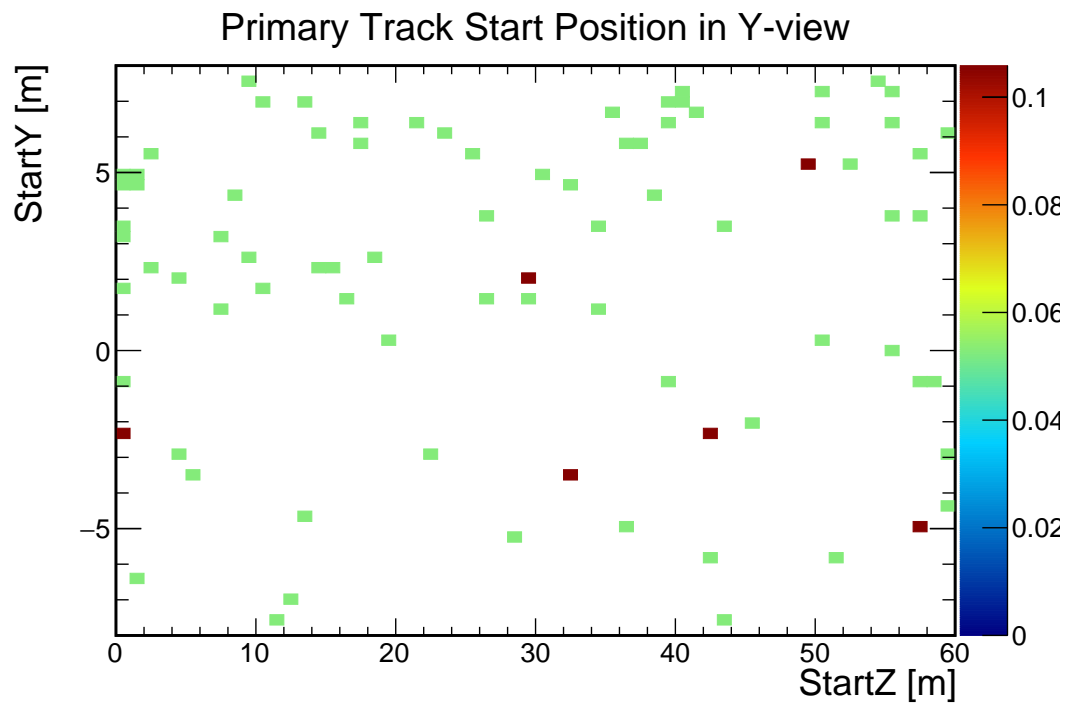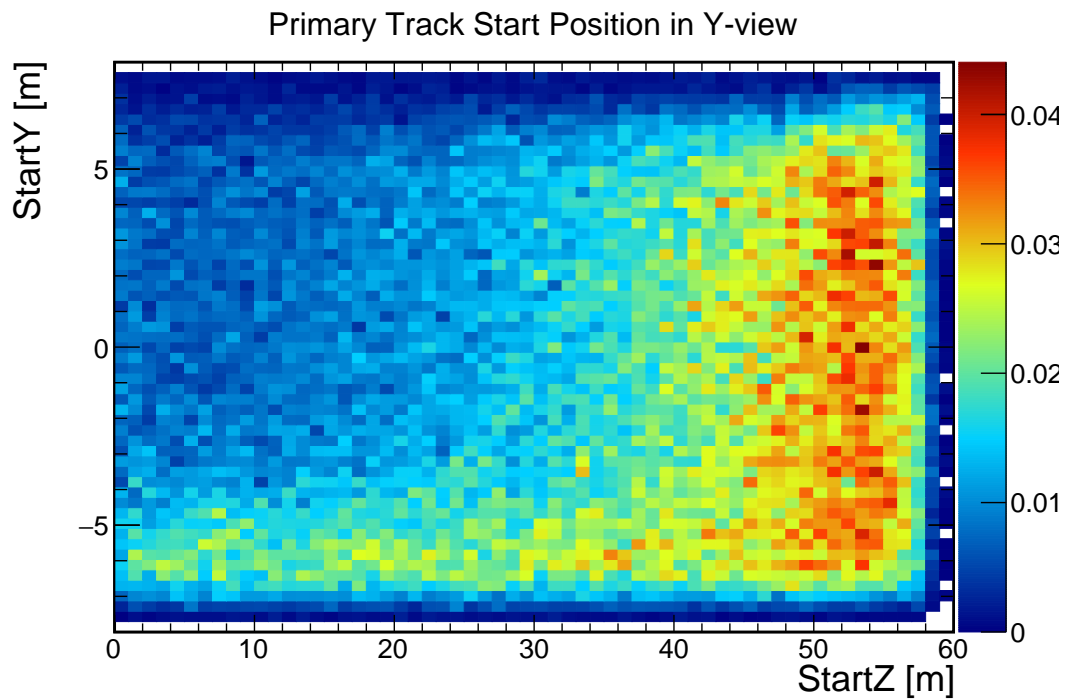
Figure 7.18: Distribution of Primary Track Start in Y-view.
Events pass all the escaping sample selection criteria. Y-view can be interpreted as look from the side of the detector.

Primary Track Start Position in X-Y view

(a) Signal.

Primary Track Start Position in X-Y view
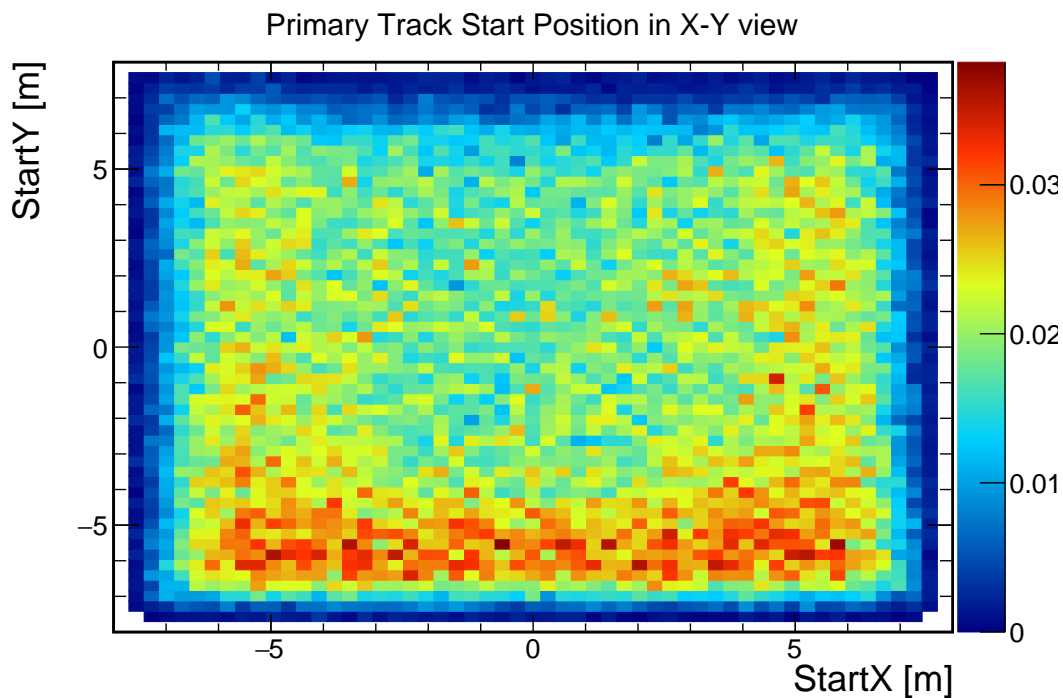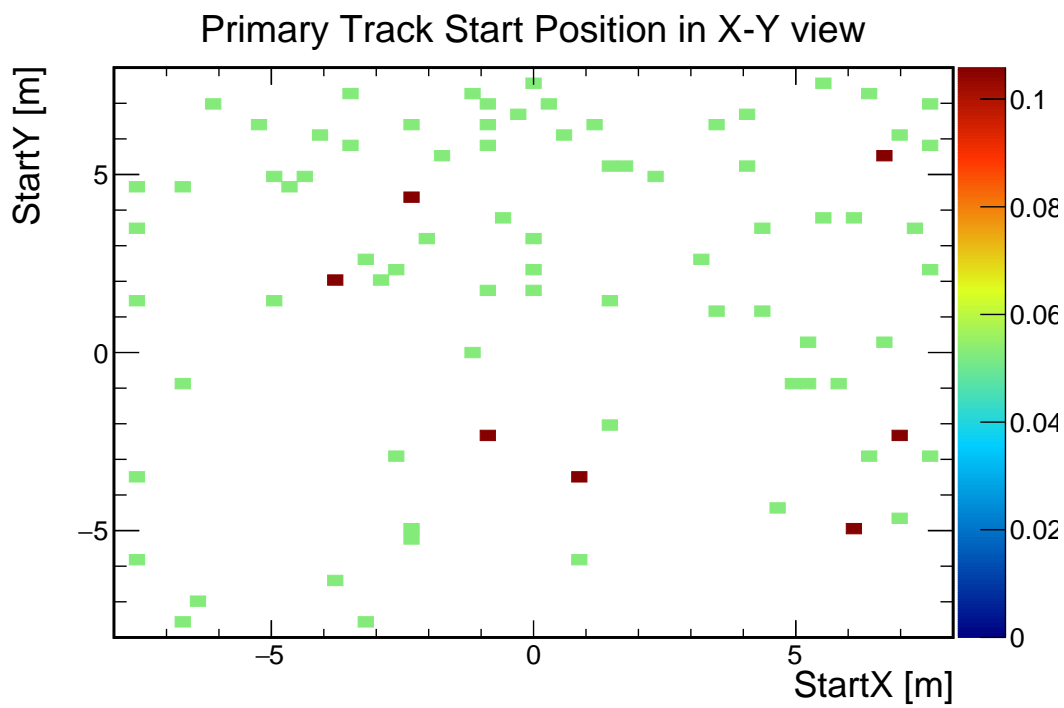
(b) Cosmic Background.

Figure 7.19: Distribution of Primary Track Start in X-Y view.
Events pass all the escaping sample selection criteria. X-Y view can be interpreted as look from the side of the detector along the beam direction.
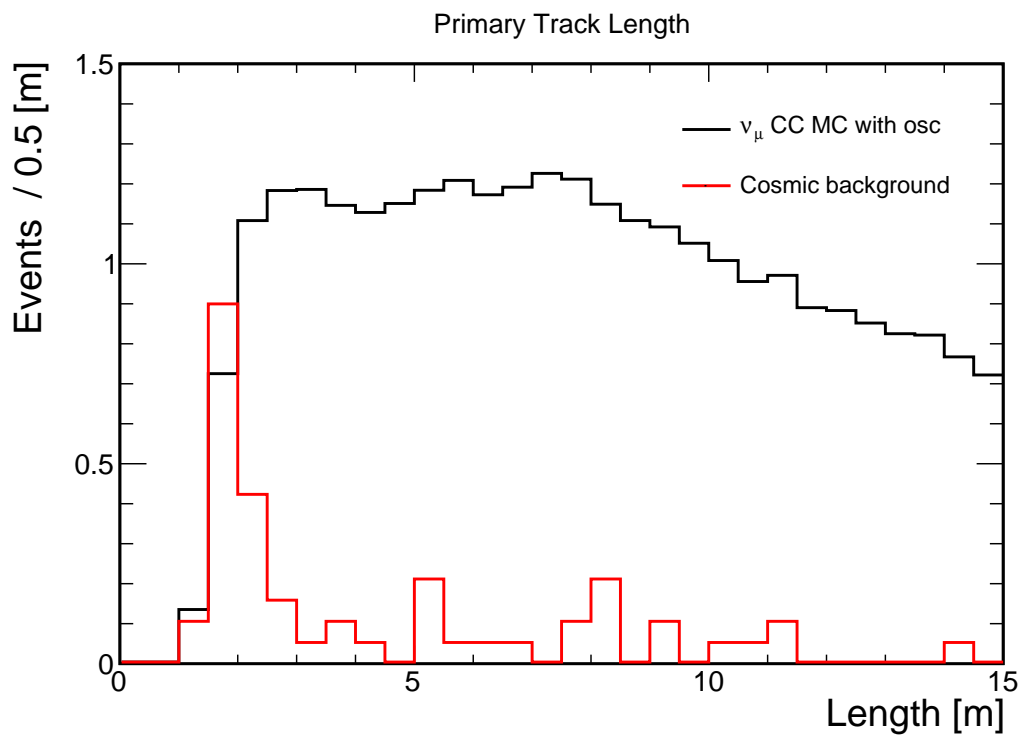
Figure 7.20: Length of Primary Track.
Events pass all the escaping sample selection criteria.

7.2.4 Summary

In this section all selection criteria are briefly stated together.

Base cuts

- data quality,

- failed containment cut for the contained sample,

- CVN > 0.5,

- cosmic rejection PID value is > 0.48.

Preselection

- number of backwards projected cells for primary track is grater than 7,

- number of cells from detector edge to hadronic cluster is grater than 2,

- Y-component of track's direction at its end is less than 0.

Selection

- ReMId is greater than 0.5,

- $\frac{p_t}{p}$ is less than 0.6,

- hadronic energy for CVN QE-like events is grater than 0.1 GeV.

This concludes the escaping and contained events selection chapter, the next step is to determine selected events energies.

Chapter 8

Energy Estimator

This chapter discusses the energy estimation for the selected events with selection criteria developed in previous chapter. How energy is measured for the contained sample one can refer to section 6.5 of event reconstruction chapter. For the escaping events, the energy estimation algorithm is discussed in this chapter.

8.1   Different Approaches

Similar to energy estimation for contained sample events, the escaped event is divided into two parts: muon track (track with the highest ReMId score) and hadronic cluster. Hadronic cluster is the set of all hits in the slice with removed hits on primary track. Preselection cut, which keeps hadronic cluster to at least 3 cells from the edge of the detector, makes sure that all the activity associated with hadrons is contained. Thus, hadronic energy of the selected escaping event can be estimated with the help of the same algorithm as for contained event, but another approach is needed for the muon track.

The following subsections briefly describe several approaches taken in attempt to reconstruct neutrino energy by using either an analytic expression for the neutrino energy or a lookup table.

8.1.1 Quasi-Elastic Formula

Interactions which constitute a significant fraction of the ν_μ CC interactions in NOvA are QE interactions, for these interactions an analytic expression for neutrino energy, which is written in terms of observable variables can be used. For escaping events observable quantities are hadronic energy and the primary track angle[1].

The well known quasi-elastic formula for neutrino energy reconstruction in terms of muon energy E_μ and scattering angle

$$E_\nu = \frac{E_\mu m_N - \frac{m_\mu^2}{2}}{m_N - E_\mu + p_\mu \cos\theta} \tag{8.1}$$

can be easily rewritten in terms of reconstructed hadronic energy E_{had} and scattering angle. With assumptions $E_\mu >> m_\mu$ and that reconstructed hadronic energy is kinetic energy of a hadron neutrino interacted with, the previous formula transforms into

$$E_\nu = E_{had}\Big[1 + \sqrt{1 + \frac{4m_N}{E_{had}(1 - \cos\theta)}}\Big]. \tag{8.2}$$

In practice this approach to neutrino energy reconstruction turned out to be unsatisfactory. Firstly, figure 8.1 shows true distribution of neutrino interaction types for energies in NOvA experiment, for significant fraction of events the formula is not applicable. Secondly, reconstructed hadronic energy resolution for lower energy (exactly where QE events are expected) is worse, see figure 9.18 in [52]. Finally, for majority of muon tracks $\cos\theta$ is close to one which leads to a big uncertainty in $\frac{1}{1-\cos\theta}$ term.

8.1.2 Lookup Table

The other approach is to measure hadronic energy of the event together with the scattering angle of primary track and make a table. Rows and columns of the table are intervals in reconstructed hadronic energy and scattering angle - 5 bins for hadronic energy from 0 GeV to 1 GeV and 5 bins for cosine of scattering angle from 0.5 to 1. For every one of these 25 bins distribution of true energy of neutrino is made and mean is

---

[1]Angle between muon track and incoming neutrino.
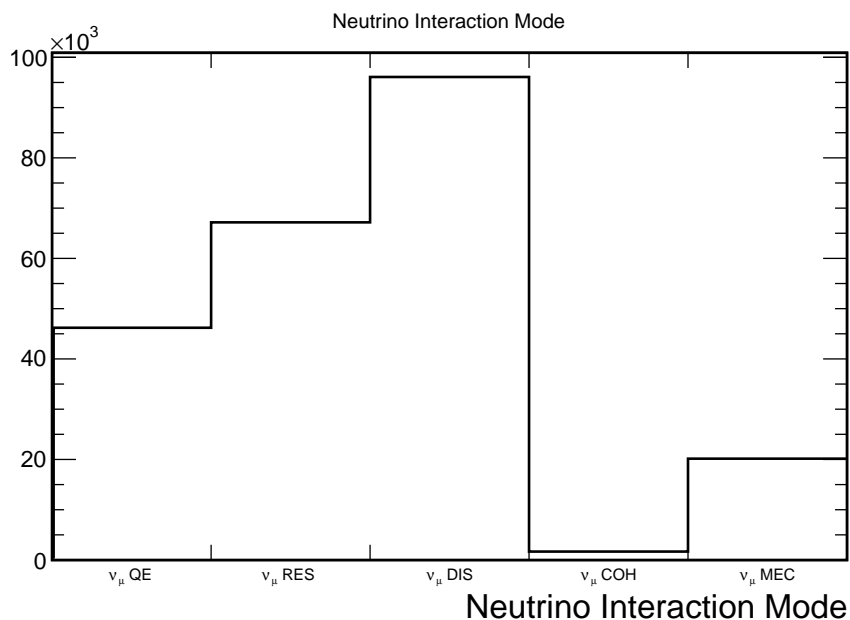
Figure 8.1: True Neutrino Interaction Mode.
Only 20% of all neutrino interactions which pass Base Cut 7.2.4 are QE, this fraction even less for the full selection as some CVN QE-like events are not allowed.

calculated, that mean value is an entry in the table.

During the test period entry of the table is used as reconstructed energy for the event with corresponding reconstructed hadronic energy and scattering angle of primary track. Results of the approach also turned out to be unsatisfactory independent of number of bins for reconstructed hadronic energy and scattering angle. Reconstructed energy is mapped to a narrow region around 2 GeV and no power was left to distinguish between maximal mixing and non-maximal one. In other words, sensitivity of the experiment was not improved by using this energy estimator for escaping events.

8.2 Machine Learning Regression Algorithms

Approaches described in the previous section while being simple and easy interpretable do not provide good enough improvement in experiment sensitivity. The natural next step in searching for a good energy estimator for escaping events is to try different machine learning regression algorithms such as an artificial neural network, k Nearest

Neighbours and decision trees. All these algorithms are applicable for regression problem and all of them were examined with the same set of input variables.

8.2.1 Input Variables

The first step in construction of muon energy estimator is to determine which variables contribute most of the information about true muon energy. The following set is probably the fullest set of these variables. Extensive search for other variables did not provide variables which improved muon energy estimator.

- Track Length. The length of the primary track contains all the information about muon energy when track is fully contained in the detector and provides a lower limit for the energy otherwise.

- Track scattering. The cumulative sum of all deviations from a straight line in degrees normalized by track length. Muon with a small energy has a shorter track and a lot of scattering while propagating through the detector resulting in a bigger track scattering variable. This variable discriminates cases with the same amount of contained track but different amount of escaped part.

- Track angle. The variable describes the angle between the reconstructed track and incoming neutrino[2].

- Track Energy Per Hit. Visible energy of the track is divided by number of hits in the track. The variable helps to determine if muon is minimum ionizing particle or not, this has a strong connection with the muon total energy.

During the training period every set of these four variables is supplemented with a true muon energy in the corresponding event. These variables are not completely independent as can be seen in figure 8.2. It is known that regression algorithms achieve better results when input variables are decorrelated, thus decorrelation and gaussinization procedures were carried out and final distributions before they enter training are shown in figure 8.3.

---

[2]At the far detector neutrino source is a point source and direction of incoming neutrinos could be determine.
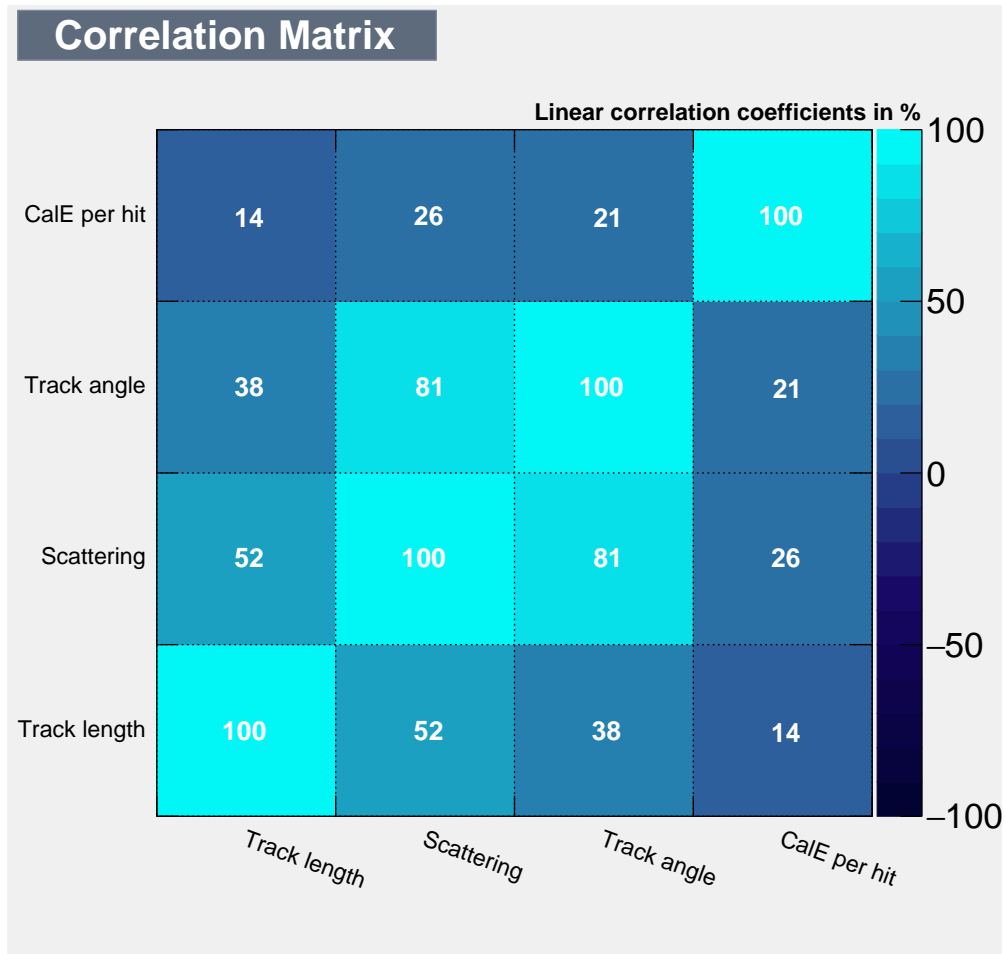
Figure 8.2: Correlation Matrix.
Correlations between input variables for BDT algorithms. The algorithm performs better if input variables are first transform into a Gaussian form and then decorrelated.

8.2.2 Training

Training and testing samples contain equal number of events - 101079. This events in addition to escaping sample selection are subject to one more selection. Namely, events have to be from the files with subrun number less than 55. This criteria selects events from all runs with different detector states, so energy estimator during the training process exposed to events it could see in the final analysis. Events with subrun equal or more than 55 are used for final validation.
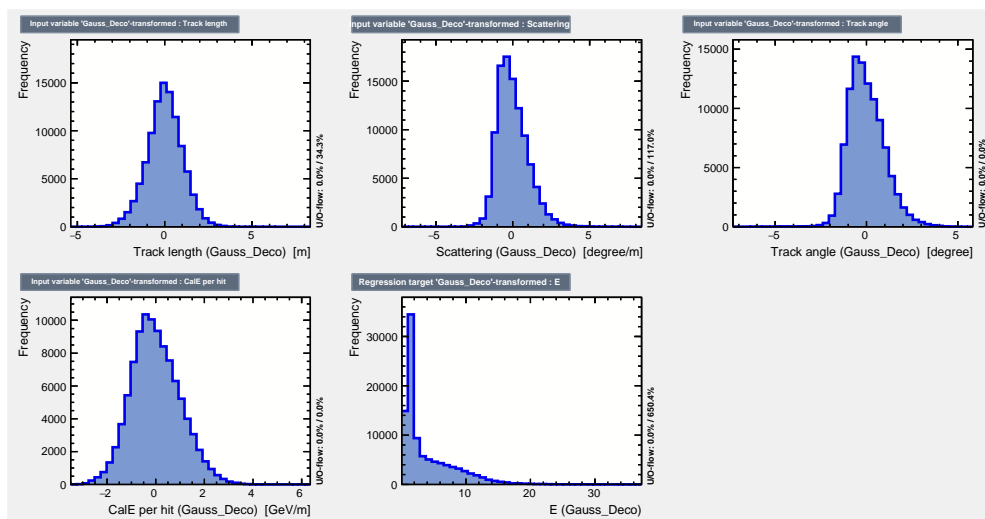
Figure 8.3: Input and target variables after decorrelation and gaussinization procedures were performed.

Early tests showed that artificial neural net and k nearest neighbours algorithms have a significantly worse performance and these algorithms are not used for final muon energy estimator tuning. On the other hand, results for the Boosted Decision Trees (BDT) turned out to be more promising. The next several paragraph briefly explain how BDT work and what hyper parameters are chosen for muon energy estimator.

Regression decision tree is a tree-like graph where data flow from root to leaves through several branching points. Root and branching points correspond to questions and if data satisfies the question it propagates through one branch, if not then it propagates through another branch. During the training process tree learns its structure and populates leaves with examples from training sample. When a new data point is fed into the tree it propagates through the tree following the questions in branching points and finally reaches one of the leaves. Then regression output of the tree is an average over all training examples in the leaf.

Unfortunately, the decision tree shows worse performance on average compare to other algorithms and tree structure is unstable on training data meaning that small changes leads to drastically effect on tree structure. Nevertheless, performance could be improved via ensemble method where many different trees are fit and predictions are aggregated across the trees. Ensemble sometime called a forest.

One more way to improve performance of decision trees is to use boosting. A function which is needed to be learnt, in this case muon energy estimator E_{muon}, taken as a weighted sum of base functions $f(\vec{x}, \alpha)$ - single tree - often called "weak learners".

$$E_{muon}^N(\vec{x}, \vec{\beta}, \vec{\alpha}) = \sum_{n=0}^N \beta_n f(\vec{x}, \alpha_n), \tag{8.3}$$

where $\vec{x}$ is a input vector, $\vec{\beta}$ are weights for different trees and $\vec{\alpha}$ are parameters of the trees. Boosting is a iterative process where each subsequent tree $f(\vec{x}, \alpha_{N+1})$ learns in a way to minimize a loss function[3] for $E_{muon}^N(\vec{x}, \vec{\beta}, \vec{\alpha}) + \beta_{N+1} f(\vec{x}, \alpha_{N+1})$.

It is recommended not to use trees with depth deeper than 8, so a depth 5 of was chosen. Another hyper parameter for BDT training is the number of weak learners. Ten different options were tried and the best result was achieved for 800.

8.2.3 Performance

The performance of escaping events energy estimator is evaluated by looking at the RMS of the resolution histogram. Resolution is defined as

$$\text{Resolution} = \frac{\text{True Muon Energy} - \text{Reco Muon Energy}}{\text{True Muon Energy}}. \tag{8.4}$$

As can be seen in figure 8.4, muon energy resolution is about **32%**, the distribution is not symmetrical and shifted towards positive values meaning that estimator on average undershoot the escaping muon energy. Correction could be made to make energy estimator to get right muon energy on *average* (mean of resolution histogram is zero), however as it shown in the next chapter this is not necessary. Figure 8.5 illustrates reconstructed muon energy together with cosmic background.

For the final fit reconstructed neutrino energy ($E_\nu = E_{\text{had}} + E_\mu$) is used instead of just muon energy. Hadronic energy resolution is on the order of 20% which leads to **23%** reconstructed neutrino energy resolution. Figures 8.6 and 8.7 illustrate reconstructed neutrino energy resolution and reconstructed neutrino energy together with cosmic background. Similar to escaping muon energy, shift to make neutrino energy

---

[3]Huber loss function is used, $L(E_{muon}, E_{true}) = \begin{cases} \frac{1}{2}(E_{true} - E_{muon})^2 & |E_{true} - E_{muon}| \leq \delta, \\ \delta(|E_{true} - E_{muon}| - \frac{\delta}{2}) & |E_{true} - E_{muon}| > \delta. \end{cases}$

reco_resol_BDT_mu_Full

Mean: 0.094

RMS: 0.322
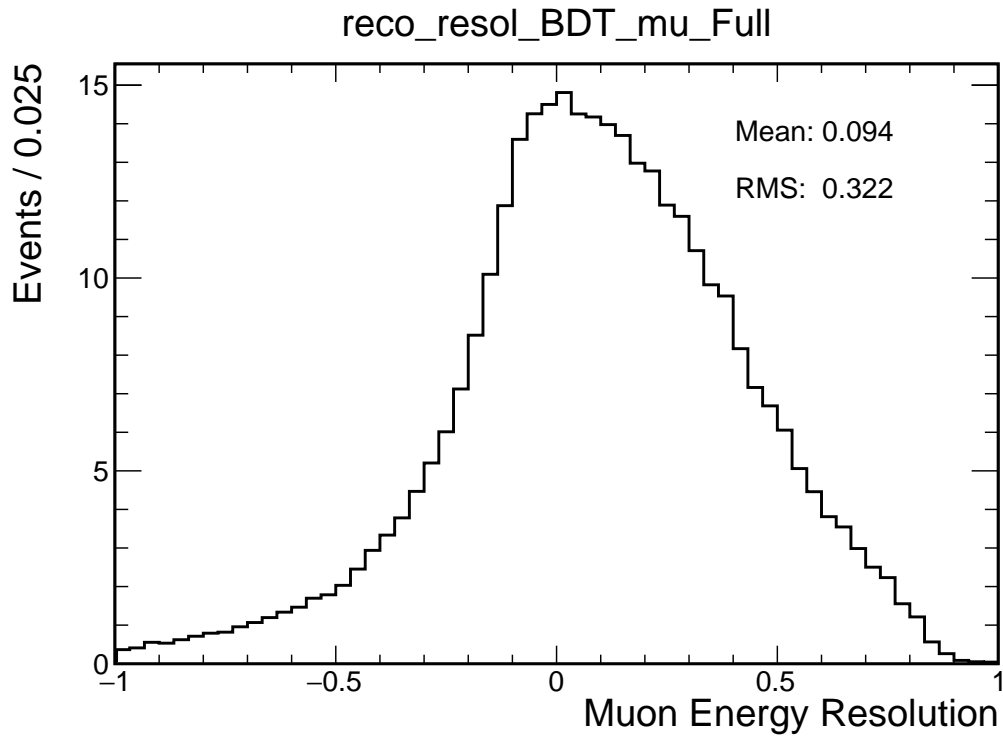
Figure 8.4: Reconstructed Muon Energy Resolution.

correct on *average* is not necessary and it is not improving the experimental sensitivity.

Another useful plots to look at are the neutrino energy resolution as a function of true and reconstructed neutrino energy, figures 8.8a and 8.8b. These plots illustrate that neutrino energy resolution is stable across the measured neutrino spectrum. Two plots on figure 8.9 show how true energy related to reconstructed energy for muon and neutrino respectively.
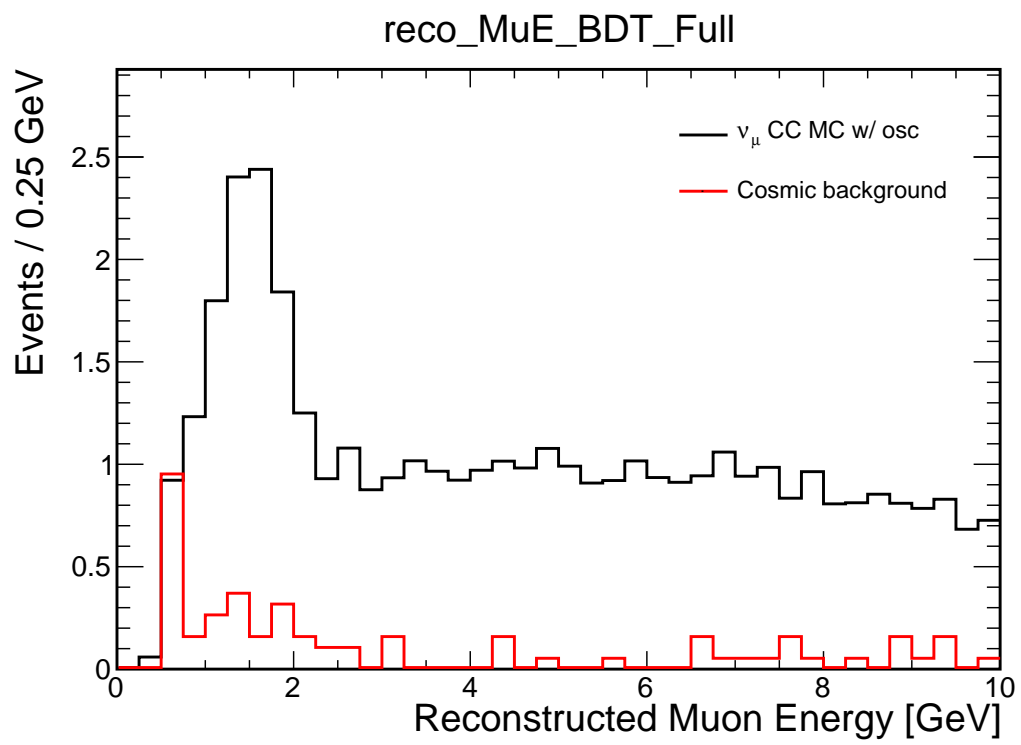
Figure 8.5: Reconstructed Muon Energy.
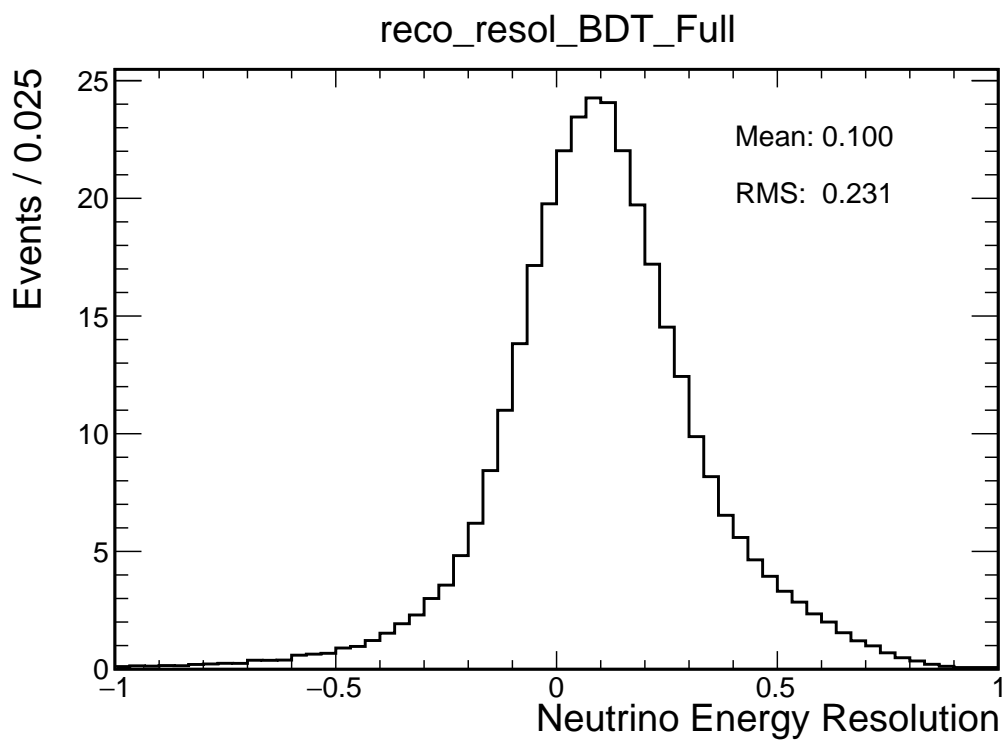
Figure 8.6: Reconstructed Neutrino Energy Resolution.
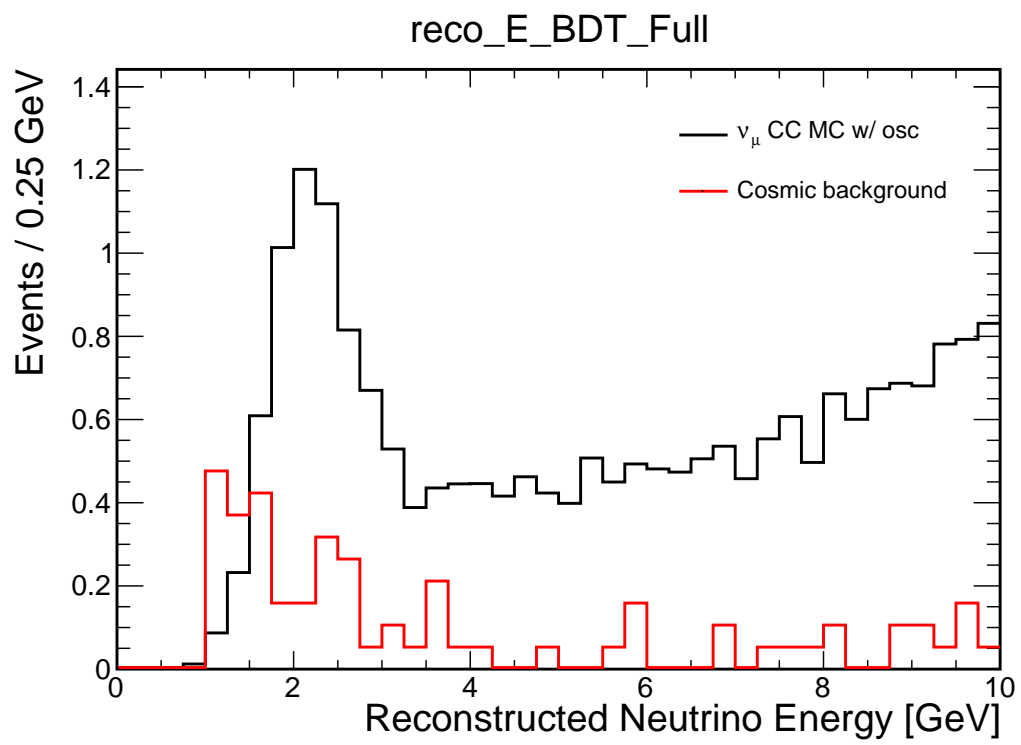
Figure 8.7: Reconstructed Neutrino Energy.

reco_resol_BDT_vs_trueE_Full
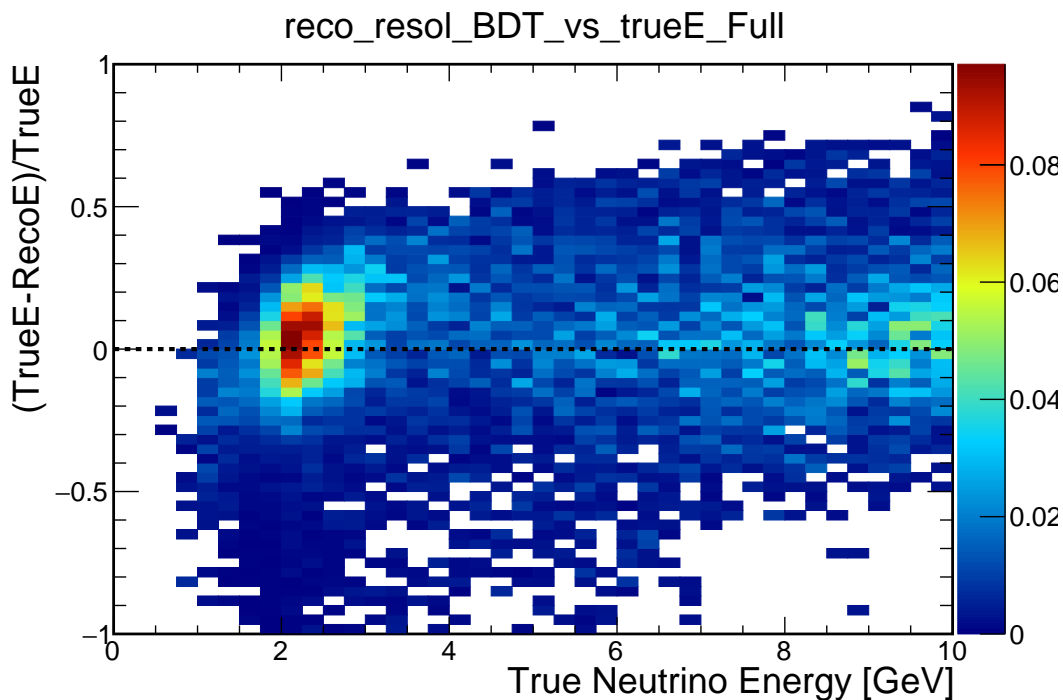
(a) Neutrino Energy Resolution vs True Neutrino Energy.

reco_resol_BDT_vs_recoE_Full
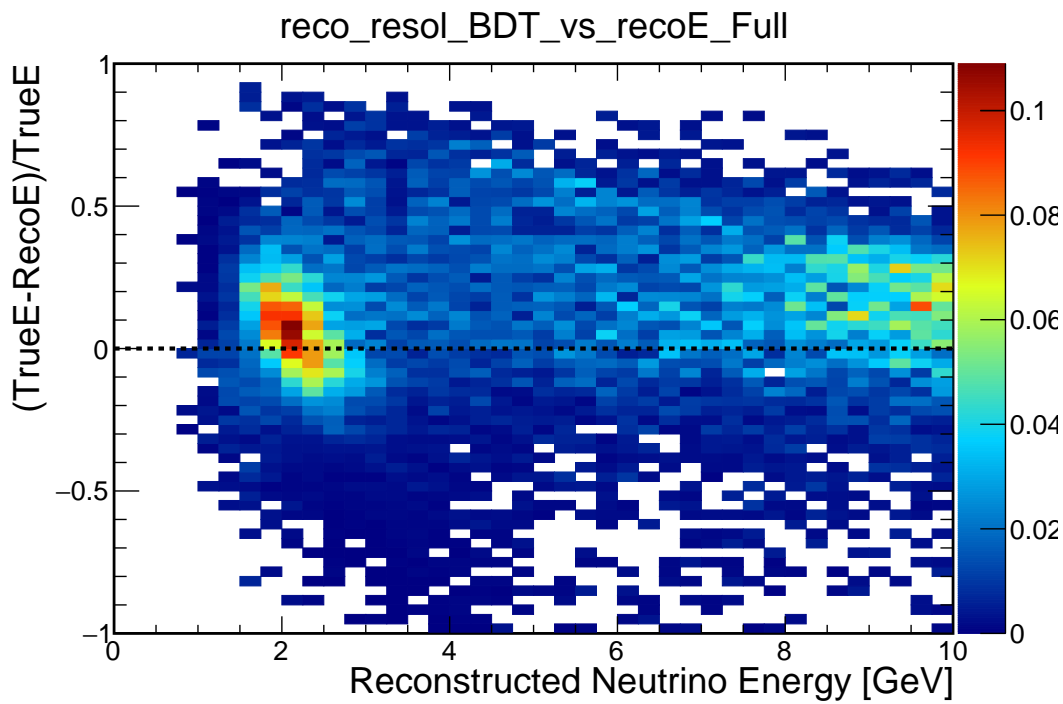
(b) Neutrino Energy Resolution vs Reconstructed Neutrino Energy.

Figure 8.8: Neutrino Energy Resolution vs Neutrino Energy.

reco_trueMuE_vs_BDT_recoMuE_Full
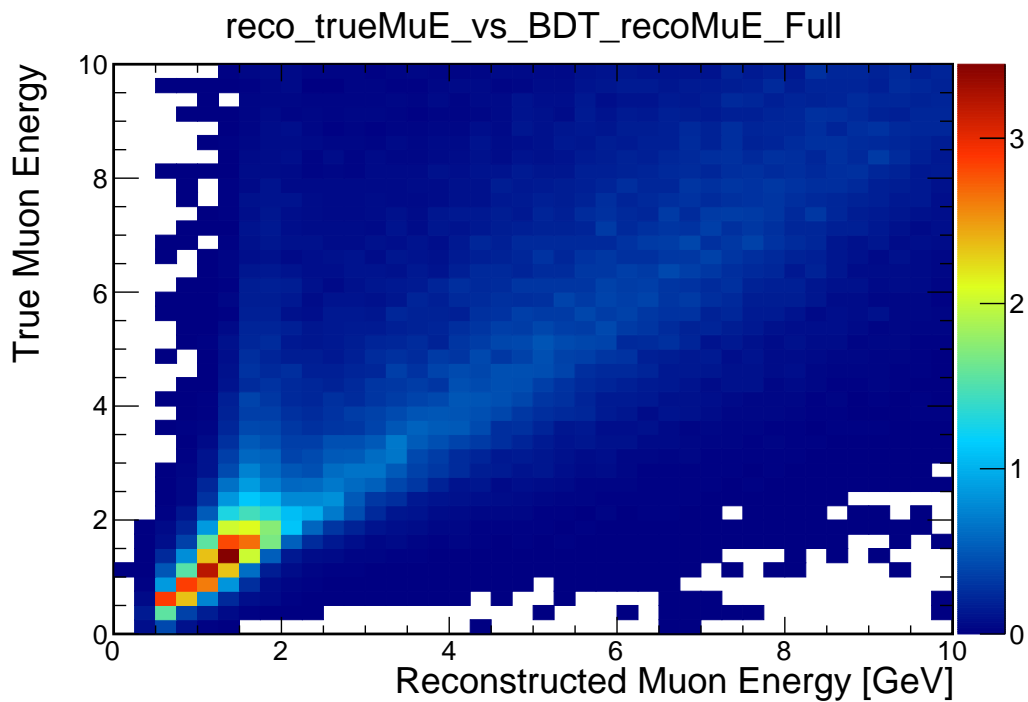
(a) True Muon Energy vs Reconstructed Muon Energy.

reco_trueE_vs_BDT_recoE_Full
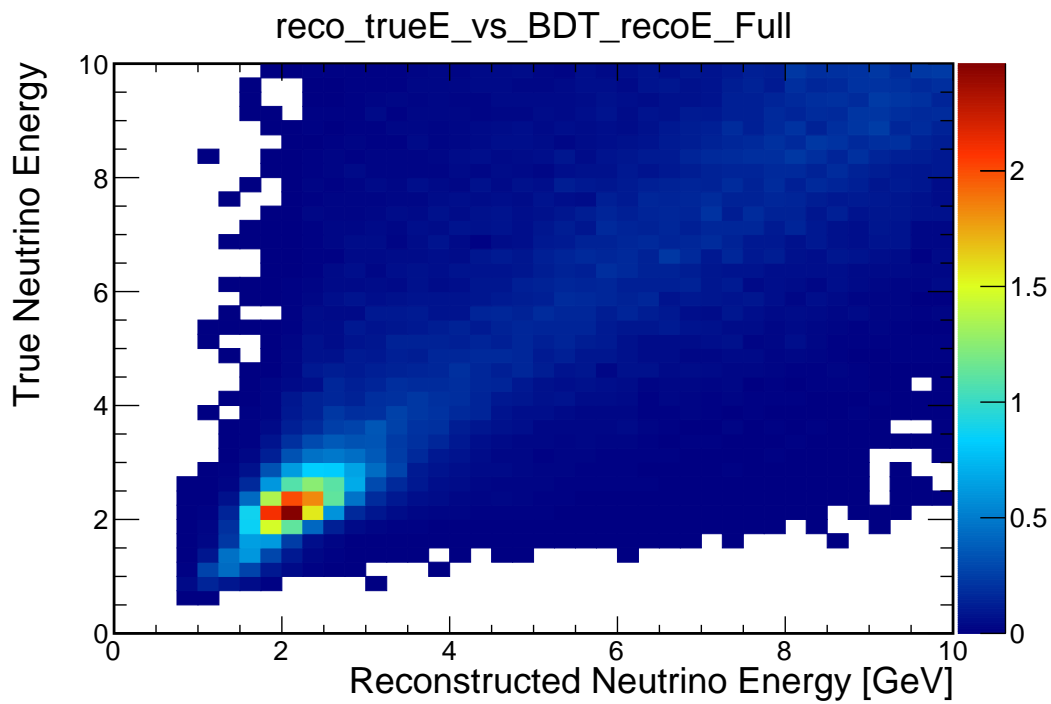
(b) True Neutrino Energy vs Reconstructed Neutrino Energy.

Figure 8.9: True Energy vs Reconstructed Energy.
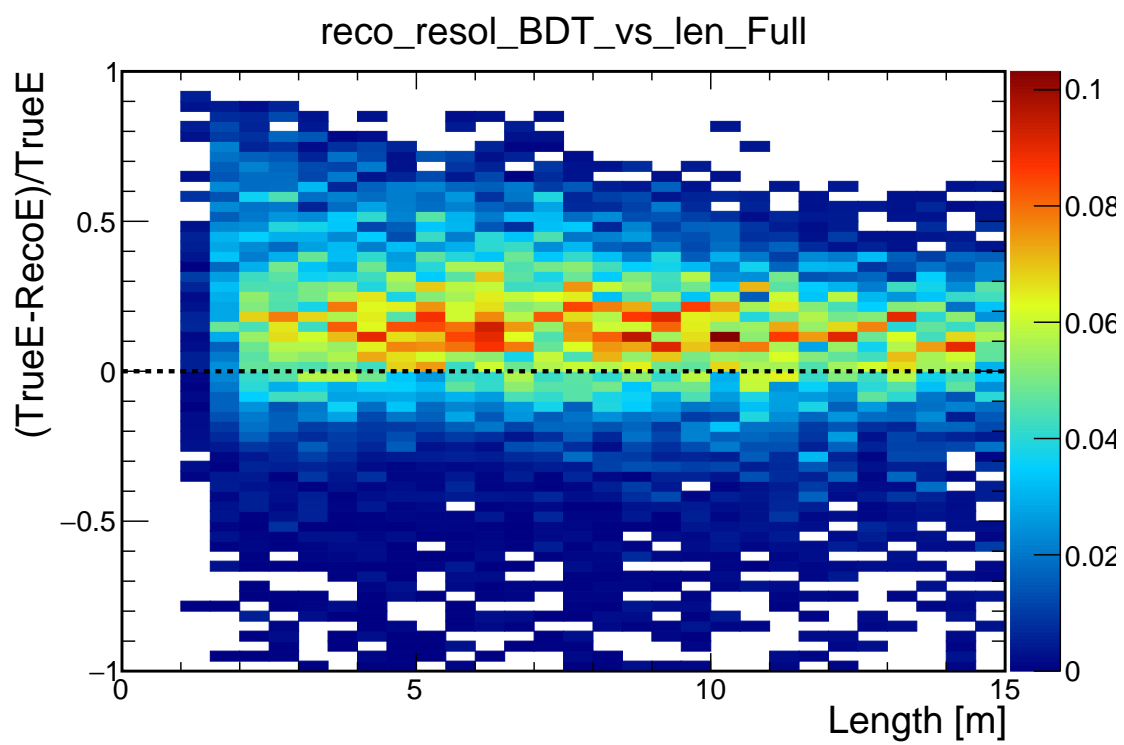
Figure 8.10: Neutrino Energy Resolution vs Length of Primary Track.

Chapter 9

Far Detector Prediction and Analysis

The ν_μ disappearance analysis, first, requires us to make a prediction for specific selected sample values of oscillation parameters Δm^2_{32} and θ_{23} and second, requires us to compare these predicted samples with the real selected sample. A measurement of parameters is obtained from a method known as a likelihood fit. The simplest way to do this is to compare the FD prediction with data, however, significant flux and neutrino cross section uncertainties would result in not so great experimental sensitivity. The existence of the ND and its measurements of the neutrino energy spectrum greatly mitigate this aforementioned problem. A procedure, called extrapolation, helps to predict the FD neutrino spectrum based on ND measurements and is described in the current chapter.

9.1 Prediction

The predicted FD spectrum consists of ν_μ CC signal, beam background components, and cosmic background. The extrapolation procedure uses ND data only to predict ν_μ CC signal since it is a significant portion of the FD neutrino spectrum. Beam background components are taken directly from FD Monte Carlo and cosmic background is estimated based on data recorded outside the beam spill window of NuMI spill.
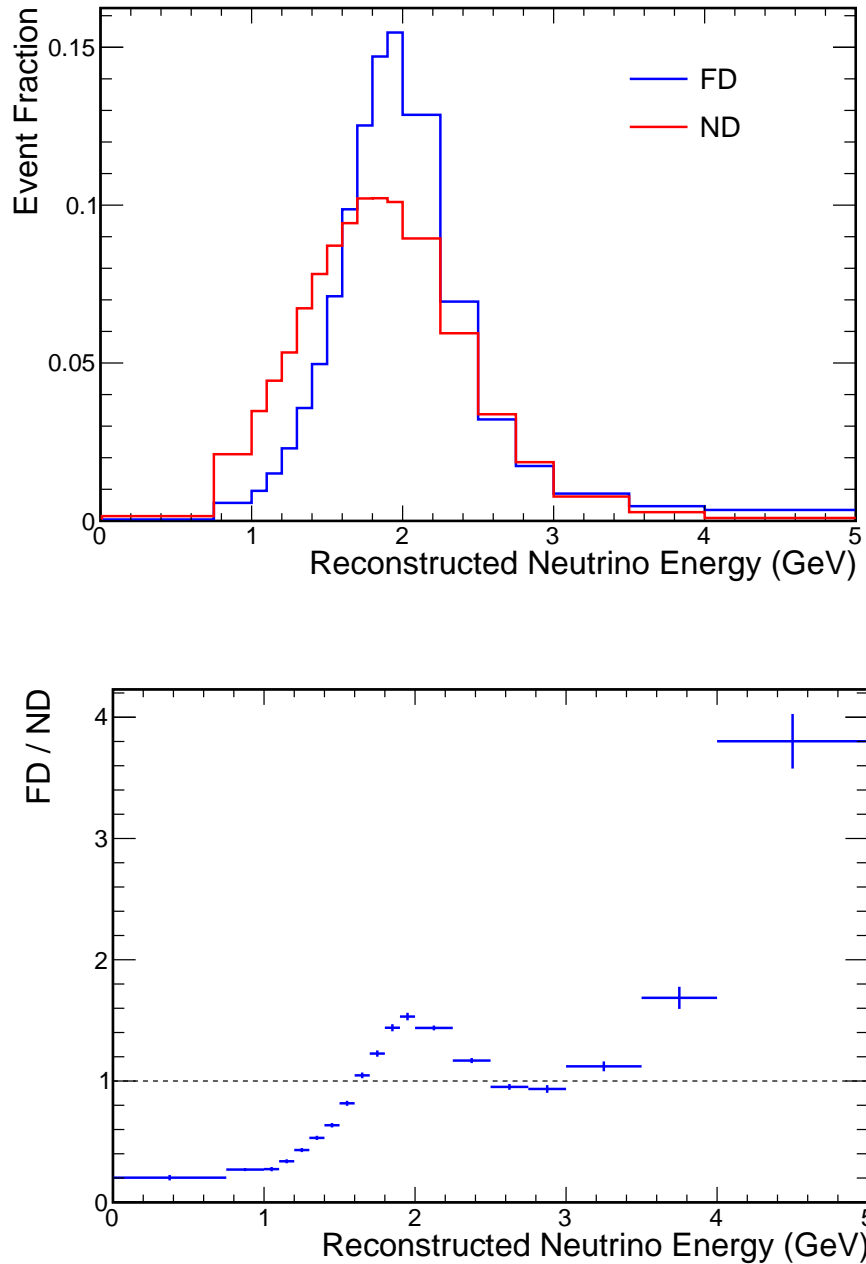
Figure 9.1: MC Prediction for the contained samples in ND and FD.
The first plot above illustrates the contained neutrino spectra in the Near Detector and the Far Detector. Both detectors observed neutrinos from the same source, however smaller ND size leads to a bigger fraction of low energy neutrinos and close position of ND to decay pipe also broaden observed neutrino spectrum. The second plot illustrates the shape of Far to Near ratio, however for the extrapolation procedure Far to Near ratio is used in bins of true energy. The actual extrapolation procedure is performed for four quantiles separately and spectra shapes are very similar to what is illustrated here.
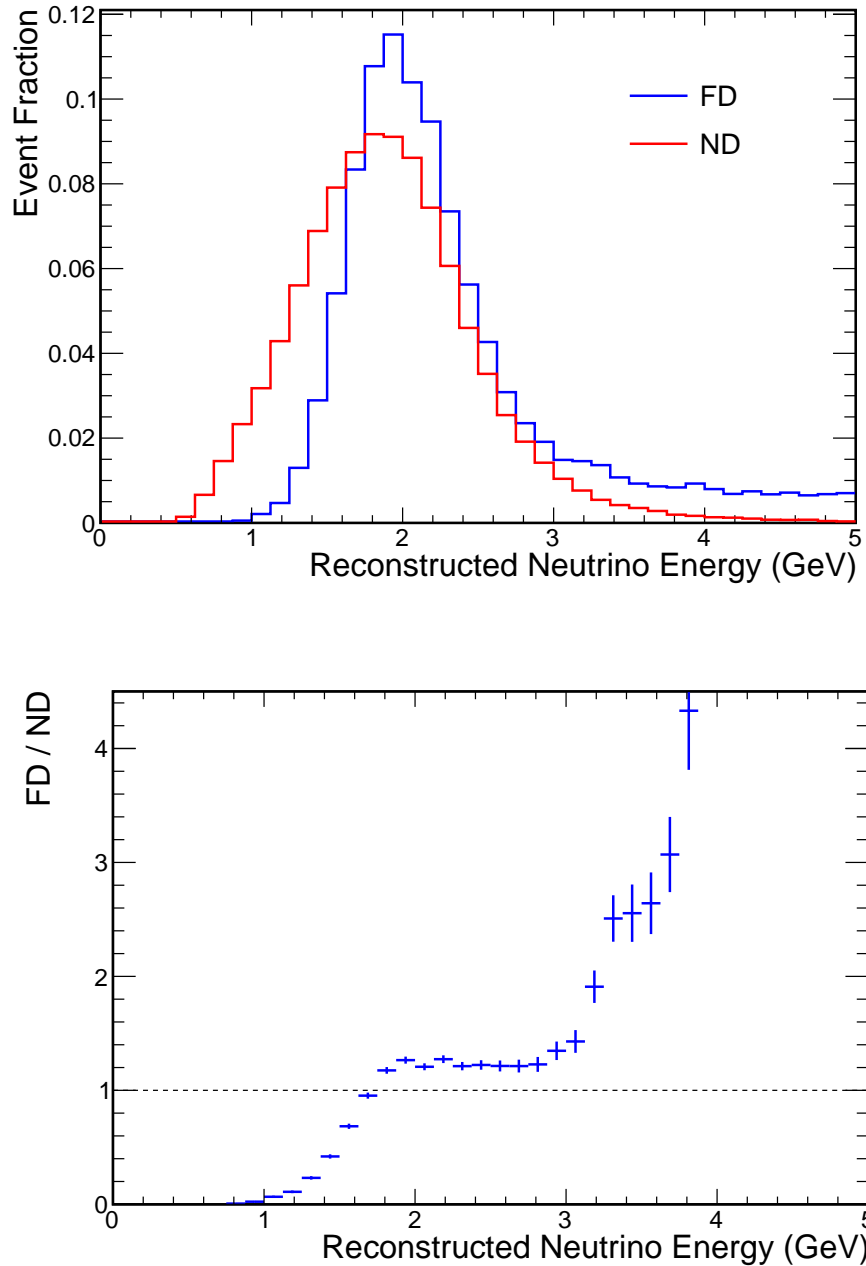
Figure 9.2: MC Prediction for the contained sample in ND and the escaping sample in FD.

The first plot above illustrates the contained neutrino spectrum in the Near Detector and the escaping spectrum in the Far Detector. Both detectors observed neutrinos from the same source, however smaller ND size leads to a bigger fraction of low energy neutrinos and close position of ND to decay pipe also broaden observed neutrino spectrum. The second plot illustrates the shape of Far to Near ratio, however for the extrapolation procedure Far to Near ratio is used in bins of true energy. To obtained prediction of escaping neutrino spectrum in the Far Detector contained Near Detector spectrum is used.
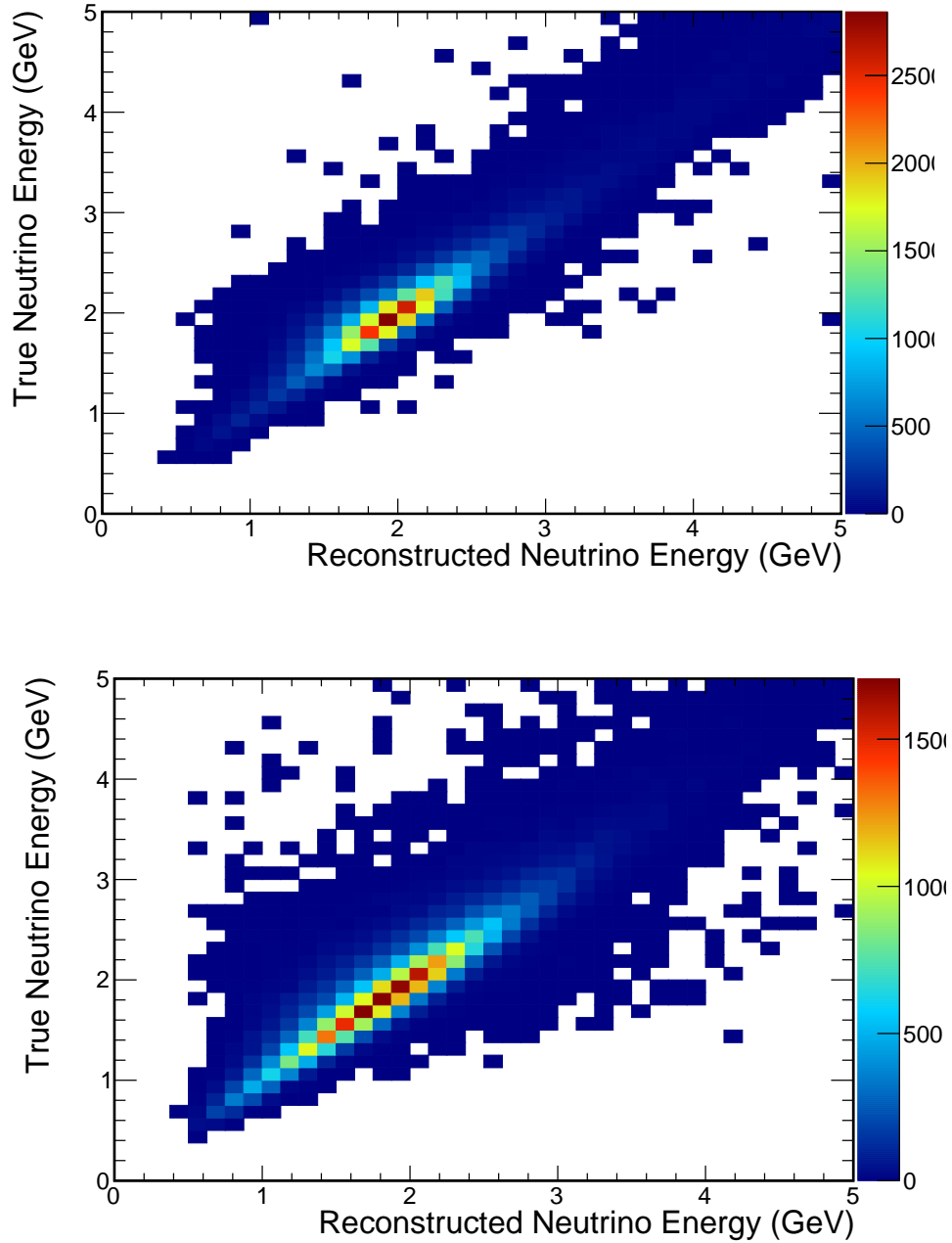
Figure 9.3: Reco-true matrices for FD and ND contained samples.
This is an example of reco-true matrices for FD (top) and ND (bottom) contained samples, matrices for the escaping sample looks similar. The matrices are used in extrapolation procedures to convert ND neutrino spectrum in reconstructed energy bins to spectrum in true energy bin and vice versa for FD neutrino spectrum.

9.1.1 Signal Extrapolation

Monte Carlo simulations for ND and FD are generated separately and under assumption of no neutrino oscillation. The shape of reconstructed neutrino spectra at different detectors is different largely due to the fact of different geometric effects and inconsistency in distortions caused by different resolutions of energy estimators at ND and FD. Figures 9.1 and 9.2 illustrate the overlay of neutrino spectra shapes for both detectors.

Being a small detector the ND cannot contain highly energetic neutrinos, thus its observed neutrino spectrum is based towards lower energy - smaller hadronic activity and shorter muon tracks. However, steel plates alternating with regular detectors planes at the end of ND help to contain more energetic muons, nevertheless the ND neutrino spectrum is limited by around 4 GeV. One more geometrical effect which plays a role in FD/ND spectra shape difference is that decay tube[1] is not seen as a point neutrino source. The ND catches neutrinos which was produced at a wider range of off-axis angles and therefore the ND sees a broader neutrino spectrum as compared to FD. All these effects are well model by NOvA simulations.

Distortions caused by different resolutions of energy estimators at the ND and the FD is also mitigated by the extrapolation procedure. For every detector a 2D histogram of reconstructed energy vs. true energy is created. These *reco-true matrices* are used to convert bins of reconstructed energy at each detector to bins of true energy. Figure 9.3 illustrates these matrices.

The full extrapolation procedure works as follows. Firstly, an observed ND neutrino spectrum in bins of reconstructed energy is converted to the spectrum in bins of true energy with the help reco-true matrix. Secondly, geometric effect is mitigated by multiplying result of previous step with FD/ND true energy ratio to get FD unoscillated prediction in bins of true energy. Thirdly, every bin of the spectrum is reweighed with oscillated probability. Finally, FD reco-true matrix is applied to convert neutrino spectrum in bin of true energy back to spectrum in bins of reconstructed energy, thus result is the predicted FD neutrino spectrum based on the observed neutrinos at the ND. Figure 9.4 illustrates steps of the extrapolation procedure.

---

[1]Place where pions decay into neutrinos and other particles
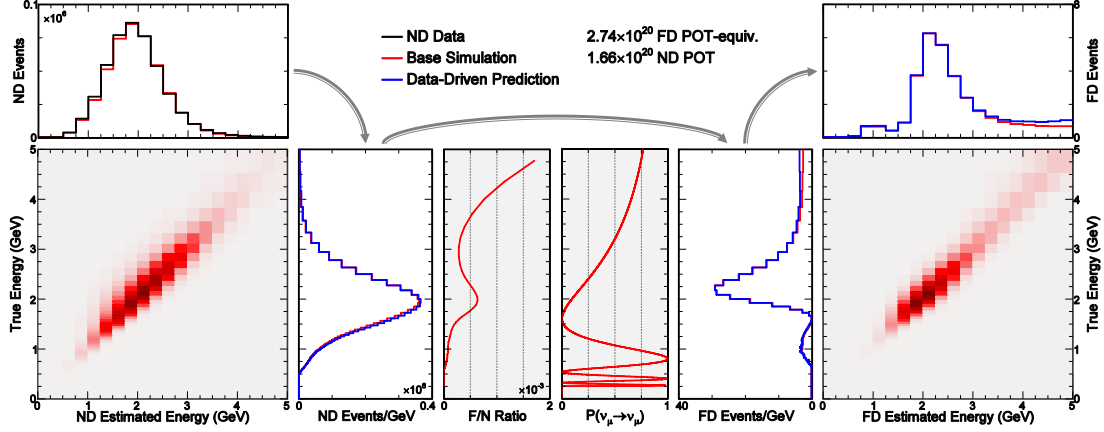
Figure 9.4: Extrapolation procedure schematic.
To obtain a correct prediction of neutrino spectrum at the FD based on the observed neutrino spectrum at the ND, 4 steps are needed. 1. Convert the ND spectrum in bins of reconstructed energy to bins of true energy with the reco-true matrix. 2. Multiply by the FD/ND true energy ratio to account for a different geometric effects for the FD and the ND. 3. Reweigh every bin of the spectrum by the oscillation probability. 4. Convert spectrum in bins of true energy back to spectrum in bins of reconstructed energy.

9.1.2 Beam Background Prediction

As mentioned in the beginning of the section, only ν_μ CC signal[2] is passing through extrapolation procedure described in section 9.1.1. All beam induced background components, namely $\nu_e, \bar{\nu}_e, \nu_\tau, \bar{\nu}_\tau$ and NC, are small compare to signal and ND Monte Carlo is subtracted from observed neutrino spectrum before it gets extrapolated. Then the beam background from FD Monte Carlo is added back to predicted FD neutrino spectrum [54].

9.1.3 Cosmic Background Prediction

Since for every 12 μs of NuMI spill a wider window of 450 μs is recorded the same data files are used for the cosmic background estimation. All selected events outside of NuMI

---

[2]Signal consists of two channels: $\nu_\mu \to \nu_\mu$ and $\bar{\nu}_\mu \to \bar{\nu}_\mu$.

spill window are normalized by scale factor

$$\text{scale} = \frac{12\mu s}{450\mu s - 12\mu s},\tag{9.1}$$

to estimate cosmic background inside the NuMI spill window. After that, this selected spectrum is added to the FD predicted neutrino spectrum.

9.2 Analysis

This section describes a procedure used for the measurement of oscillation parameters Δm_{32}^2 and $\sin^2 \theta_{23}$. The procedure is called a binned maximal-likelihood fitting.

9.2.1 4+1 Sample Fitting

The ND neutrino spectrum reweighed with the oscillation probability during the extrapolation procedure produces the FD predicted neutrino spectrum for those specific oscillation parameters. The analysis framework calculates the oscillation probability in the three-flavor neutrino formalism for different values of Δm_{32}^2 and $\sin^2 \theta_{23}$.

The final FD neutrino spectra predictions consists of five different spectra. Four spectra for FD contained events, these spectra have events with different reconstructed hadronic energy fraction, and one spectrum for escaping events. Contained spectra are extrapolated from 4 similar[3] ND contained spectra and escaping spectrum is extrapolated from one - all quantiles combined - ND contained spectrum.

When the predictions for specific oscillation parameters for the five spectra are ready and real FD data is gathered, the following log-likelihood for the Poisson distributed data function is used

$$\chi^2 = \sum_{s \in \{\text{cont, esc}\}} \left[2 \sum_i n_{s,i} - o_{s,i} + o_{s,i} \ln \left(\frac{o_{s,i}}{n_{s,i}} \right) \right].\tag{9.2}$$

The outer sum is summation over four contained samples and one escaping sample, for each sample inner summation is over bins i, $n_{s,i}$ is the number of predicted events for bin i and sample s, and $o_{s,i}$ is the number of observed events for bin i and sample

---

[3]ND data before the extrapolation procedure is also spilt into 4 quantiles.

s in FD data. The closer predicted spectra to observed ones the lower χ^2 function, thus maximum likelihood corresponds to a minimal χ^2. The log-likelihood function is calculated for different oscillation parameters and 2D surface of χ^2 vs Δm_{32}^2 and $\sin^2 \theta_{23}$ is formed. The minimum of the surface corresponds to the best fit point, confidence levels are drawn around best fit point on the plane of Δm_{32}^2 and $\sin^2 \theta_{23}$ based on the $\Delta \chi^2$ relative to the minimum value [1]. The values of $\Delta \chi^2$ for different confidence intervals in 1D and 2D cases are illustrated in Table 9.1.

C.L. (%)	1D	2D
68.3	1.00	2.30
90.0	2.71	4.61
95.4	4.00	6.18
99.7	9.00	11.83

Table 9.1: $\Delta \chi^2$ values for different dimensions and confidence levels.

In order to include systematic uncertainties in the current picture, one more term is added to the χ^2 function:

$$\chi^2 = \sum_{s \in \{\text{cont, esc}\}} \left[2 \sum_i n_{s,i} - o_{s,i} + o_{s,i} \ln\left(\frac{o_{s,i}}{n_{s,i}}\right) + \sum_j \frac{s_j^2}{\sigma_j^2} \right]. \tag{9.3}$$

The last term is the same for the five samples. The σ_j parameters describe our knowledge and understanding of the allowed shift in a particular systematic. The s_j parameters are evaluated during the process known as marginalization - for every set of oscillation parameters Δm_{32}^2 and $\sin^2 \theta_{23}$, the analysis software scans over different values of s_j trying to find the value which minimizes χ^2. This leads to a better fit and to a more gentle slope of χ^2 surface, as result confidence level contours gets bigger. Thus, the effect of systematic uncertainties makes the oscillation parameters measurements less certain as expected.

Chapter 10

Systematics

Precise measurements of the oscillation parameters depend on correct extrapolated predictions of neutrino spectrum at the Far Detector. In turn, extrapolated predictions depend on our understanding of all properties of the detectors as well as properties of particles propagation and interaction with other particles. Naturally, this understanding cannot be absolute which leads to uncertainties in the final result, these uncertainties are called systematic uncertainties, as opposed to statistical uncertainties which comes from the probabilistic nature of the high energy experiment. While statistical uncertainties are mitigated by longer exposure, systematic uncertainties could be mitigated by the experiment design. For example, the two-detector design of NOvA reduces the impact of flux and cross section uncertainties.

The first section of this chapter describes the treatment of systematic uncertainties in NOvA and the following ones discuss the impact of different systematic uncertainties on the extrapolated predictions.

10.1   Evaluation of Systematic Uncertainties

For some systematics, the analysis framework allows a reweightable approach to evaluate the impact of a specific systematic on the analysis result. This approach helps to reduce the computational resources [55]. For instance, any cross section parameter has its own uncertainty and for every simulated event a weight is calculated based on that uncertainty, and by reweighing events one gets a new (shifted) prediction which

corresponds to that cross section parameter. One gets 2 shifted predictions by using weights which are calculated for $\pm 1\sigma$ shifts for some cross section parameter; nominal and 2 shifted predictions are used to produced a systematic error band on all plots which are presented in this chapter. In this document, systematic error bands are shown only for escaping sample, the readers interested in the study of the systematic uncertainties for the contained sample are referred to [53].

The systematic effects which need to alter information on a hit-by-hit basis cannot be used in a reweightable scheme and a completely new set of Monte Carlo simulation files is generated. For instance, new sets of files are required for the systematically shifted scintillation model, calibration systematics etc.

During the fitting procedure the fitter needs to know the prediction for fractional systematic shifts. This is achieved by using a cubic spline interpolation between nominal, $\pm 1\sigma$ and $\pm 2\sigma$ shifts.

The analysis framework distinguishes between two types of systematic uncertainties in NOvA, those which are correlated for both detectors and those which are independent. Correlated systematic uncertainties shift the prediction in both detectors simultaneously by the same amount and are called *absolute* uncertainties. Flux and neutrino cross section uncertainties are examples of absolute uncertainties. Systematic effects which are independent across detectors are called *relative* uncertainties.

10.2 Cross Section Uncertainty

GENIE cross section models depends on 80+ parameters and uncertainties on all these parameters allow to calculate cross section weights [32]. When one alters some parameter the weight is determined as ratio of cross section with altered parameter to nominal one. Later, at analysis time, every selected event at the Near or the Far Detector is weighted with above calculated weight, thus the shifted prediction is generated. The marginalization process[1] is computationally heavy and only those GENIE cross section systematics are used which has significant impact on the analysis. Table 10.1 summarize cross section parameters used in the analysis, the first column is the parameter description and the second one is parameter's 1σ uncertainty.

---

[1]fitting procedure with systematic uncertainties taken into account.

In addition to GENIE parameters, the NOvA framework analysis uses a few more cross section effects to get a better agreement between ND data and simulations. The first effect is RPA[2] corrections, data from MINERvA [56] strongly support the need for a correction to reactions at low momentum transfer for QE and RES reactions. Corrections were needed to accommodate the effect of "weak charge screening" and they were computed based on RPA. Both corrections and uncertainties are momentum transfer dependent except for RPA RES uncertainty which is taken at 100% (means that effect is switched off) [57]. The second effect is MEC, neutrino scattering on a pair of nucleons [3], which depends on neutrino energy and the fraction of np pairs. Different models give different behavior for the MEC cross section at low energies. Since MEC is constraint by normalizing to the data the most important part of cross section uncertainty is the shape. Ratio of different normalized models to the empirical GENIE MEC model lies inside the region bounded by two functions given in table 10.2, where "+" and "-" correspond to $+1\sigma$ and -1σ shift respectively. Another important effect of the MEC interaction is 4-momentum transfer. The simulation is fit to the data by applying weights in $(q_0, |\vec{q}|)$-plane and uncertainty to the fit tends to make things more QE-like or RES-like, these shifts are achieved by varying other the combination of uncertainties that distorts the visible hadronic energy distribution [58].

Figures 10.1, 10.2, 10.3, 10.4, 10.5, 10.6 illustrate effect of GENIE parameters on selected escaping signal and background events. Those parameters are chosen to be shown here as they have a noticeable impact on FD predictions while the rest of the cross section parameters have a much smaller effect.

---

[2]Random Phase Approximation

[3]neutron-proton pair (np), proton-proton pair (pp).

Description	Uncertainty
Axial mass for CC quasi-elastic neutrino production	$\pm 5\%$
Axial mass for CC resonance neutrino production	$\pm 20\%$
Axial mass for NC resonance neutrino production	$\pm 20\%$
Vector mass for CC resonance neutrino production	$\pm 10\%$
CCQE Pauli suppression (via changes in Fermi level k_F)	$\pm 35\%$
CC coherent neutrino production, normalization	$\pm 20\%$
NC coherent neutrino production, normalization	$\pm 20\%$
Nucleon elastic reaction probability	$\pm 30\%$
Nucleon charge exchange probability	$\pm 50\%$
Nucleon absorption probability	$\pm 20\%$
Nucleon inelastic reaction probability	$\pm 40\%$
Hadron formation zone	$\pm 50\%$
DIS neutrino on neutron CC 1 pion production	$\pm 50\%$
DIS neutrino on neutron CC 2 pions production	$\pm 50\%$

Table 10.1: GENIE parameters and their uncertainties used in the analysis.

Description	Uncertainty
RPA effect in resonance neutrino production	q^2 dependent
RPA enhancement effect in CC QE	q^2 dependent
RPA suppression effect in CC QE	q^2 dependent
MEC initial state np fraction	0.7...0.9
MEC cross section energy dependence	$\pm\frac{1}{1+2.5E_{\nu_\mu}}$
MEC momentum transfer shape	q^2 dependent

Table 10.2: RPA and MEC uncertainties used in the analysis.

(a) FD MC Background Prediction   (b) FD MC Signal Prediction
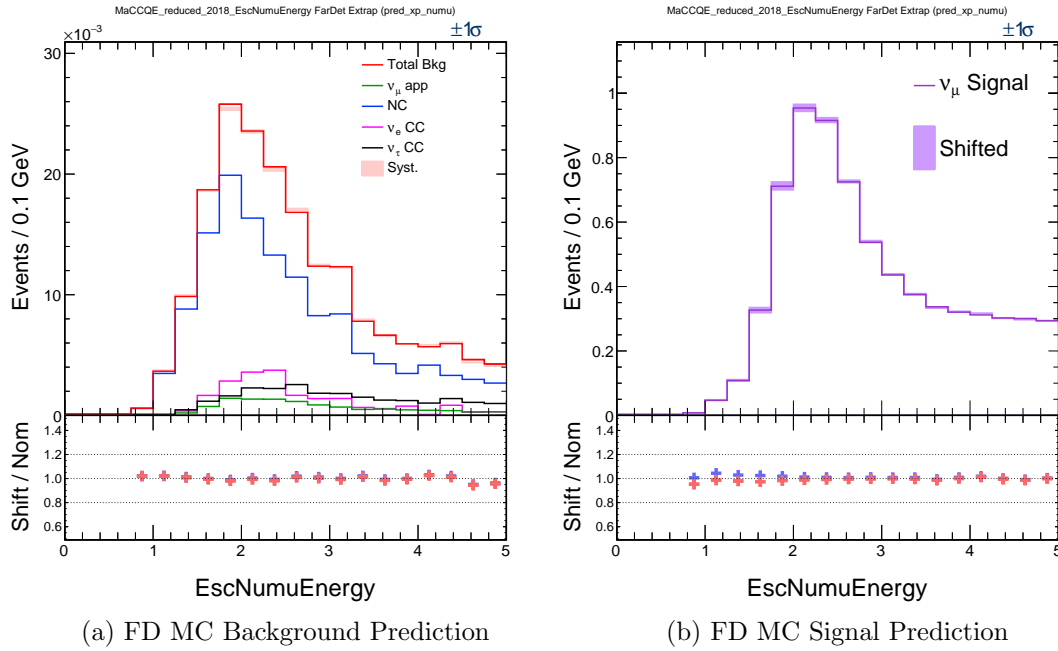
Figure 10.1: Systematic effect of MaCCQE uncertainty

Integral shift	Nominal	Shift (+)	Shift (-)	% Diff. (+)	% Diff. (-)
ν_μ signal	18	17	18	-0.7	+1.0
Tot beam bkg	0.46	0.46	0.46	-0.6	+0.3
NC	0.33	0.33	0.33	-0.1	-0.1
ν_μ App	0.027	0.026	0.027	-1.6	+1.6
ν_e CC	0.051	0.051	0.051	+0.0	+0.0
ν_τ CC	0.056	0.055	0.058	-2.1	+2.7

Table 10.3: Systematic effect of MaCCQE uncertainty on FD MC signal and background prediction
The "Nominal" column shows the number of selected events when the GENIE parameter is at its central value.The "Shift ($\pm$)" columns show the number of selected events when the GENIE parameter is shifted by 1σ up or down correspondingly. The "Diff ($\pm$)" columns show the same shifts in a relative manner.

(a) FD MC Background Prediction   (b) FD MC Signal Prediction
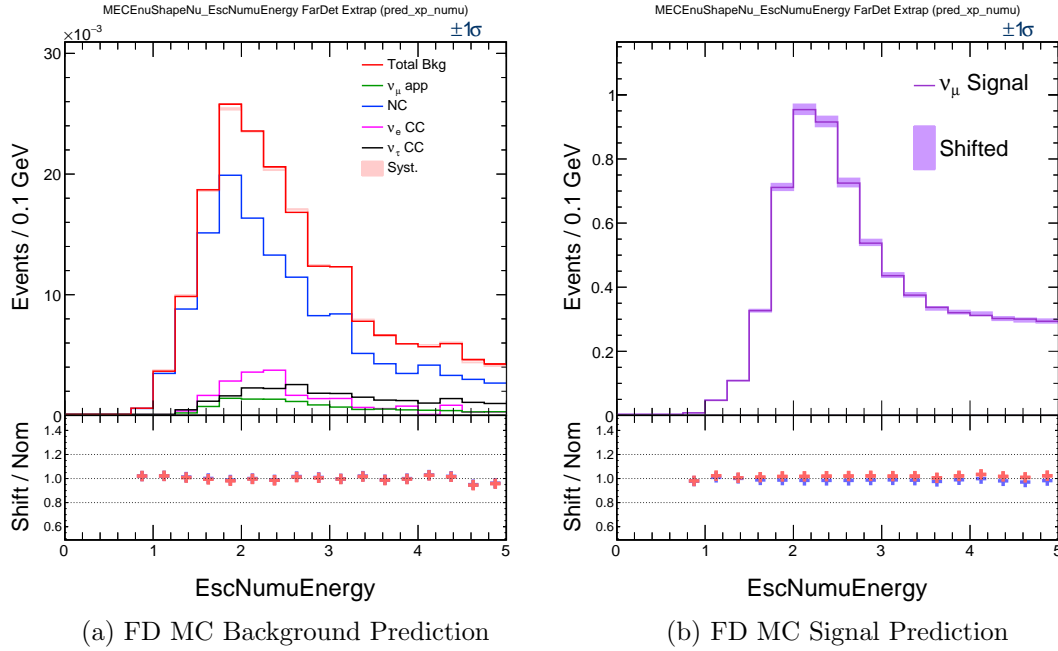
Figure 10.2: Systematic effect of MECEnuShapeNu uncertainty

Integral shift	Nominal	Shift (+)	Shift (-)	% Diff. (+)	% Diff. (-)
ν_μ signal	18	18	17	+1.8	-1.4
Tot beam bkg	0.46	0.46	0.46	-0.4	+0.0
NC	0.33	0.33	0.33	-0.1	-0.1
ν_μ App	0.027	0.026	0.027	-1.6	+1.6
ν_e CC	0.051	0.051	0.051	+0.0	+0.0
ν_τ CC	0.056	0.056	0.057	-0.6	+1.1

Table 10.4: Systematic effect of MECEnuShape uncertainty on FD MC signal and background prediction

The "Nominal" column shows the number of selected events when the GENIE parameter is at its central value. The "Shift ($\pm$)" columns show the number of selected events when the GENIE parameter is shifted by 1σ up or down correspondingly. The "Diff ($\pm$)" columns show the same shifts in a relative manner.

(a) FD MC Background Prediction   (b) FD MC Signal Prediction
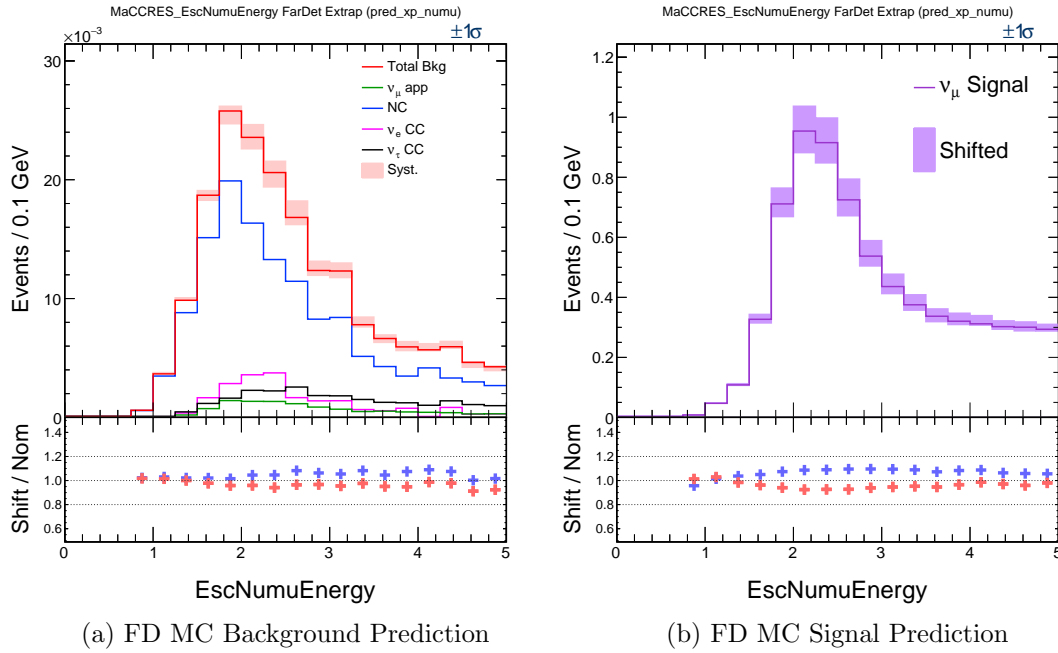
Figure 10.3: Systematic effect of MaCCRES uncertainty

Integral shift	Nominal	Shift (+)	Shift (-)	% Diff. (+)	% Diff. (-)
ν_μ signal	18	17	19	-5.4	+8.1
Tot beam bkg	0.46	0.45	0.48	-3.7	+4.5
NC	0.33	0.33	0.33	-0.1	-0.1
ν_μ App	0.027	0.024	0.031	-11.9	+13.9
ν_e CC	0.051	0.051	0.051	+0.0	+0.0
ν_τ CC	0.056	0.048	0.068	-14.1	+21.3

Table 10.5: Systematic effect of MaCCRES uncertainty on FD MC signal and background prediction

The "Nominal" column shows the number of selected events when the GENIE parameter is at its central value. The "Shift ($\pm$)" columns show the number of selected events when the GENIE parameter is shifted by 1σ up or down correspondingly. The "Diff ($\pm$)" columns show the same shifts in a relative manner.

(a) FD MC Background Prediction

(b) FD MC Signal Prediction
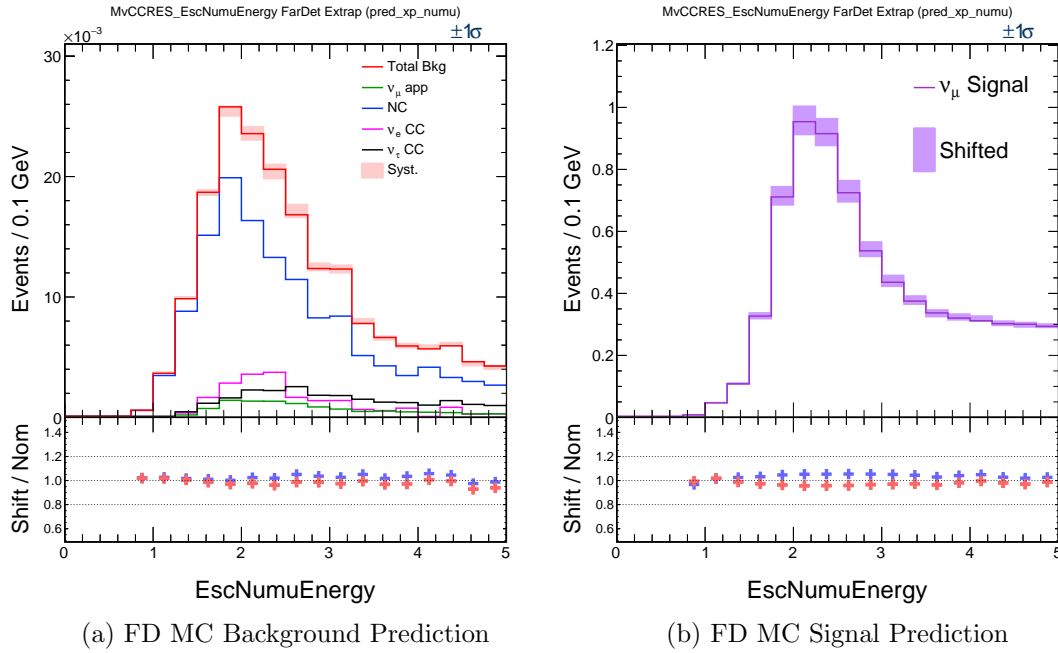
Figure 10.4: Systematic effect of MvCCRES uncertainty

Integral shift	Nominal	Shift (+)	Shift (-)	% Diff. (+)	% Diff. (-)
ν_μ signal	18	17	18	-3.2	+4.4
Tot beam bkg	0.46	0.45	0.47	-2.1	+2.3
NC	0.33	0.33	0.33	-0.1	-0.1
ν_μ App	0.027	0.025	0.029	-6.3	+7.6
ν_e CC	0.051	0.051	0.051	+0.0	+0.0
ν_τ CC	0.056	0.052	0.062	-7.5	+10.8

Table 10.6: Systematic effect of MvCCRES uncertainty on FD MC signal and background prediction

The "Nominal" column shows the number of selected events when the GENIE parameter is at its central value. The "Shift (±)" columns show the number of selected events when the GENIE parameter is shifted by 1σ up or down correspondingly. The "Diff (±)" columns show the same shifts in a relative manner.

(a) FD MC Background Prediction (b) FD MC Signal Prediction

Figure 10.5: Systematic effect of CCQEPauliSupViaKF uncertainty

Integral shift	Nominal	Shift (+)	Shift (-)	% Diff. (+)	% Diff. (-)
ν_μ signal	18	17	18	-1.2	+1.3
Tot beam bkg	0.46	0.46	0.46	-0.2	-0.2
NC	0.33	0.33	0.33	-0.0	-0.0
ν_μ App	0.027	0.027	0.027	-0.7	-0.7
ν_e CC	0.051	0.051	0.051	+0.0	+0.0
ν_τ CC	0.056	0.056	0.056	+0.0	-0.0

Table 10.7: Systematic effect of CCQEPauliSupViaKF uncertainty on FD MC signal and background prediction

The "Nominal" column shows the number of selected events when the GENIE parameter is at its central value. The "Shift (±)" columns show the number of selected events when the GENIE parameter is shifted by 1σ up or down correspondingly. The "Diff (±)" columns show the same shifts in a relative manner.

(a) FD MC Background Prediction   (b) FD MC Signal Prediction
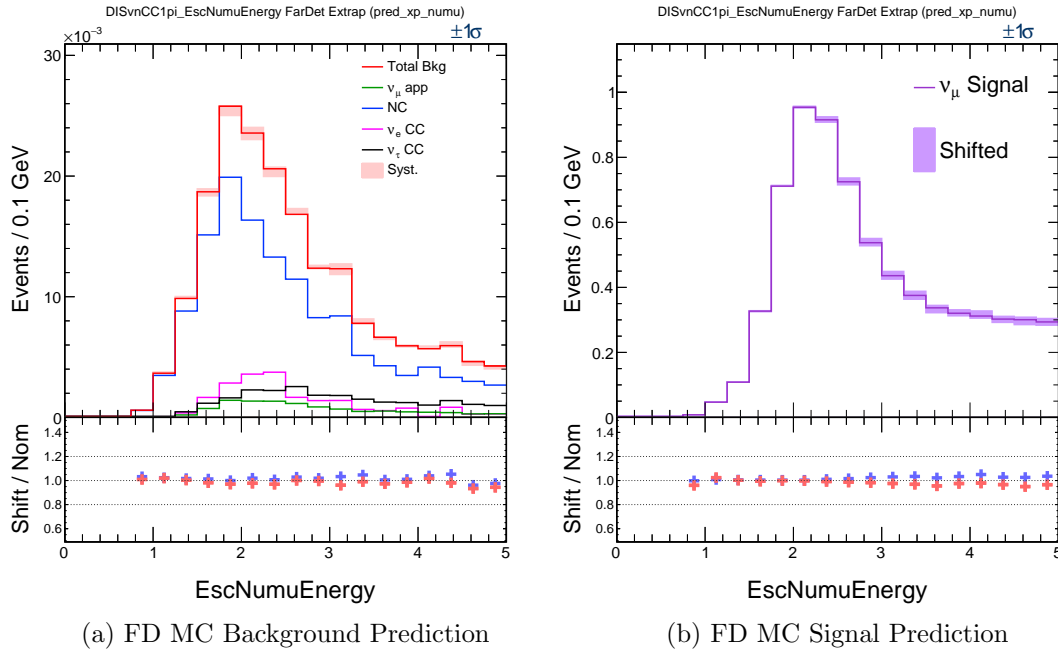
Figure 10.6: Systematic effect of DISvnCC1pi uncertainty

Integral shift	Nominal	Shift (+)	Shift (-)	% Diff. (+)	% Diff. (-)
ν_μ signal	18	17	18	-1.2	+1.3
Tot beam bkg	0.46	0.46	0.46	-0.2	-0.2
NC	0.33	0.33	0.33	-0.0	-0.0
ν_μ App	0.027	0.027	0.027	-0.7	-0.7
ν_e CC	0.051	0.051	0.051	+0.0	+0.0
ν_τ CC	0.056	0.056	0.056	+0.0	-0.0

Table 10.8: Systematic effect of DISvnCC1pi uncertainty on FD MC signal and background prediction
The "Nominal" column shows the number of selected events when the GENIE parameter is at its central value. The "Shift (±)" columns show the number of selected events when the GENIE parameter is shifted by 1σ up or down correspondingly. The "Diff (±)" columns show the same shifts in a relative manner.
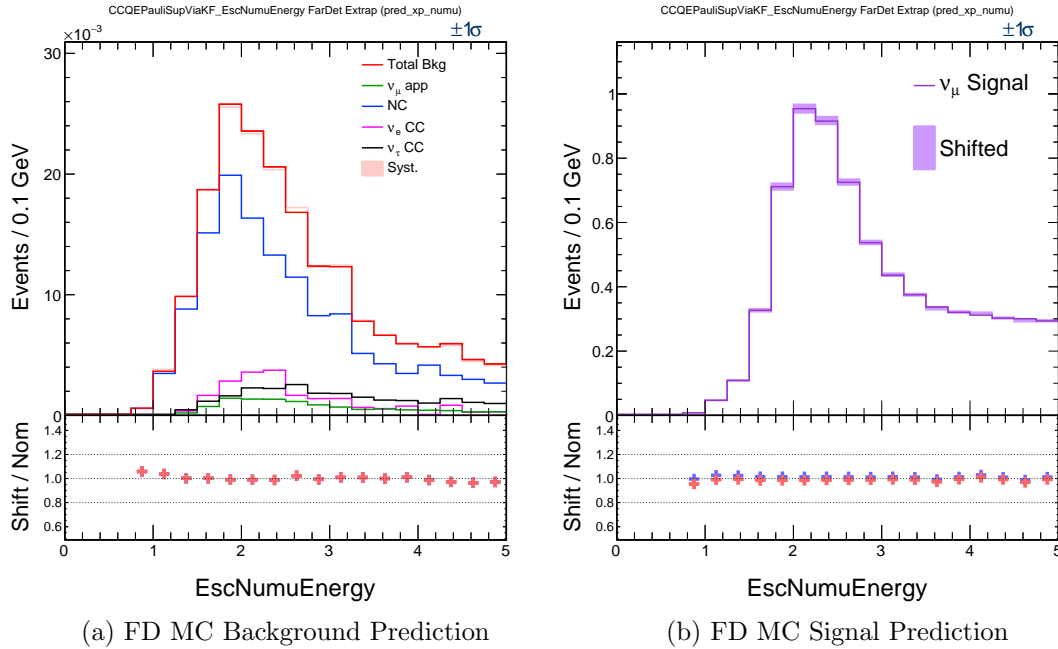
10.3   Flux Uncertainty

In order to estimate the neutrino flux through the Near and the Far detectors the NuMI beam is simulated through the entire production process that starts with protons hitting the target and ends with pions, muons and kaons decaying in the decay pipe. And systematic uncertainties of all these processes have to be evaluated.

Flux uncertainties could be separated into two categories

- **Hadron production**. Uncertainties on cross section of proton interaction in the NuMI target.

- **Beam transport**. Uncertainties on target facility components:

  - Horn current, 5% uncertainty

  - Horn 1 and Horn 2 positions in both transverse dimensions, ± 2 mm uncertainties

  - Beam position on target, ± 0.5 mm uncertainty

  - Beam spot size on target, ± 0.2 mm uncertainty

  - Target position in longitudinal direction, ± 2 mm uncertainty

It turns out that flux uncertainties are heavily correlated across almost all neutrino true energy bins. To correctly treat this, 2000 predictions were generated in different flux universes where the parameters described above have different values within their uncertainty limits, [59]. A correlation matrix is constructed based on the flux histograms from the different universes and after that a Principal Component Analysis (PCA) is carried out to disentangle the correlations. It is shown in [59] that only the first 5 or 8 PCA components are enough to explain most of the information contained in the correlation matrix i.e. first several PCA components describes all flux uncertainties.

As mentioned previously the two detectors and the extrapolation procedure help to reduce flux systematics significantly. Figure 10.7 shows the third PCA component that has the biggest impact on the Far detector prediction.

(a) FD MC Background Prediction   (b) FD MC Signal Prediction
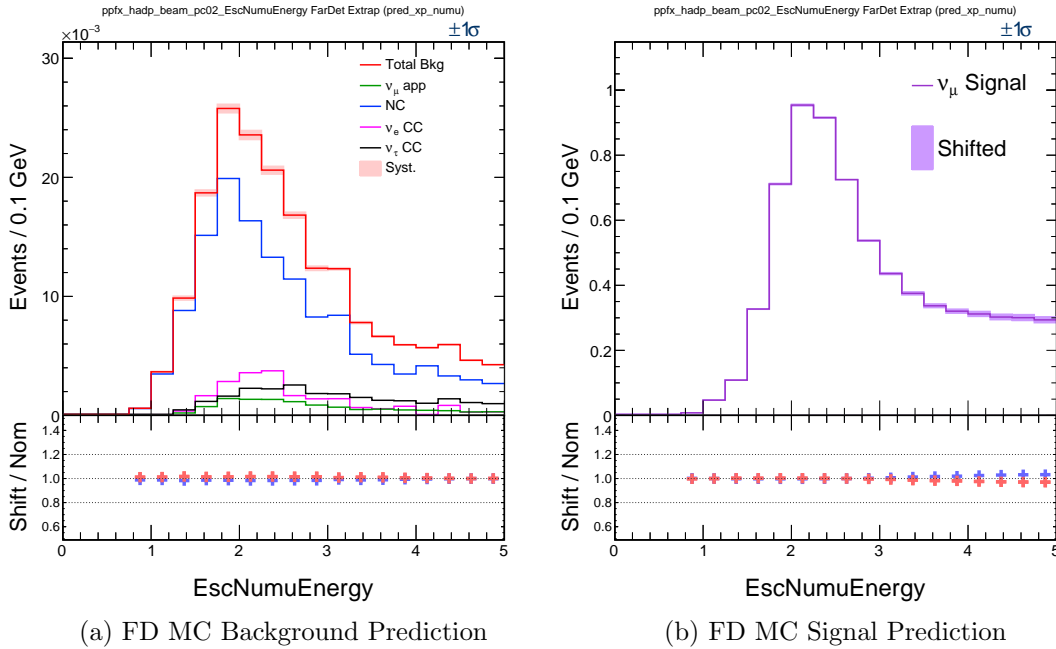
Figure 10.7: Systematic effect of 3rd flux PCA component.

Integral shift	Nominal	Shift (+)	Shift (-)	% Diff. (+)	% Diff. (-)
ν_μ signal	18	17	18	-0.7	+0.7
Tot beam bkg	0.46	0.47	0.46	+1.2	-1.3
NC	0.33	0.33	0.32	+1.3	-1.4
ν_μ App	0.027	0.027	0.027	-0.5	+0.5
ν_e CC	0.051	0.051	0.051	+0.0	+0.0
ν_τ CC	0.056	0.057	0.055	+1.4	-1.6

Table 10.9: Systematic effect of 3rd flux PCA component on FD MC signal and background prediction

The "Nominal" column shows the number of selected events when flux parameters are at its central value. The "Shift ($\pm$)" columns show the number of selected events when the third flux PCA component is shifted by 1σ up or down correspondingly. The "Diff ($\pm$)" columns show the same shifts in a relative manner.

10.4 Muon Energy Uncertainty

Due to some uncertainties in detectors masses, compositions, offsets etc. the observed range traveled by muon has its own uncertainty. Muon track length is used to estimate the muon energy at the Near detector and Far detector (for the contained sample) and is important part of energy estimator for escaping sample at the Far Detector. A very extensive study was carried out in [60] and the following absolute and relative systematic uncertainties were established:

- **Absolute**:

  - muon track length in active region of the Near and Far detectors, 0.94%
  - muon track length in muon catcher at the Near detector, 0.69%

- **Relative**:

  - muon track length in active region of the Near and Far detectors, 0.27%
  - muon track length in muon catcher at the Near detector, 0.75%

Figures 10.8 and 10.9 illustrate the impact of the absolute and relative systematic uncertainties on the escaping sample prediction at the Far detector correspondingly.

(a) FD MC Background Prediction　　　(b) FD MC Signal Prediction
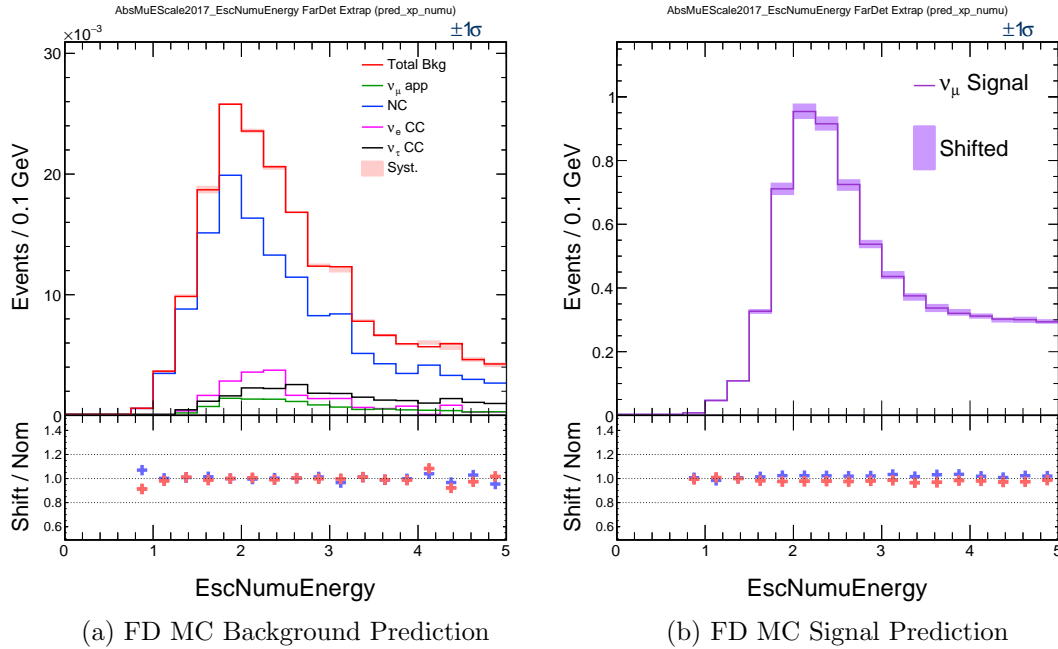
Figure 10.8: Systematic effect of absolute muon energy uncertainty

Integral shift	Nominal	Shift (+)	Shift (-)	% Diff. (+)	% Diff. (-)
ν_μ signal	18	17	18	-2.2	+2.2
Tot beam bkg	0.46	0.46	0.46	-0.2	+0.1
NC	0.33	0.33	0.33	-0.2	+0.0
ν_μ App	0.027	0.027	0.027	-0.4	+0.3
ν_e CC	0.051	0.051	0.051	+0.0	+0.0
ν_τ CC	0.056	0.056	0.056	-0.6	+0.4

Table 10.10: Systematic effect of absolute muon energy uncertainty on FD MC signal and background prediction

The "Nominal" column shows the number of selected events when the nominal simulation is used. The "Shift (±)" columns show the number of selected events when muon track length is shifted by 1σ up or down correspondingly. The "Diff (±)" columns show the same shifts in a relative manner.

(a) FD MC Background Prediction

(b) FD MC Signal Prediction
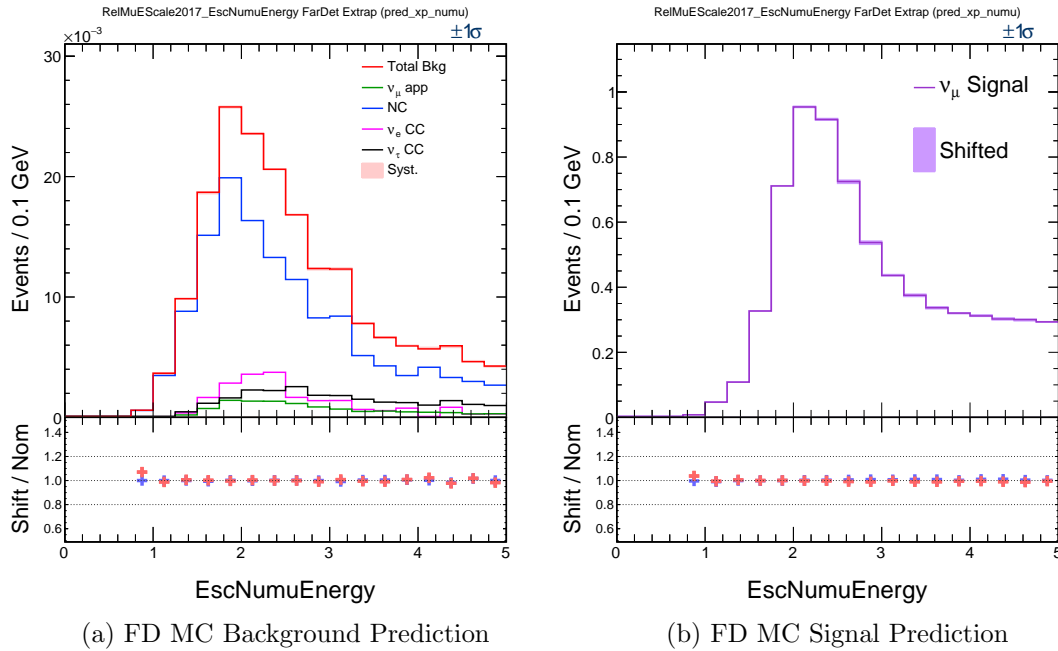
Figure 10.9: Systematic effect of relative muon energy uncertainty

Integral shift	Nominal	Shift (+)	Shift (-)	% Diff. (+)	% Diff. (-)
ν_μ signal	18	17	18	-0.5	+0.4
Tot beam bkg	0.46	0.46	0.46	+0.0	-0.0
NC	0.33	0.33	0.33	+0.0	+0.0
ν_μ App	0.027	0.027	0.027	+0.1	-0.1
ν_e CC	0.051	0.051	0.051	+0.0	+0.0
ν_τ CC	0.056	0.056	0.056	+0.0	-0.1

Table 10.11: Systematic effect of relative muon energy uncertainty on FD MC signal
and background prediction

The "Nominal" column shows the number of selected events when the nominal simula-
tion is used. The "Shift ($\pm$)" columns show the number of selected events when muon
track length is shifted by 1σ up or down correspondingly. The "Diff ($\pm$)" columns show
the same shifts in a relative manner.

10.5   Calorimetric Energy Uncertainties

Several studies of the post calibration calorimetric response of the detectors show that the protons in the Near detector have the biggest discrepancy between data and simulations [61]. It is found that the calorimetric detector response in data is 5% lower than the simulation and this discrepancy is interpreted as a 5% absolute calibration uncertainty. In order to evaluate an impact of this uncertainty a new simulation is generated and a different calibration is applied before the reconstruction step. As result, every slice has the same number of hits but their energies are shifted up or down. Figure 10.10 illustrates the impact of absolute calibration uncertainty.

While comparison of simulated muons to data can be done in both detectors (simulation/data comparison in the Near detector and simulation/cosmic comparison in the Far detector) however for protons it could be done only in the Near detector. Thus, the same 5% effect is assumed as the worst case for a relative effect. Figure 10.11 illustrates the impact of the relative calibration uncertainty on selected escaping sample at the Far detector.

In addition to the average cell response an individual detector cell has a different response for an energy deposition at different distances from the readout electronics. A comparison of the reconstructed and true energy of simulated cosmic hits as function of their position along the cell is performed in [62] and the discrepancy is interpreted as calibration 'shape' uncertainty. The effect of this systematic is illustrated in figure 10.12.
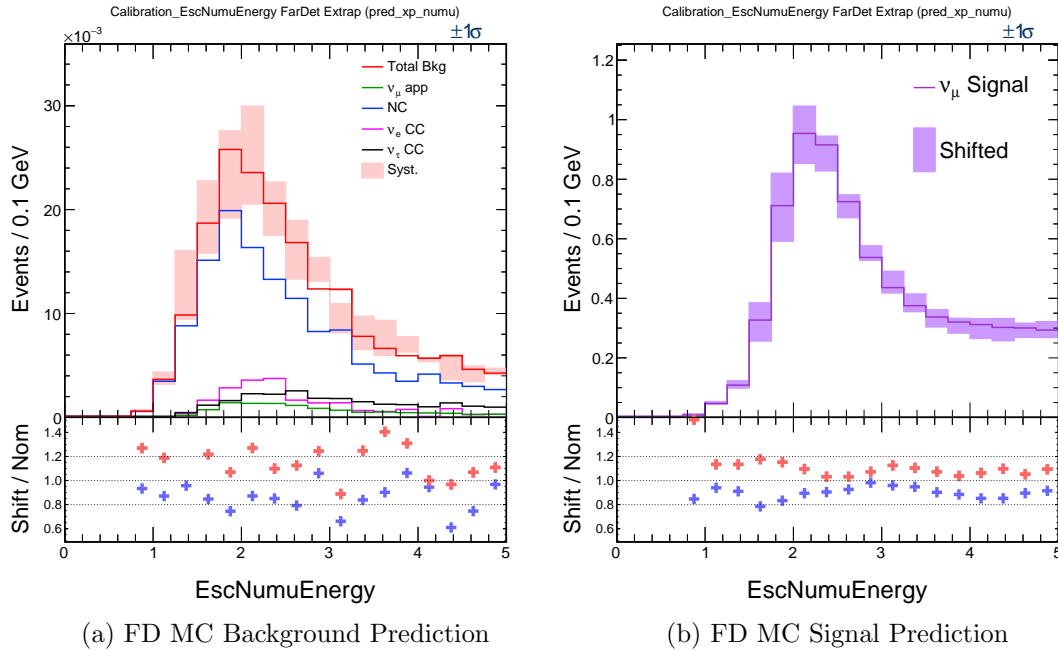
(a) FD MC Background Prediction

(b) FD MC Signal Prediction

Figure 10.10: Systematic effect of absolute calibration uncertainty

Integral shift	Nominal	Shift (+)	Shift (-)	% Diff. (+)	% Diff. (-)
ν_μ signal	18	19	16	+8.5	-10.1
Tot beam bkg	0.46	0.54	0.39	+17.4	-15.6
NC	0.33	0.41	0.29	+23.5	-13.2
ν_μ App	0.027	0.026	0.023	-2.0	-12.9
ν_e CC	0.051	0.051	0.051	+0.0	+0.0
ν_τ CC	0.056	0.057	0.048	+2.1	-14.9

Table 10.12: Systematic effect of absolute calibration uncertainty on FD MC signal and background prediction

The "Nominal" column shows the number of selected events when the nominal simulation is used. The "Shift (±)" columns show the number of selected events when calibration shifted samples are used. The "Diff (±)" columns show the same shifts in a relative manner.

(a) FD MC Background Prediction

(b) FD MC Signal Prediction
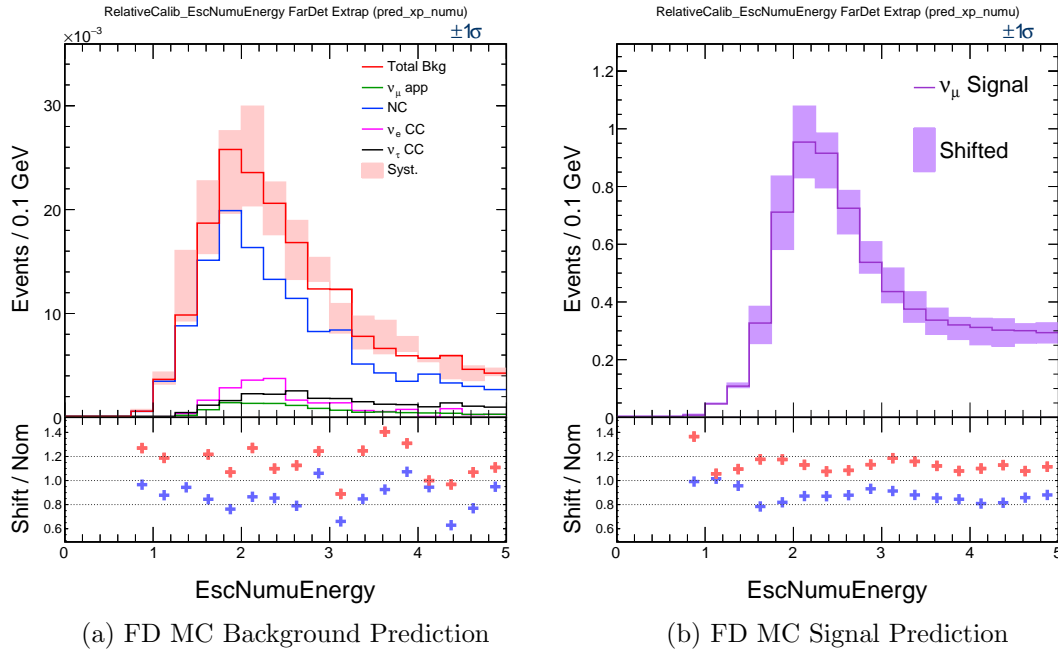
Figure 10.11: Systematic effect of relative muon energy uncertainty

Integral shift	Nominal	Shift (+)	Shift (-)	% Diff. (+)	% Diff. (-)
ν_μ signal	18	20	15	+12.2	-13.5
Tot beam bkg	0.46	0.54	0.39	+17.4	-15.3
NC	0.33	0.41	0.29	+23.5	-13.0
ν_μ App	0.027	0.026	0.023	-2.0	-12.8
ν_e CC	0.051	0.051	0.051	+0.0	+0.0
ν_τ CC	0.056	0.057	0.048	+2.1	-14.3

Table 10.13: Systematic effect of relative calibration uncertainty on FD MC signal and background prediction

The "Nominal" column shows the number of selected events when the nominal simulation is used. The "Shift (±)" columns show the number of selected events when calibration shifted samples are used. The "Diff (±)" columns show the same shifts in a relative manner.

(a) FD MC Background Prediction

(b) FD MC Signal Prediction
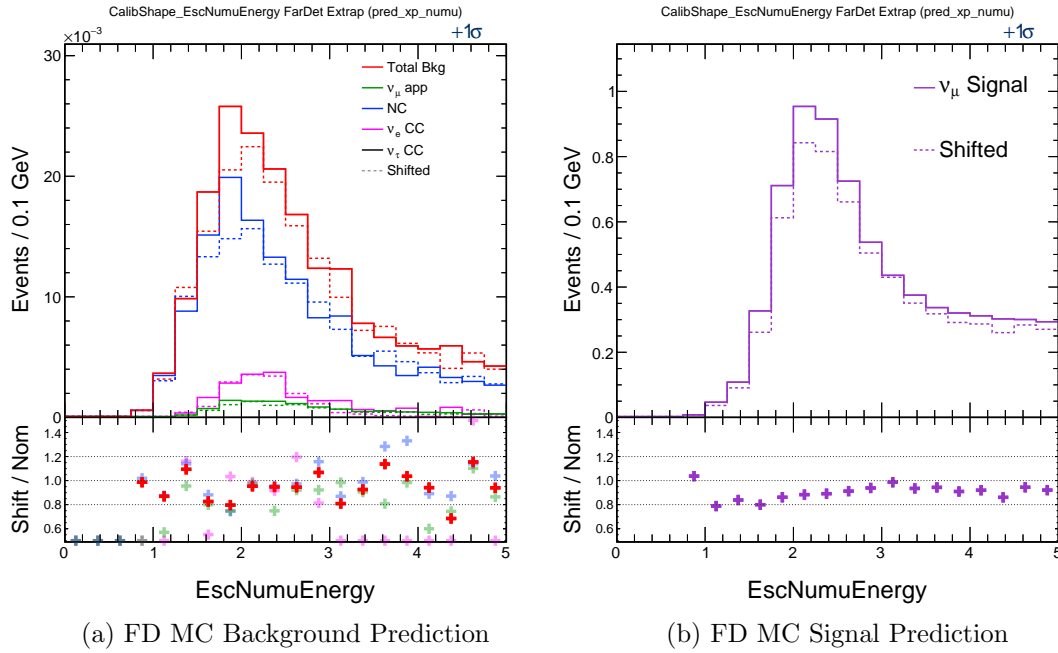
Figure 10.12: Systematic effect of 'shape' calibration uncertainty

Integral shift	Nominal	Shift (+)	Shift (-)	% Diff. (+)	% Diff. (-)
ν_μ signal	17.524	15.811	–	-9.8	–
Tot beam bkg	0.463	0.428	–	-7.5	–
ν_e CC	0.051	0.040	–	-20.2	–
NC	0.329	0.315	–	-4.2	–
ν_μApp	0.027	0.023	–	-14.2	–
ν_τ CC	0.056	0.049	–	-12.5	–

Table 10.14: Systematic effect of 'shape' calibration uncertainty on FD MC signal and background prediction
The "Nominal" column shows the number of selected events when the nominal simulation is used. The "Shift ($\pm$)" columns show the number of selected events when calibration shifted sample is used. The "Diff ($\pm$)" columns show the same shifts in a relative manner.

10.6 Light Model

To estimate the uncertainty on the light model, three special datasets are generated. The first dataset which is called nominal is generated with increased Cerenkov light collection efficiency and reduced standard scintillation light production, effectively removing the $\frac{dE}{dx}$ discrepancy observed in the ratio of ND data/simulation for muons and protons [63]. The second and the third datasets are $\pm 1\sigma$ shifts where alternative scintillator light levels are shifted by 10% up and down while the calibration is simultaneously adjusted by 10% in the opposite direction. The effect of the shifts is that some hits fall below or rise above the readout threshold.

In comparison to contained sample, the light model systematic has a significant effect on escaping sample[4]. The main reason is that escaping events have a significant fraction of hits which are close to the detector's edges. Those hits which happened at the back end of the cells have a bigger chance to have an incorrect attenuation meaning that the hits are very sensitive to the light model. As result, $\pm 1\sigma$ shifts could significantly affect those hits thereby making an event pass or fail preselection criterion in 7.2.4. Figure 10.13 illustrates the effect of light model systematic on selected escaping sample.

---

[4]a small effect of light model systematic for contained sample could be seen on page 613 of [64]
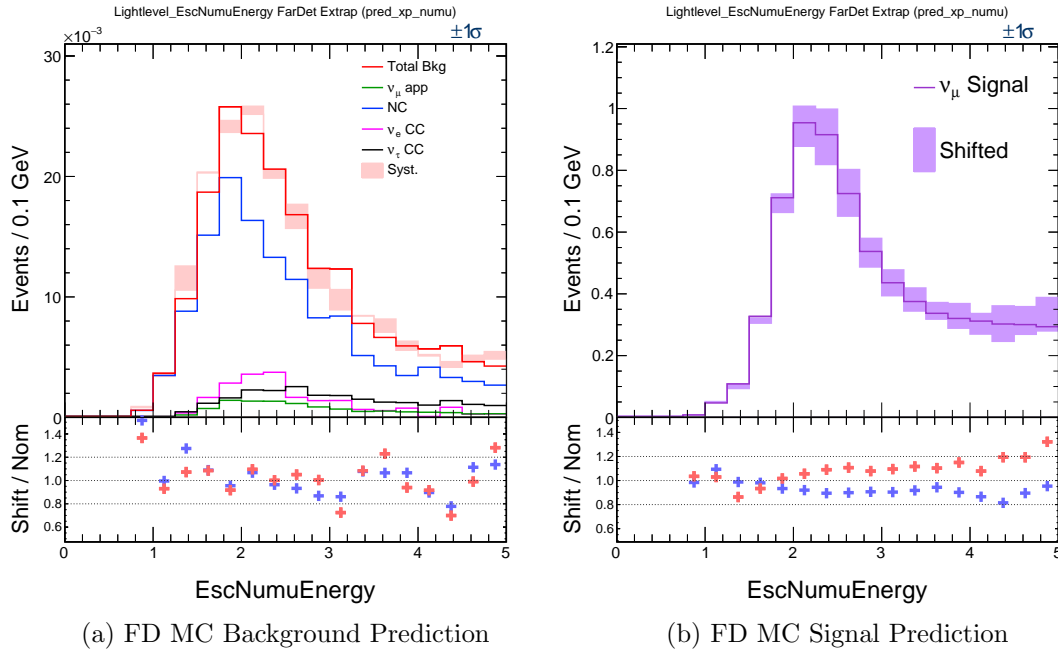
(a) FD MC Background Prediction

(b) FD MC Signal Prediction

Figure 10.13: Systematic effect of light model uncertainty

Integral shift	Nominal	Shift (+)	Shift (-)	% Diff. (+)	% Diff. (-)
ν_μ signal	18	19	16	+9.1	-8.7
Tot beam bkg	0.46	0.46	0.46	+0.4	+0.3
NC	0.33	0.33	0.34	+0.8	+3.1
ν_μ App	0.027	0.027	0.025	+0.4	-6.7
ν_e CC	0.051	0.051	0.051	+0.0	+0.0
ν_τ CC	0.056	0.059	0.049	+5.0	-13.3

Table 10.15: Systematic effect of light model uncertainty on FD MC signal and background prediction
The "Nominal" column shows the number of selected events when the nominal simulation is used. The "Shift (±)" columns show the number of selected events when light level shifted samples are used. The "Diff (±)" columns show the same shifts in a relative manner.

Chapter 11

Results

After analysing the Far Detector data, 126 events were selected for the 4 contained samples, including an expected background of 5.8 misidentified cosmic rays and 3.4 misidentified neutrino events of other types. For the escaping sample, 30 events were selected, including an expected background of 6.0 misidentified cosmic rays and 0.4 misidentified neutrino of other types. The resulting 5 spectra were fit simultaneously with the best-fit parameters are $\sin^2 \theta_{23} = 0.504$ and $|\Delta m^2_{32}| = 2.45 \times 10^{-3} eV^2$.
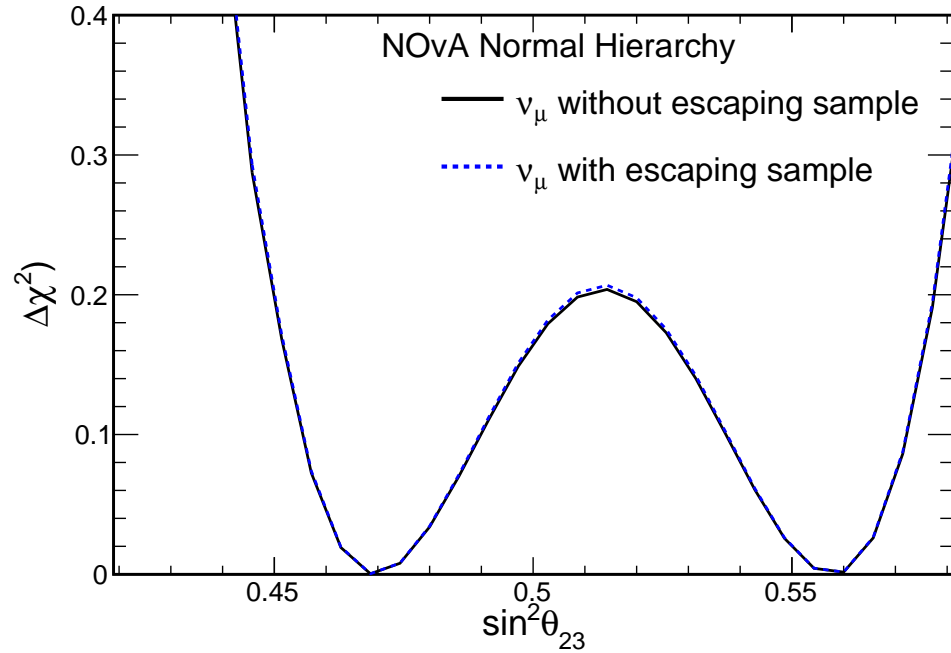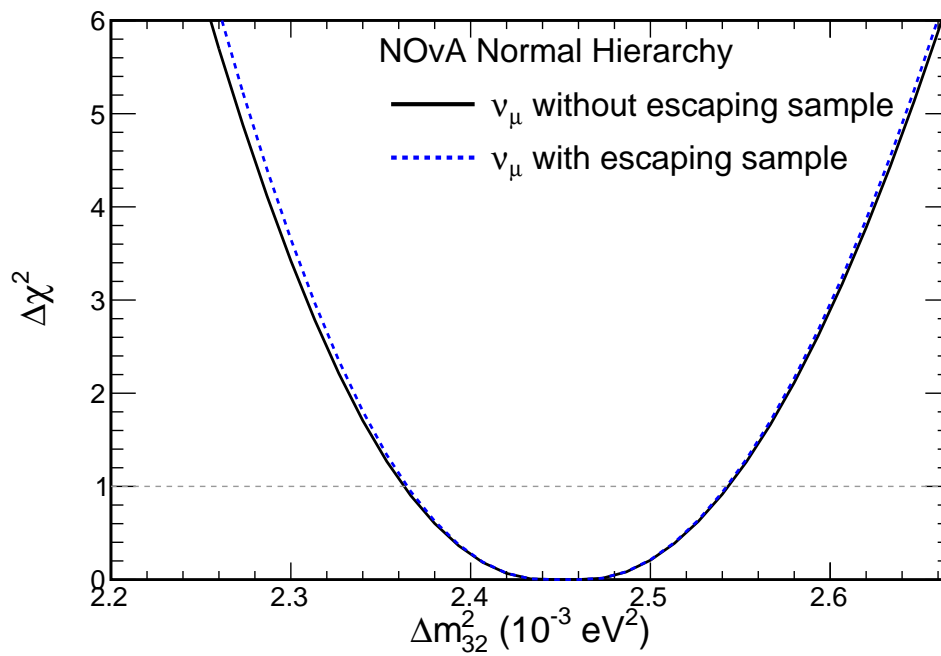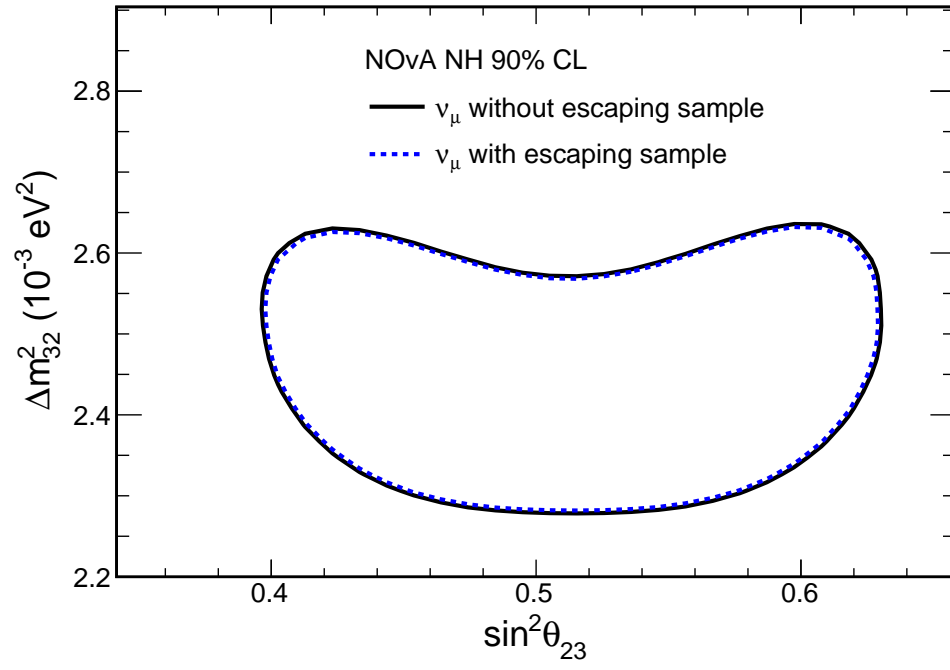
11.1 Predicted Contours

Before the real data is used to make final sensitivity contours, it is important to see predicted sensitivity contours to understand how much power the escaping sample provides to the experiment. To generate the predicted contours and profile functions for $\sin^2 \theta_{23}$ and Δm^2_{32}, simulation of the signal[1] was used to generate a fake data. Figures 11.1a, 11.1b and 11.2 illustrate profile functions and sensitivity contours respectively. Expected improvement is marginal.

11.2 Event Displays of Several Selected Escaping Events
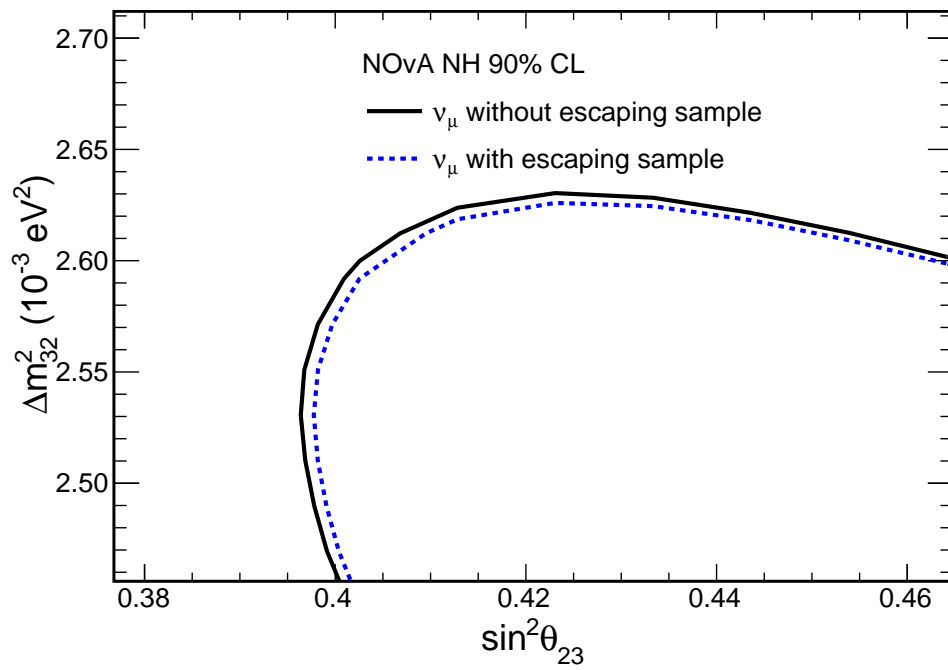
Figures 11.3, 11.4 and 11.5 give the examples of selected escaping events at the Far Detector.

---

[1]2017 best fit was used as seed oscillation parameters

(a) $\Delta\chi^2$ functions for $\sin^2\theta_{23}$ 1D fit

(b) $\Delta\chi^2$ functions for Δm^2_{32} 1D fit

Figure 11.1: $\Delta\chi^2$ functions for $\sin^2\theta_{23}$ and Δm^2_{32} 1D fit

(a) Unzoomed

(b) Zoomed

Figure 11.2: Predicted contours without and with escaping sample

Figure 11.3: Selected FD escaping ν_μ CC candidate
(Rotated left) The X vs. Z and Y vs. Z views of selected FD escaping ν_μ CC
candidate with estimated muon neutrino energy of 2.54 GeV.

Figure 11.4: Selected FD escaping ν_μ CC candidate
(Rotated left) The X vs. Z and Y vs. Z views of selected FD escaping ν_μ CC
candidate with estimated muon neutrino energy of 2.78 GeV.
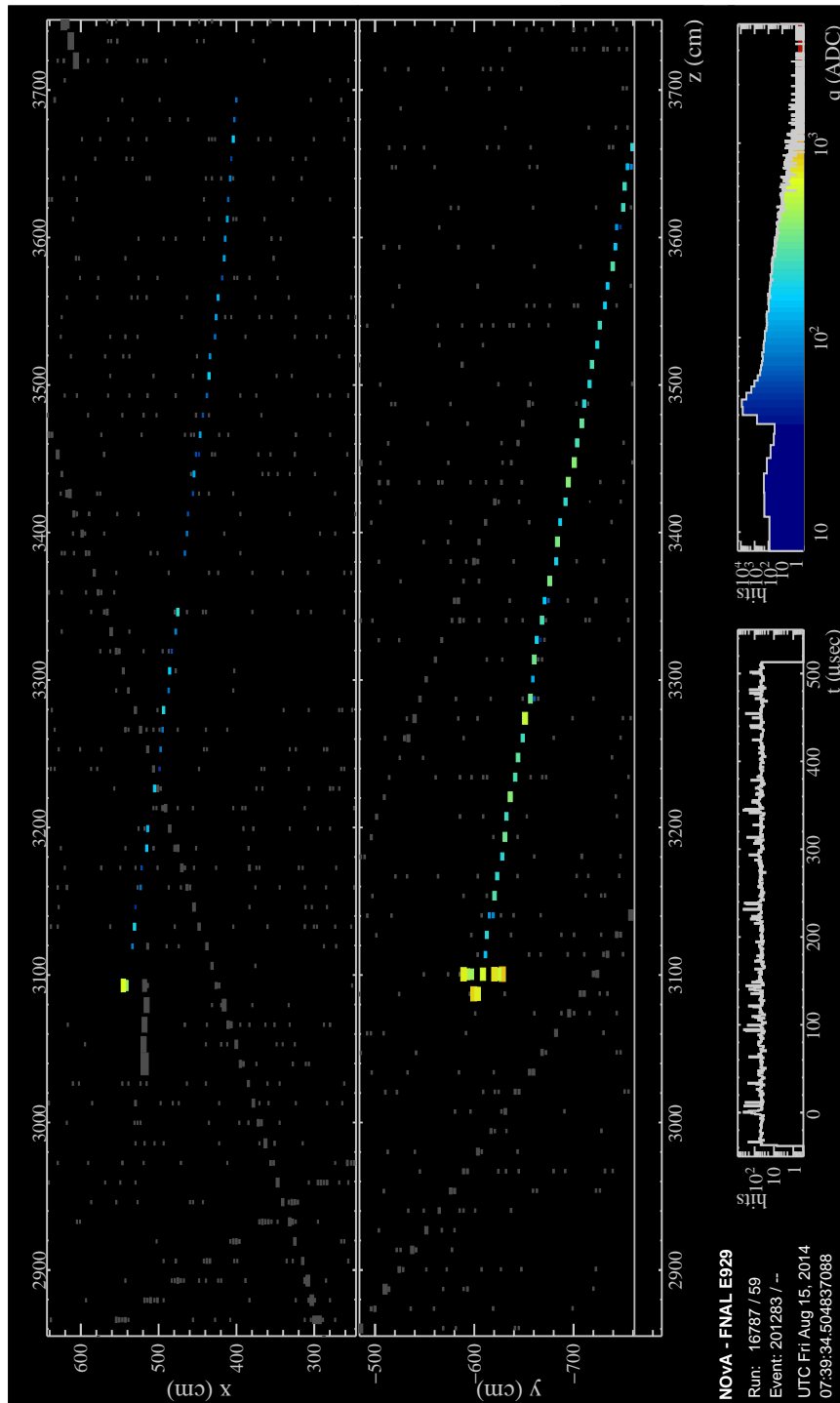
Figure 11.5: Selected FD escaping ν_μ CC candidate
(Rotated left) The X vs. Z and Y vs. Z views of selected FD escaping ν_μ CC
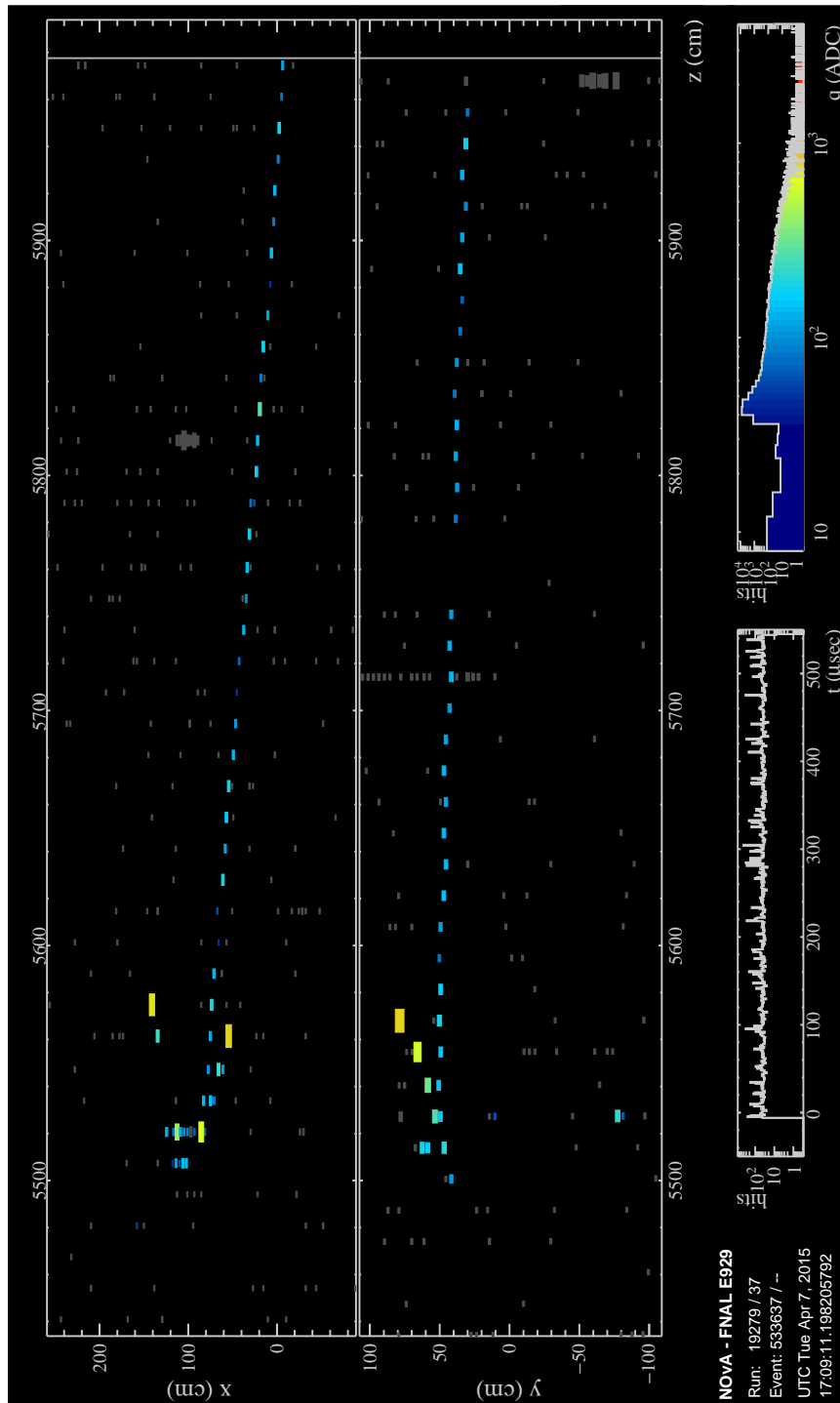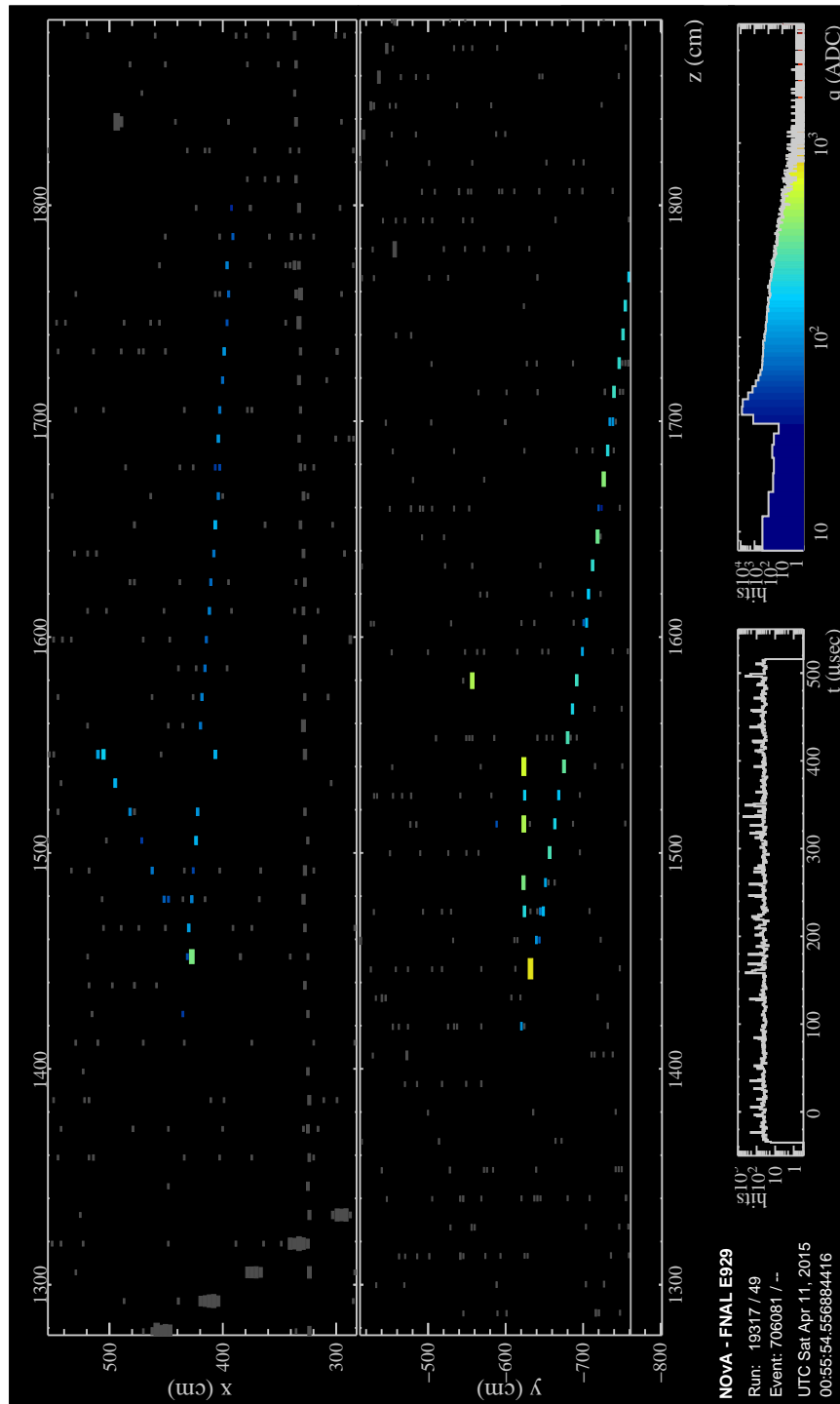candidate with estimated muon neutrino energy of 1.85 GeV.

11.3   Results of the Fit

The Far Detector data selected for all 5 spectra were fit to the extrapolated prediction. The fit included penalty terms to account for the systematic uncertainties according to equation 9.3. The figures 11.6 and 11.7 show overlaid Far Detector data with the predicted 1σ systematic uncertainty band for the four contained and one escaping spectra respectively.

Figure 11.8 illustrates 90% confidence levels of 5 samples fit with and without systematics effects included.
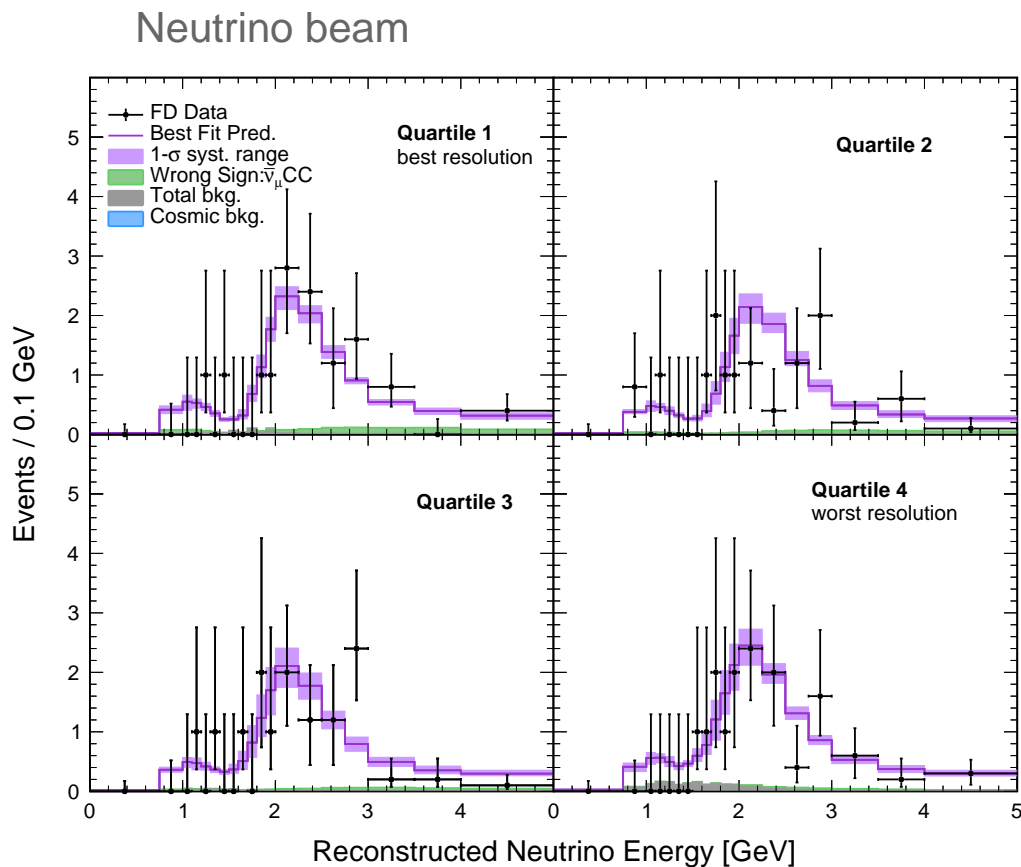
Figure 11.6: Observed 4 contained spectra at the Far Detector with best fit and systematics uncertainties

It is also interesting to compare if including the escaping sample is improving the
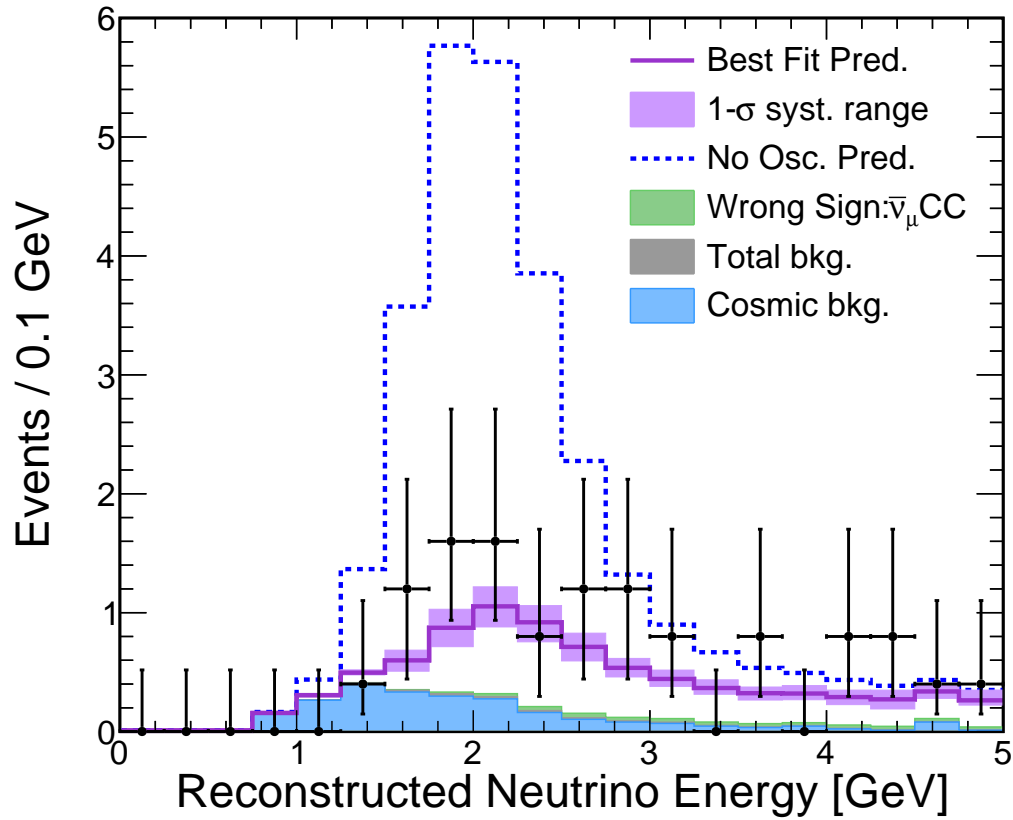
Figure 11.7: Observed escaping spectrum at the Far Detector with best fit and systematics uncertainties

Dashed line illustrates predicted escaping sample under assumption of no oscillation.

NOvA results when real data is used. Figure 11.9 illustrates the NOvA results with and without escaping sample in the fit.
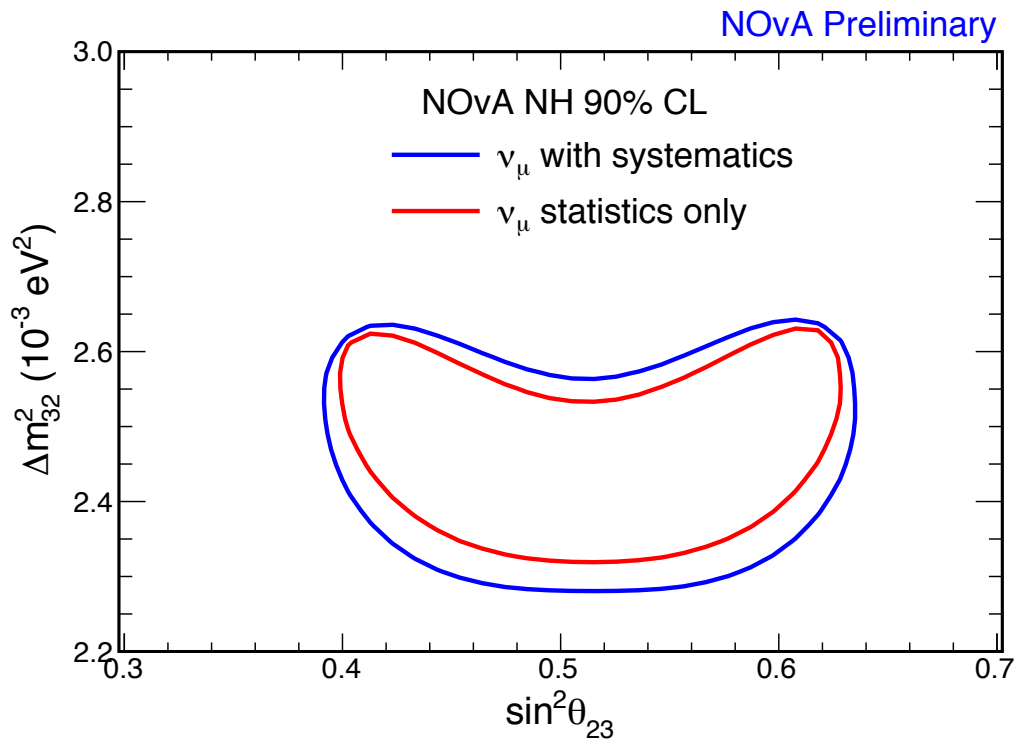
Figure 11.8: 90% confidence levels with and without systematic uncertainties Confidence level with systematic uncertainties is shown in blue and without systematics uncertainties is shown in red. The best-fit parameters are $\sin^2 \theta_{23} = 0.504$ and $|\Delta m^2_{32}| = 2.45 \times 10^{-3} eV^2$.

Figure 11.9: 90% confidence levels with and without escaping sample in the fit
Confidence level without escaping sample is shown in black and with escaping sample
is shown in blue. The best-fit parameters when escaping sample is included are
$\sin^2 \theta_{23} = 0.504$ and $|\Delta m_{32}^2| = 2.45 \times 10^{-3} eV^2$.

Chapter 12
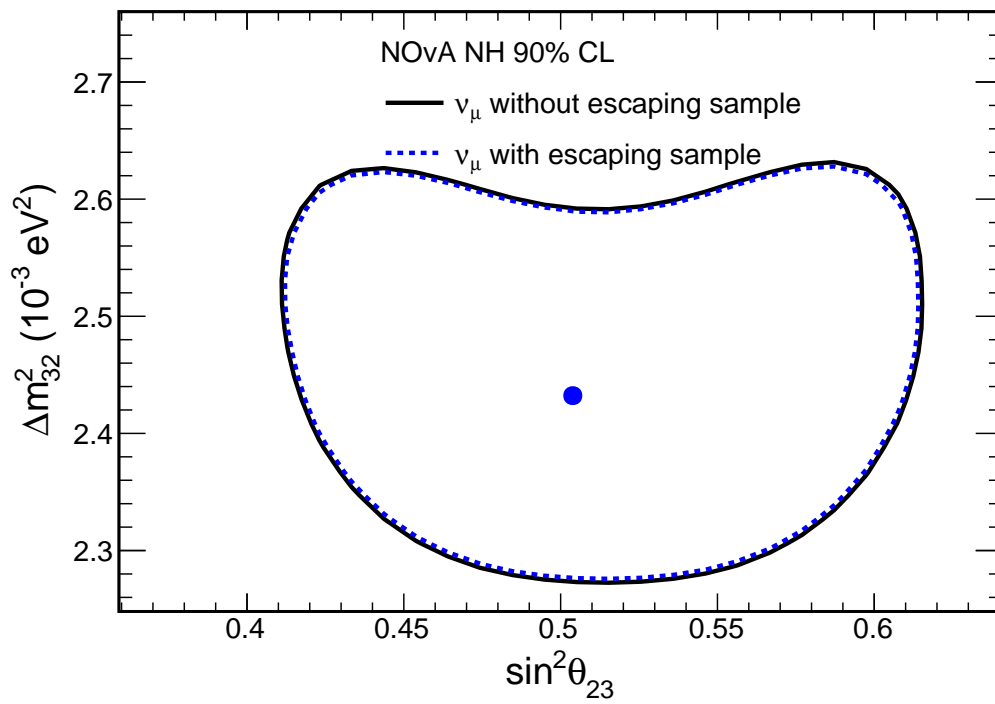
Conclusion

The data analyzed in the present work were taken between 2014 and 2017 in a neutrino mode. The results presented in the previous chapter prefer non-maximal mixing with best-fit oscillation parameters

$$\sin^2 \theta_{23} = 0.504^{+0.079}_{-0.060},$$

$$\Delta m^2_{32} = 2.45^{+0.11}_{-0.07} \times 10^{-3} \ eV^2.$$

The selection criteria to select the escaping sample developed in the present thesis allow to select events which were previously discarded by the analysis software. Despite the marginal improvements in measuring oscillation parameters using the escaping sample effectively adds **4%** more statistics.

The main difficulties with the escaping sample which are cosmic background and event energy estimation were addressed. And while energy estimation hardly could be improved more, there are still some space for potential improvements in cosmic background rejection. As it can be seen in figure 11.7 the most of cosmic background is in the region of 1-2 GeV where experiment is the most sensitive to oscillation parameters $\sin^2 \theta_{23}$ and Δm^2_{32}. One of the possible future lines of attack could be a usage of hit time information to determine the direction of the escaping track[1]. Another possibility could be a deep convolutional neural net, which was used in ν_μ disappearance and ν_e appearance analyses as well as in this thesis for contained sample, but trained primarily

---

[1]as of today timing resolution is not enough, however potentially it could be improved.

on escaping events.

NOvA experiment continues to take data in neutrino and antineutrino mode. Future improvements in analysis techniques, better understanding of systematics effects and more statistics will help us to understand neutrino sector in greater details and, perhaps, will bring more questions to study. Stay tuned!

References

[1] K. A. Olive et al. Review of Particle Physics. *Chin. Phys.*, C38:090001, 2014.

[2] R. Zwaska. *Accelerator systems and instrumentation for the NuMI neutrino beam.* PhD thesis, University of Texas, 2005.

[3] R. N. Mohapatra and G. Senjanovic. Neutrino mass and spontaneous parity non-conservation. *Phys. Rev. Lett.*, 44:912–915, 1980.

[4] K. S. Hirata et al. Observation of 8B solar neutrinos in the Kamiokande-II detector. *Phys. Rev. Lett.*, 63:16–19, 1989.

[5] John N. Bahcall. Two solar neutrino problems. *Phys. Lett.*, B338:276–281, 1994.

[6] F. P. An et al. Observation of electron-antineutrino disappearance at daya bay. *Phys. Rev. Lett.*, 108:171803, 2012.

[7] P. Adamson et al. First measurement of electron neutrino appearance in NOvA. *Phys. Rev. Lett.*, 116:151806, 2016.

[8] Mainz Collaboration. Final results from phase II of the Mainz neutrino mass search in tritium β decay. *The European Physical Journal C - Particles and Fields*, 40:447–468, 2005.

[9] T2K Collaboration. The T2K experiment. *Nuclear Instruments and Methods in Physics Research Section A: Accelerators, Spectrometers, Detectors and Associated Equipment*, 659:106 – 135, 2011.

[10] J. Chadwick. Intensitatsverteilung im magnetischen spektren der β-strahlen von radium b + c. *Verh. Dtsch. Phys. Ges.*, 16:383, 1914.

[11] W. Pauli. Open letter to the group of radioactive people at gauvereins meeting in tubingen, 1930.

[12] J. Chadwick. The existence of a neutron. *Royal Society of London Proceedings Series A*, 136:692, 1932.

[13] E. Fermi. Versuch einer theorie der β-strahlen. i. *Zeitschrift fur Physik*, 88:161, 1934.

[14] C. L. Cowan Jr., F. Reines, F. B. Harrison, H. W. Kruse, and A. D. McGuire. Detection of the free neutrino: A confirmation. *Science*, 124:103, 1956.

[15] G. Danby, J-M. Gaillard, K. Goulianos, L. M. Lederman, N. Mistry, M. Schwartz, and J. Steinberger. Observation of high-energy neutrino reactions and the existence of two kinds of neutrinos. *Phys. Rev. Lett.*, 9:36, 1962.

[16] G. Arnison et. al. (UA1 Collaboration). Experimental observation of isolated large transverse energy electrons with associated missing energy at $s = 540$ gev. *Physics Letters B*, 122:103, 1983.

[17] G. Arnison et. al. (UA1 Collaboration). Experimental observation of lepton pairs of invariant mass around 95 gev/c^2 at the cern sps collider. *Physics Letters B*, 126:398, 1983.

[18] D. DeCamp et. al. (ALEPH Collaboration). Determination of the number of light neutrino species. *Physics Letters B*, 231:519, 1989.

[19] M. L. Perl et. al. Evidence for anomalous lepton production in e^+e^- annihilation. *Physical Review Letters*, 35:22, 1975.

[20] K. Kodama et. al. (DONUT Collaboration). Observation of tau neutrino interactions. *Physics Letters B*, 504:218, 2001.

[21] B. Pontecorvo. Mesonium and antimesonium. *Zhur. Eksptl. i Teoret. Fiz.*, 1957.

[22] Z. Maki, M. Nakagawa, and S. Sakata. Remarks on the unified model of elementary particles. *Prog. Theor. Phys.*, 28:870, 1962.

[23] R. Davis, D. Harmer, and K. Hoffman. Search for neutrinos from the sun. *Phys. Rev. Lett.*, 20:1205, 1968.

[24] John N. Bahcall. Solar neutrino cross sections and nuclear beta decay. *Phys. Rev. B*, 135:137, 1964.

[25] Y. Suzuki. Kamiokande and Super-Kamiokande. *Progress in Particle and Nuclear Physics*, 40(0):427, 1998.

[26] A. B. McDonald et. al. (SNO Collaboration). First neutrino observations from the sudbury neutrino observatory. *Nuclear Physics B - Proceedings Supplements*, 91(13):21, 2001.

[27] G. Drexlin, V. Hannen, S. Mertens, and C. Weinheimer. Current Direct Neutrino Mass Experiments. *Adv. High Energy Phys.*, 2013:293986, 2013, 1307.0101.

[28] Brian Fields and Subir Sarkar. Big-Bang Nucleosynthesis (2006 Particle Data Group mini-review). 2006, astro-ph/0601514.

[29] P. Adamson et al. The NuMI Neutrino Beam. *Nucl. Instrum. Meth.*, A806:279–306, 2016, 1507.06690.

[30] A. Fasso, A. Ferrari, J. Ranft, and P. R. Sala. FLUKA: Present status and future developments. *Conf. Proc.*, C9309194:493–502, 1993.

[31] S. Agostinelli et al. GEANT4: A Simulation toolkit. *Nucl. Instrum. Meth.*, A506:250–303, 2003.

[32] C. Andreopoulos et al. The GENIE Neutrino Monte Carlo Generator. *Nucl. Instrum. Meth.*, A614:87–104, 2010, 0905.2517.

[33] A Aurisano, C Backhouse, R Hatcher, N Mayer, J Musser, R Patterson, R Schroeter, and A Sousa. The nova simulation chain. *Journal of Physics: Conference Series*, 664(7):072002, 2015.

[34] C. H. Llewellyn Smith. Neutrino Reactions at Accelerator Energies. *Phys. Rept.*, 3:261–379, 1972.

[35] Dieter Rein and Lalit M. Sehgal. Neutrino Excitation of Baryon Resonances and Single Pion Production. *Annals Phys.*, 133:79–153, 1981.

[36] R. P. Feynman, M. Kislinger, and F. Ravndal. Current matrix elements from a relativistic quark model. *Phys. Rev.*, D3:2706–2732, 1971.

[37] T. Katori. Meson exchange current (mec) models in neutrino interaction generators. *AIP Conf. Proc.*, 1663:030001, 2015.

[38] J B Birks. Scintillations from organic crystals: Specific fluorescence and relative response to different radiations. *Proceedings of the Physical Society. Section A*, 64(10):874, 1951.

[39] P. A. Cherenkov. Visible emmision of clean liquids by action of γ radiation. *Doklady Akademii Nauk SSSR (in Russian)*, 14, 1934.

[40] Martin Ester, Hans-Peter Kriegel, Jörg Sander, and Xiaowei Xu. A density-based algorithm for discovering clusters a density-based algorithm for discovering clusters in large spatial databases with noise. In *Proceedings of the Second International Conference on Knowledge Discovery and Data Mining*, KDD'96, pages 226–231. AAAI Press, 1996.

[41] Rudolf Kalman. A new approach to linear filtering and prediction problems. 82:35–45, 01 1960.

[42] Nichloas Raddatz. *Muon Neutrino Disappearance in NOvA*. PhD thesis, University of Minnesota, 2016.

[43] C Backhouse, A Radovic, P Singh, and M Campbell. The attenuation and treshold calibration of the nova detectors. Nova collaboration internal document 13579-v35, 2017.

[44] A. Aurisano, A. Radovic, D. Rocco, A. Himmel, M. D. Messier, E. Niner, G. Pawloski, F. Psihas, A. Sousa, and P. Vahle. A convolutional neural network neutrino event classifier. *JINST*, 11(09):P09001, 2016, 1604.01444.

[45] Nitish Srivastava, Geoffrey Hinton, Alex Krizhevsky, Ilya Sutskever, and Ruslan Salakhutdinov. Dropout: A simple way to prevent neural networks from overfitting. 15:1929–1958, 06 2014.

[46] D Torbunov. Numu energy estimator technote for Prod3 MC. Nova collaboration internal document 23342-v2, 2017.

[47] Kanika Sachdev. *Muon Neutrino to Electron Neutrino Oscillation in NOvA*. PhD thesis, University of Minnesota, 2015.

[48] T Blackburn. FD containment criteria for the ν_μ disappearance analysis. Nova collaboration internal document 23402-v1, 2017.

[49] D Mendez. Event selection for the third ν_μ disappearance analysis. Nova collaboration internal document 23234-v7, 2017.

[50] K Bays. Nova cosmic rejection package and algorithms. Nova collaboration internal document 11205-v5, 2017.

[51] Dominick Rocco. *Muon Neutrino Disappearance in NOvA with a Deep Convolutional Neural Network Classifier*. PhD thesis, University of Minnesota, 2016.

[52] Susan Lein. *Muon Neutrino Contained Disappearance in NOvA*. PhD thesis, University of Minnesota, 2015.

[53] Luke Vinton. *Measurement of Muon Neutrino Disappearance with the NOvA Experiment*. PhD thesis, University of Sussex, 2018.

[54] J Lozier. Modularextrap technical note. Nova collaboration internal document 12563-v1, 2014.

[55] C Backhouse. The CAFAna framework - technote. Nova collaboration internal document 9222-v4, 2013.

[56] P. A. Rodrigues et al. Identification of Nuclear Effects in Neutrino-Carbon Interactions at Low Three-Momentum Transfer. *Phys. Rev. Lett.*, 116:071802, 2016.

[57] J. Wolcott and K. Bays. Cross section central value tune and uncertainties for the 2017 analysis. Nova collaboration internal document 23264-v1, 2017.

[58] K. Bays, G. Pawloski, A. Mislivec, and J. Wolcott. NOvA 2018 cross-section tune tech-note. Nova collaboration internal document 23264-v1, 2017.

[59] N Nayak. Flux Systematics for the 2018 NOvA Oscillation Analysis. Nova collaboration internal document 27884-v4, 2018.

[60] M Strait. Muon Energy Scale Systematic. Nova collaboration internal document 20816-v9, 2017.

[61] S Germani. Recap and Update on $\frac{dE}{dx}$ along Tracks. Nova collaboration internal document 20399-v2, 2017.

[62] T Alion. Absolute Calibration and Shape Systematic. Nova collaboration internal document 20318-v1, 2017.

[63] S Germani. Recap and Update on $\frac{dE}{dx}$ along Tracks. Nova collaboration internal document 20399-v2, 2017.

[64] K. Warburton, F. Psihas, and E. Catano-Mur. Numu Systematics 2017. Nova collaboration internal document 27827-v3, 2018.

Appendix A

Glossary and Acronyms

Care has been taken in this thesis to minimize the use of jargon and acronyms, but this cannot always be achieved. This appendix defines jargon terms in a glossary, and contains a table of acronyms and their meaning.

A.1 Glossary

- **Cosmic-Ray Muon** (**CR** μ) – A muon coming from the abundant energetic particles originating outside of the Earth's atmosphere.

A.2 Acronyms

Table A.1: Acronyms

Acronym	Meaning
CRμ	Cosmic-Ray Muon